6-19-2014

Imaging Fourier Transform Spectroscopy of the Boundary Layer Plume from Laser Irradiated Polymers and Carbon Materials

Roberto I. Acosta

IMAGING FOURIER TRANSFORM SPECTROSCOPY OF THE BOUNDARY LAYER PLUME FROM LASER IRRADIATED POLYMERS AND CARBON MATERIALS

DISSERTATION

Roberto I. Acosta, Captain, USAF

AFIT-ENP-DS-14-J-8

DEPARTMENT OF THE AIR FORCE
AIR UNIVERSITY

AIR FORCE INSTITUTE OF TECHNOLOGY

Wright-Patterson Air Force Base, Ohio

AFIT-ENP-DS-14-J-8

IMAGING FOURIER TRANSFORM SPECTROSCOPY OF THE BOUNDARY LAYER PLUME FROM LASER IRRADIATED POLYMERS AND CARBON MATERIALS

DISSERTATION

Presented to the Faculty

Department of Engineering Physics

Graduate School of Engineering and Management

Air Force Institute of Technology

Air University

Air Education and Training Command

In Partial Fulfillment of the Requirements for the

Degree of Doctor of Philosophy

Roberto I. Acosta, BS, MS

Captain, USAF

June 2014

DISTRIBUTION STATEMENT A.
APPROVED FOR PUBLIC RELEASE; DISTRIBUTION UNLIMITED.

AFIT-ENP-DS-14-J-8

IMAGING FOURIER TRANSFORM SPECTROSCOPY OF THE BOUNDARY LAYER PLUME FROM LASER IRRADIATED POLYMERS AND CARBON MATERIALS

Roberto I. Acosta, BS, MS

Captain, USAF

Approved:

_____//signed//_____	28 May 14
Glen P. Perram, PhD (Chairman)	Date
_____//signed//_____	28 May 14
Kevin C. Gross, PhD (Member)	Date
_____//signed//_____	29 May 14
Paul T. Murray, PhD (Member)	Date

Accepted:

_____//signed//_____	3 Jun 14
Adedeji B. Badiru, PhD Dean, Graduate School of Engineering and Management	Date

Abstract

Emissive plumes from laser irradiated fiberglass reinforced polymers (FRP), poly(methyl methacrylate) (PMMA), and porous graphite targets were investigated primarily using a mid wave infrared (MWIR) imaging Fourier transform infrared (FTIR) spectrometer. Polymer and graphite targets were irradiated with a 1.064 μm Nd:YAG and a 1.07 μm ytterbium continuous wave (CW) fiber laser, respectively. Both low speed, buoyant flow atmospheric pressure and shear flow at Mach 0.1 - 0.9 were studied experimentally. Data was acquired with a spectral resolution of 2 cm^{-1} and spatial resolution as high as 0.52 mm^2 per pixel with framing rates up to 2.5 Hz. Strong emissions from H_2O, CO, CO_2 and hydrocarbons were observed in the MWIR between 1900 cm^{-1} and 4000 cm^{-1}. A single-layer radiative transfer model was developed to estimate spatial maps of temperature and column densities of CO and CO_2 from the hyperspectral imagery. Gas plume temperatures were observed as high as 2999 K with statistical errors of ± 395 K and systematic errors of less than 100 K, associated from the different radiative transfer models. Column densities were observed with statistical errors of ~ 5 % and systematic errors of less than ~ 18 %. Also, surface temperatures from optical pyrometry measurements were observed as high as 2500 K with systematic errors of ± 200 K. The imaging Fourier transform spectroscopy (IFTS) observations were complemented with high speed three-color visible imagery and higher spectral resolution, non-imaging Fourier transform spectroscopy (FTS) observations.

Emissive plumes from laser irradiated fiberglass reinforced polymers (FRP) were investigated from hyperspectral IFTS observations. The analysis of pre-combustion spectra yields effective temperatures rising from ambient to 1200 K and suddenly increasing to 1515 K upon combustion. The spectral analysis for a single pixel within a single frame yields an effective temperature of 1019 ± 6 K, and CO and CO_2 column densities of 1.14 ± 0.05 and 1.11 ± 0.03 x 10^{18} molec/cm^2, respectively. Systematic errors associated with the radiative transfer model dominate, yielding effective temperatures with uncertainties of > 100 K and column densities to within a factor of 2-3. Hydrocarbon emission at 2800 to 3200 cm^{-1} was well correlated with CO column density.

Desorption kinetics at the boundary layer was investigated for laser irradiated PMMA. Spatial maps of plume temperature and MMA concentration were developed for surfaces irradiated with laser radiative fluxes between 4 - 22 W/cm^2. The surface temperatures evolved with an initial rise of about 20 K/s, and approach a steady state at about 600 K after 10 s, when irradiated at 22 W/cm^2. When heating the surface with a 10.6 μm CO_2 laser, the rate of temperature rise is about three times greater despite a lower irradiance. For laser irradiated PMMA at 22 W/cm^2, an effective activation energy for MMA formation at the surface of 30.83 ± 8.29 kJ/mol was obtained. This effective activation energy is consistent with surface desorption of the monomer.

For laser-irradiated porous graphite targets, experimental results indicated a dominant CO_2 production at the surface-boundary layer at surface temperatures between 2157 - 2530 K. This indicates production of CO and CO_2 at the surface from heterogeneous reaction. On the basis of CO/CO_2 primary product ratio, we obtained

effective activation energies of 149 to 111 kJ/mol at distances between 0.72 mm to 3 mm in the boundary layer, respectively. The effective activation energies were comparable near the surface (0.72 mm) with the global heterogeneous reaction for production of CO and CO_2 at the surface, whereas in the boundary layer (2.16 mm) with the global homogeneous reaction of CO oxidation to CO_2. Kinetics interplay between heterogeneous and homogeneous combustion are shown from experimental observations at high spatial resolutions. Overall the boundary layer profile at steady-state is consistent with CO being mainly produced at the surface-boundary layer by heterogeneous reactions followed by a rapid homogeneous combustion in the boundary layer towards buoyancy.

To my grandparents, wife and daughter

Acknowledgments

My sincere appreciation to my wife and daughter for their support, understanding and patience, which gave me the strength to finish the academic program. To my grandparents, who I am very grateful for raising me as their son and giving me all their love, which led me to where, I am today. I want to express my deep gratitude to my advisor, Prof. Glen Perram, for the opportunity to work in a fun and fulfilling research field. Thanks for all the technical, personal and scientific guidance to ensure the ultimate success of the research.

Likewise I want to thank the committee members, Dr. Kevin Gross and Prof. Terry Murray. For all the support in this research as well their technical expertise and advices. Thanks to Dr. Gross for ensuring I became successful with MATLAB to process the tremendous amount of data acquired in this research. Also, the Air Force Research Laboratory, Laser Effects Branch (AFRL/RDLE) for their support and providing the facilities to do this research.

I would like to also acknowledge Prof. Greg Jackson from the University of Maryland for providing the spectral database to analyze PMMA. Finally, thanks to the High Energy Laser Joint Technology Office (HEL-JTO) for funding this research.

Roberto I. Acosta

Table of Contents

Page

Abstract iv

Acknowledgements viii

Table of Contents ix

List of Figures xii

List of Tables xx

I. Introduction 1

Document Overview 5

II. Background 9

Fourier Transform Infrared Spectroscopy 9
Laser Materials Interaction 13
Fiberglass 16
Poly(methyl methacrylate) 18
Graphite 20

III. Gas Phase Plume From Laser Irradiated Fiberglass Reinforced Polymers via Imaging Fourier-Transform Spectroscopy 25

Preface 25
Introduction 26
Experimental 29
Results and Discussions 32
Spectral Assignments 32
Spectral Fitting 35
Spatial Maps of Temperature and Concentrations 42
Conclusions 50

IV. Thermal Degradation of Poly(methyl methacrylate) with a 1.06 μm Nd:YAG Laser in a Buoyant Flow 51
Preface 51
Introduction 52
Experimental Methods 56

Page

Results and Discussion 59
Imagery 59
Spectral Features 63
Surface Temperature 72
Plume Dynamics 77
Kinetics 81
Conclusions 87

V. Boundary Layer Combustion Kinetics of Laser Irradiated Porous Graphite from Imaging Fourier Transform Spectroscopy 90

Preface 90
Introduction 91
Experimental Methods 95
Results 97
Plume Dynamics 97
Spectral Analysis 104
Profiles of Temperature and Column Densities 116
Discussion 122
Heterogeneous and Homogeneous Kinetics 122
Conclusions 132

VI. Conclusions 135
Key Results 138
Fiberglass Reinforced Polymers 139
Poly(Methyl Methacrylate) 139
Graphite 141
Summary 142
Recommendations for Future Work 146

Appendix A. Mid Infrared Imaging Fourier Transform Spectromtery for High Power Fiber Laser Irradiated Fiberglass Composites (Invited Paper) 149
Preface 149
Introduction 150
Experimental 153
Instrument Description 153
Experimental Set-Up 154
Results and Discussion 156
Conclusions 165

Page

Appendix B. Preliminary Experiments of Laser Irradiated Graphite in an Oxidizer Flow of M = 0.2 166
Introduction 166
Preliminary Results 166
Spectral Signal 172
Conclusions 176
Recommendations for Future Work 176
Bibliography 178
Vita 193

List of Figures

Figure Page

1. Schematic of Michelson interferometer 10

2. Interferogram as a function of number of OPD 11

3. FTIR spectra of a combustion plume 12

4. Schematic diagram of the experimental apparatus. The imaging Fourier transform spectrometer is positioned to observe the surface-gas boundary layer, with a spatial resolution of 0.9 mm per pixel. The fiberglass surface is normal to the laser beam, with an irradiance of 45 W/cm^2. A cold graphite plate is positioned within the instrument FOV 30

5. Visible images of: (a) the laser irradiated fiberglass sample, (b) the optically thin, smoky plume before combustion, and (c) the optically thick plume after ignition 31

6. Single broadband image of an interferogram in the far DC wing for laser irradiated fiberglass reinforced polymer at 24 s. The plume extends above the surface 10 mm in the x-direction and above 25 mm in the y-direction 33

7. Normalized FTIR spectra for (x,y) = (1.8 mm, 12.6 mm) at 24 s 34

8. (a) Data, model, fit residual, and imaginary component of the spectrum at t = 24 s for (x,y) = (1.8 mm, 12.6 mm) in the spectral region between 2000 - 2400 cm^{-1}. Fit results were T =1019 ± 7 K, q_{CO} = 1.14 ± 0.05 x 10^{18} CO molec/cm^2 and q_{CO2} = 1.11 ± 0.03 x 10^{18} CO_2 molec/cm^2. (b) Atmospheric transmittance profile for 3.12 m path between the plume and the instrument with atmospheric CO_2 concentration of 369 ppm. (c) Empirical emissivity to possibly account for -C ≡ C- stretch 37

Figure Page

9. (a) Comparison of (o) –C≡C- spectra from 1-octyne at room temperature [105] with (---) empirical emissivity of equation (3) for the pixel (x,y) = (1.88 mm, 12.6 mm) at 24 s, with temperature T= 898 K, and (b) peak amplitude of empirical emissivity, $A(\nu=c_2)$, as effective plume temperature increases 40

10. Spatial maps of the: (a) Fit plume temperature, *T* obtained from the LBLRTM calculation at t = 24 s, (b) Brightness temperature that correspond to a hot CO_2 peak at 2295 cm^{-1} 43

11. (a) Spatial maps of column density of CO, and (b) CO_2 (middle panel) in units of (10^{18} molec/cm^2). (c) Corresponding map of the [CO]/[CO_2] column density ratio 44

12. (a) Temporal evolution of plume and surface temperature and (b) temporal CO, CO_2 column densities for t ≥ 15 s. The pre-combustion data is for (x,y) = (1.8 mm, 12.6 mm) and the combustion data is reported for (x,y) = (6.3 mm, 12.6 mm) 46

13. Temporal correlation between the pre-combustion concentrations for: (□) CO, (O) HC, and (◇) –C≡C- at (x,y) = (1.8 mm, 12.6 mm) 48

14. Schematic diagram of the experimental set-up for the (a) side-view experiments (b) sample rotated at 30° to investigate the surface at 21.7 W/cm^2 57

15. Picture of post-irradiated PMMA (a) original and (b) with contrast filter 60

16. Infrared plume imagery of irradiated PMMA at 21.7 W/cm^2 at time intervals of (a) 9 s (b) 18 s (c) 37 s and (d) 57 s 61

Figure Page

17. Difference between two frames (Δt = 0.005 s) at t = 9 s for 21.7 W/cm^2 reveal the turbulent eddies and their effect on the DC component of the interferogram 62

18. Infrared plume imagery of surface irradiated PMMA at t = 24 s for (a) 17.4 W/cm^2 (b) 13.0 W/cm^2 (c) 8.7 W/cm^2 and (d) 4.3 W/cm^2. Plume imagery at different time intervals of (e) 24 s (17.4 W/cm^2), (f) 32 s (13.0 W/cm^2), (g) 131 s (8.7 W/cm^2) and (h) 214 s (4.3 W/cm^2).....63

19. Non-imaging FTIR time averaged spectra for laser irradiated PMMA at 21.7 W/cm^2 showing the spectral radiance (L_ν) of MMA in the (a) LWIR and (b) MWIR 65

20. (a) Molecular structure of PMMA. (b) Structure of the $COOCH_3$ moiety 65

21. (a) Temporal variations of the band integrated radiance, L of selected infrared bands in the LWIR. (b) Band integrated radiance, L of =CH and C-O bands plotted as a function of the irradiance for the 811 cm^{-1} band.....68

22. Temperature dependent absorption coefficient of MMA, κ at 300 (–), 500 (--), 700 (·–) and 1000 (··) K for the CH_3- and $=CH_2$ stretching band in the MWIR 70

23. IFTS observed spectral radiance (--), fit (-) and residual (··) of the MMA 3.4 μm band at (x,y) = (0 mm, 11.7 mm).....71

24. Non-imaged FTIR surface and plume spectral radiance at t = 51 s for the rotated 30° PMMA sample with Planckian at 440 K. The atmospheric CO_2 absorption feature appears near 2400 cm^{-1} 73

Figure Page

25. (a) Time averaged (t > 12 s) observed spectral radiance (O) from center pixel and spectral model (-), yielding an effective surface temperature of 613.9 ± 0.8 K. (b) Timed averaged spatial surface temperature distribution of irradiated PMMA at 21.7 W/cm^2. (c) Laser beam profile at y = 10 mm 74

26. Temporal evolution of surface temperature irradiated with a 1.06 μm Nd:YAG laser at 21.7 W/cm^2 (□), compared against irradiated PMMA surfaces with a 10.6 μm CO_2 laser at 13.7 W/cm^2 (·-) from [52] and electrically heated at 4 W/cm^2(--) and 1.7 W/cm^2 (··) from [125] 76

27. Time averaged spatial maps of gas-phase plume temperature for laser radiative fluxes of (a) 21.7 W/cm^2, (b) 17.4 W/cm^2, (c) 13.0 W/cm^2, (d) 8.7 W/cm^2 and (e) 4.3 W/cm^2 78

28. Time averaged spatial maps of MMA concentrations from the evolve boundary-layer plume for laser irradiated PMMA at (a) 21.7 W/cm^2, (b) 17.4 W/cm^2, (c) 13.0 W/cm^2, (d) 8.7 W/cm^2 and (e) 4.3 W/cm^2 79

29. Temporal evolution of plume temperature at (x,y) = (0.9mm, 12.6 mm) and surface temperature at 21.7 W/cm^2 81

30. Spatially averaged MMA column density (O) and MMA vapor pressure (□) along the surface-boundary layer in the vertical direction (9 mm ≤ y ≤ 16.2 mm) for irradiances between 4.3 to 21.7 W/cm^2. Time, *t*, is defined as the linear pixel dimension (distance) per the buoyant gas velocity of Equation (27).....82

Figure Page

31. Spatially averaged MMA surface column density (O) and MMA vapor pressure (□) along the surface-boundary layer in the vertical direction (9 mm ≤ y ≤ 16.2 mm) for irradiances between 4.3 to 21.7 W/cm^2 83

32. Arrhenius type plot of MMA formation at (x,y) = (0 mm, 12.6 mm) for irradiated PMMA surface at 21.7 W/cm^2 86

33. Schematic experimental set-up 97

34. Time averaged infrared combustion plume imagery of laser irradiated porous graphite (0.6 cm particle size) at (a) 251 W/cm^2, (b) 485 W/cm^2, (c) 777 W/cm^2, (d) 1 kW/cm^2 and (e) 4 kW/cm^2 99

35. Post-irradiated porous graphite target at 4 kW/cm^2 showing structural changes with formation of deposited carbon 100

36. Time averaged infrared combustion plume imagery of laser irradiated porous graphite at 485 W/cm^2 with particle size of (a) 0.6 cm and (b) 0.4 cm. (c) Pyrolitic graphite.....102

37. High-speed visible imagery for irradiated graphite at 777 W/cm^2 at times intervals of (a) 16.28 s, (b) 16.29 s, (c) 16.31 s and (d) 16.32 s. Spatial resolution is 0.14 mm/pixel 103

38. High-speed visible imagery of steady-state diffuse plume and secondary plume of laser irradiated graphite at 777 W/cm^2 at (a) 54.48 s, (b) 54.53 s, (c) 54.58 s and (d) 55.60 s with a 0.14 mm/pixel spatial resolution. The ghost image is due to an out-of-focus image of a bright source in the field-of-view of the camera 104

Figure Page

39. (a) Time averaged (41 s ≤ t ≤ 120 s) spectral radiance for (x,y) = (1.4 mm, 35.3 mm). (b) Basis functions from LBLRTM and optional empirical emissivity, without atmospheric attenuation 105

40. Experimental [143] and simulated emissivity of CO_2, H_2O and CO at 2850 K in the 4.3 μm region 110

41. (a) Un-processed broadband image at 9.2 s with rectangular box indicating spatial averaging (9.36 mm ≤ y ≤ 54.0 mm) for observed data at x = 0.72 mm and modeled by (b) LBLRTM, (c) RADCAL and (d) EM2C 113

42. Comparison of radiative transfer models with observed spectral radiance at x = 0.72 mm for (a)-(c) t = 23 s and (d)-(f) t= 100 s 115

43. Surface and plume temperature at 0.72 – 2.88 mm 118

44. Temporal evolution of CO and CO_2 column densities at (a) 0.72 mm, (b) 1.44 mm, (c) 2.16 mm, and (d) 2.88 mm away from the surface in the boundary layer 119

45. Spatial maps at steady state (41 s ≤ t ≤ 120 s) of (a) CO, (b) CO_2 and (c) plume temperature 121

46. CO/CO_2 ratio as a function of inverse surface temperature at the surface-boundary layer (0.72 mm), with $\alpha/\beta = 4910 \exp(-17{,}970/T)$ 124

47. Effective activation energies as a function of distance from the surface towards the boundary layer.....126

Figure Page

48. Comparison between the CO/CO_2 product ratio predicted by Equation (39) with experimental data (1.2 % relative humidity) at x = 0.72 mm and Tognotti et al. [149] data with 20 % oxygen in dry gas and 3.5 % relative humidity.....128

49. Profiles of gas-phase species and plume temperature along the boundary layer, with surface temperature at ~ 2500 K as a function of t = d/v. *Inset:* spatial plume temperature map with vector showing the path along the boundary layer towards the buoyant flow of the shown profiles.....132

50. (a) Top view for schematic diagram of the experiment set-up with the IFTS perpendicular to the combustion plume for the laser irradiation event. (b) Photo of the actual testing set-up with the sample normal to the laser energy and a cold blackbody plate positioned at the instrument FOV perpendicular to the combustion plume.....155

51. (a) Painted and (b) unpainted fiberglass composite samples before and after 60 s laser radiation. (c) From left to right, still photos of distinctive material response to the laser radiation throughout different time intervals during experimentation ..1

52. Top panel: Unpainted fiberglass composite raw hyperspectral image (32 x 32 pixels) of a single frame (left). (Right) Corresponding raw FTIR spectrum of pixel (15,26) from the top left image. Bottom Panel: Painted fiberglass composite raw hyperspectral (32 x 32 pixels) image of a single frame (left). (Right) Corresponding raw FTIR spectrum of pixel (15,26) from the bottom left

image. The raw FTIR spectrum is for a single pixel (row, column) of a hyperspectral data cube. The brightest pixels are saturated in this image 159

53. Average calibrated FTIR CO and CO_2 spectra of unpainted (top left panel) and painted fiberglass (bottom left panel) for a choice of pixels. Time average brightness temperatures maps of CO at 2065 cm^{-1} and CO_2 at 2288 cm^{-1} for unpainted (top right panel) and painted (bottom right panel) fiberglass 162

54. Ratio of CO_2/CO spatial brightness temperature maps for unpainted (top left panel) and painted (bottom left panel) fiberglass composite. Plot of the CO_2/CO ratio along all columns of row 15 for unpainted (top right panel) and painted (bottom right panel) fiberglass.....164

55. Experimental set-up schematic diagram 168

56. Broadband imagery with hot blackbody 169

57. Intensity variation of an un-processed hyperspectral image at a frame for three different columns (C).....170

58. Intensity variation by shifting columns 105 and 146 by 2 and 1 rows respectively 171

59. Intensity variation for broadband imagery as a function of columns for rows 29, 34 and 39.....172

60. Time averaged broadband image and spectral signature for rows along columns 105, 146 and 188 for laser irradiated graphite (0.12 cm particle size) at 0.8 kW/cm^2 173

Figure Page

58. Time and spatially averaged spectra at the edge of the sample towards the oxidizer stream flow 174

59. Un-calibrated spectra at t = 39 s for rows (8 – 12) along column 106 174

60. Peak CO_2 intensity at 2195 cm^{-1} for rows (11- 16) along columns 105, 146 and 188.....175

List of Tables

Table Page

1. Typical fiberglass composition in percent by weight [41].....17

2. Elemental analysis of black PMMA [60].....19

3. Global heterogeneous and homogeneous reactions for the oxidation of carbon, where $k_j = k_{0,j} \exp(-E_j/R)$ 24

4. Principal infrared bands of MMA [113] 53

5. Thermo-physical properties of black PMMA 57

6. Summary of statistical results obtained from LBLRTM, RADCAL and EM2C at 9, 23 and 100 s. [a]Gas temperature, (K). [b]Column density, (10^{17} molec/cm^2). *Denotes undetectable spectral signature 116

7. Comparison of simulation parameters for Equation (39) 130

8. Test matrix for wind tunnel experiments 167

IMAGING FOURIER TRANSFORM SPECTROSCOPY OF THE BOUNDARY LAYER PLUME FROM LASER IRRADIATED POLYMERS AND CARBON MATERIALS

I. Introduction

The high-energy laser (HEL) lethality community requires a better understanding of laser material damage for a wide variety of emerging threats. In order to reduce the dimensionality of laser-materials interactions, it is necessary to develop novel predictive capabilities of these events. Laser ablation of materials in an oxidizing environment and under the influence of air flow is a complex process defined by the interplay of a number of processes, such as oxidation, vaporization, melting, expulsion of molten material, and breakdown/removal of oxide layer [1-3]. There has been relatively limited computational efforts aimed at investigation of the enhancement of material removal by external gas flow, the effect of the oxidation of metal targets on the efficiency of laser cutting, and the characteristics of the material recession under conditions of laser-induced charring of polymer composites and carbon-rich targets. Often the fundamental analyses must be limited to a few key processes and global, predictive modeling is difficult. The objective is to better understand the fundamentals of laser lethality testing by developing empirical models from hyperspectral imagery thus enabling the development of a robust library of experiments for vulnerability assessments.

Imaging Fourier-transform spectrometers (IFTS) has recently been developed with the ability to measure spatial and temporal variations in plume temperature and

molecular species concentrations, with fast framing rates [4-7]. The coupling of the focal plane array (FPA) to a Michelson interferometer enables collection of spectra at all pixels simultaneously, thus providing precise characterization of emissive infrared plumes at high spatial resolutions. Past research efforts have been aimed to monitor spectral variations of emissive plumes from: detonation fireballs [8-10], muzzle flash [11], jet engines [12, 13], chemical plumes [14, 15] and smokestacks [16]. Recently there has been a growing interest in measuring gaseous emission of flares [17] and laminar flames [18] to identify and quantify such emissions. With previous work illustrating some of the capabilities of this instrument, there is significant potential for studying combustion plumes from laser irradiated polymers and carbon based materials. Some of the benefits of hyperspectral imagery for examining combustion events are: (1) turbulence in plume dynamics can be studied from high-speed broadband imagery contained in the interferogram cubes, (2) narrow instantaneous field-of-view (IFOV) simplifying spatial averaging as well the spectral interpretation for large variations in the temperature and density of combustion plumes, and (3) construction of two-dimensional dynamics of the evolve species in the gas phase to predict the chemical kinetics interplay in a dynamic flow revealing plume symmetry [12].

Mid wave IFTS has the ability to measure simultaneous spatial and temporal variations in molecular species concentrations and gas temperature fluctuations in the spectral range of 1800 – 6667 cm^{-1} (1.5–5.5 μm) with adequate spectral (0.25–150 cm^{-1}) and spatial resolutions (≤ 1 mm^2 per pixel). The instrument features a 320 x 256 pixel Stirling-cooled indium antimonide (InSb) focal plane array (FPA) that can be narrowed to

improve the temporal resolution. At a focal distance of 3.12 m, the IFOV yields a spatial resolution of ~ 0.81 mm^2 per pixel. The instrument has been upgraded with a 0.25X telescope that allows for a minimum focal distance of 35 cm, improving spatial resolution up to 0.29 mm^2 per pixel. A series of modulated intensity images corresponding to optical path differences (OPDs) are collected on the FPA, forming an interferogram at each pixel. A hyperspectral data cube is comprised of a stack of 2D images corresponding to different optical path differences. The rate at which a data cube can be acquired is dependent on spectral resolution, FPA integration time, and the number of pixels within the image. On typical instrument framing rate of 50 kHz and ~ 10,000 OPDs yields hyperspectral data cubes at 2.5 Hz, for 2 cm^{-1} and a 32 x 32 pixel field of view. Fast Fourier Transform (FFT) of each pixel's interferogram produces a raw spectrum, which is then calibrated with two internal wide-area black body sources at known temperatures. Using established radiometric calibration procedures the spectrally dependent gain and background for each pixel are determined [19]. The raw spectrum is divided by the gain and subtracted by the offset to convert the spectra into absolute units of spectral radiance ($W/(cm^2\ sr\ cm^{-1})$). Using a 0.3 optical density neutral density (ND) filter the 16-bit FPA saturates with 65,000 counts at 300 $\mu W/(cm^2\ sr\ cm^{-1})$, with a background radiance of 6 $\mu W/(cm^2\ sr\ cm^{-1})$. For gas plume temperatures near 1000 K, the DC component of the interferogram represents 28 % of the dynamic range, with the interferometer producing an 8 % modulation at zero optical path difference (ZPD).

In the current work, we demonstrate the potential of IFTS for monitoring thermal decomposition and combustion in the gas plumes generated by laser irradiation of

polymers and graphite targets. The effectiveness of high energy lasers to render a target nonfunctional depends on propagation of the laser through these evolving gas plumes, heat released in exothermic gas phase reactions, and changes to surface oxidation kinetics [1-3, 14, 20, 21]. Extension of the IFTS instrument to these laser-material interactions requires: (1) application to short focal distances (a few meters rather than the kilometer paths used for smokestack and jet/rocket engine observations) [12, 13, 16], (2) high spatial resolution (~ 1 mm sampling for laser spot sizes of 1-10 cm), (3) handling large changes in source radiance (pre and post combustion) and managing the instrument dynamic range, (4) evaluating high gas temperatures (> 2800 K) and large temporal-spatial variations in column density for various materials including: graphite, carbon composites, painted metals, and polymers films [22-24], and (5) radiative modeling of complex hydrocarbon spectra and kinetics.

To accomplish this work we collaborated with the Air Force Research Laboratory (AFRL), Laser Effects Branch (RDLE) at Kirtland Air Force Base (KAFB), NM. Experiments were carried out at their HEL testing facilities to investigate emissive plumes from laser irradiated targets. By deploying the Air Force Institute of Technology (AFIT) hyperspectral instruments we were able to: (1) conduct experiments with polymer and graphite targets, (2) identify molecular emitters in the gas-phase plume generated from laser lethality experiments, (3) employ radiative transfer models to quantify the plume temperature and effluents concentration along the boundary layer, (4) produce two-dimensional spatial maps of plume temperature and molecular species, (5) demonstrate the feasibility to study the kinetics interplay of pre-combustion and

combustion gases from laser irradiated targets. These combined efforts enable new predictive capabilities for the laser lethality community.

Key contributions to the field are: (1) benchmarking hyperspectral imagery to laser lethality experiments, (2) development of the first two-dimensional spatial maps of temperature and effluents concentrations of the evolve boundary layer plume from laser irradiated targets, (3) kinetics interpretation at high spatial resolutions from experimental observations. This research advances the understanding of the fundamental mechanism of laser irradiated-materials from hyperspectral imaging observations. The current work establishes a robust foundation for future experiments aimed to close the gap between the empirical lethality databases and fundamental modeling with predictive capabilities. As a result, the combustion kinetics in laminar flows can be explored to merge experiments with detail reactive fluid dynamics simulations.

Document Overview

Chapter II provides the background material on imaging Fourier transform infrared spectroscopy (IFTS). Basic review of laser materials interaction, properties of fiberglass, poly(methyl methacrylate) and graphite targets, and a literature survey on the kinetics of oxidation of carbon. A review of AFIT's prior research efforts with the IFTS instrument is also presented.

A separate chapter is devoted to each of the materials studied. The results for FRP, PMMA, and porous graphite are presented in Chapters III, IV and V, respectively. These chapters have been submitted for peer review or are about to be submitted for publication, and therefore include some redundant material provided elsewhere in this

document. The purposes of these chapters are to demonstrate the use of hyperspectral IFTS of laser lethality experiments.

The proof of concept and feasibility of the use of IFTS in laser lethality experiments are discussed in chapter III, which has been accepted for publication [25]. By monitoring the evolved plume of laser irradiated fiberglass composite targets, molecular species in the plume were identified from their spectral signatures in the mid-wave infrared (MWIR). Following identification of the molecular species, a simplified line-by-line radiative transfer model (LBLRTM) [26, 27] was developed to extract profiles of temperature and effluents column densities. For a single data cube, spatial maps of pre-combustion gas temperature and column densities of CO and CO_2, were developed from LBLRTM. To partially illustrate the evolving plume, the temporal dependence of temperature and column densities for a single pixel was explored. Our empirical observations were validated with prior FTIR fiberglass study [24].

Chapter IV discuss the laser radiative oxidative decomposition of poly(methyl methacrylate) (PMMA) and the effects of power density on the evolved plume from IFTS observations [28]. Carbon black pigmented PMMA targets were irradiated with a 1.06 μm fiber laser from 4 to 22 W/cm^2. Strong spectral emission of the monomer methyl methacrylate (MMA) was observed in the infrared. Assuming a homogeneous single layer plume, a simplified radiative transfer model was developed. The spectral model was used to compute the gas emissivity using data from an experimentally measured, interpolated and extrapolated MMA absorption coefficient database. Spatial maps of plume temperature and MMA column densities were developed for laser irradiated

surfaces at 4 - 22 W/cm^2. Also, we demonstrated the use of IFTS to obtain surface temperature of laser irradiated PMMA. By fitting the observed spectra with Planck's distribution, we were able to produce spatial and temporal distributions of surface temperature as well to estimate the beam profile. This work demonstrated the feasibility of investigating the kinetics of MMA formation at discrete pixels in the surface-boundary layer. The obtained effective activation energies were consistent with current established PMMA decomposition kinetics.

Chapter V culminates our work with the combustion mechanism of laser irradiated graphite targets from imaging FTIR observations [29]. We compare our results against well established kinetics mechanism for the oxidation of graphite. Porous graphite targets were irradiated using a 1.07 μm 20-kW ytterbium fiber laser. The combustion plume characteristics of irradiated porous graphite is discussed from high-speed infrared and visible imagery and documented for first time. A homogeneous single-layer plume LBLRTM was developed to estimate spatial maps of temperature and column densities of CO and CO_2 from hyperspectral IFTS. Also, we validated the use of statistical narrow-band models (EM2C and RADCAL) [30, 31] with experimental combustion data at temperatures as high as 2900 K. Systematic errors associated with the spectral models are discussed. Kinetics interplay between heterogeneous and homogeneous combustion kinetics are shown from experimental observations at high spatial resolutions. Overall the boundary layer profile at steady-state is consistent with CO being mainly produced at the surface-boundary layer by heterogeneous reactions followed by a rapid homogeneous combustion in the boundary layer towards buoyancy.

An overall conclusion of the work and summary of the results is presented in chapter VI along with recommendations for future studies in a laminar flow. Following the conclusion are appendices showing earlier proof of concept work that was published as a proceeding article focused on a qualitative analysis of painted and unpainted fiberglass targets [32]. Also, preliminary graphite experiments observations in a tube flow are documented to facilitate the planning of future systematic laminar flow experiments.

II. Background

Fourier Transform Infrared Spectroscopy

Fourier transform infrared spectroscopy (FTIR) measures the vibrational frequencies at which a sample (solid, liquid or gas) absorbs or emits infrared radiation. These vibrational frequencies are useful to identify molecular species composition and concentrations. In principle, FTIR spectrometers are based on a Michelson interferometer [33-35], a schematic diagram is shown in Figure 1. A Michelson interferometer typically consists of a translating mirror, beamsplitter, and a detector. The incident beam of radiation is divided into two paths by the beamsplitter, which travels to the fixed and moving mirror. These two beams are then recombined after an optical path difference (OPD) has been established [36]. The OPD between the two beams is defined as the position of the translating mirror with respect to the beam splitter. It can be expressed as $OPD = d_1 - d_2$, where d_1 and d_2 are the respective distances of the moving and fixed mirror with respect to the beam splitter. By scanning the translating mirror, an interference pattern is produced between the two beams. The variation in intensity of the beam as a function of number of OPDs is recorded by a detector, in which the spectral information is encoded. This is known as an interferogram or an interference pattern.

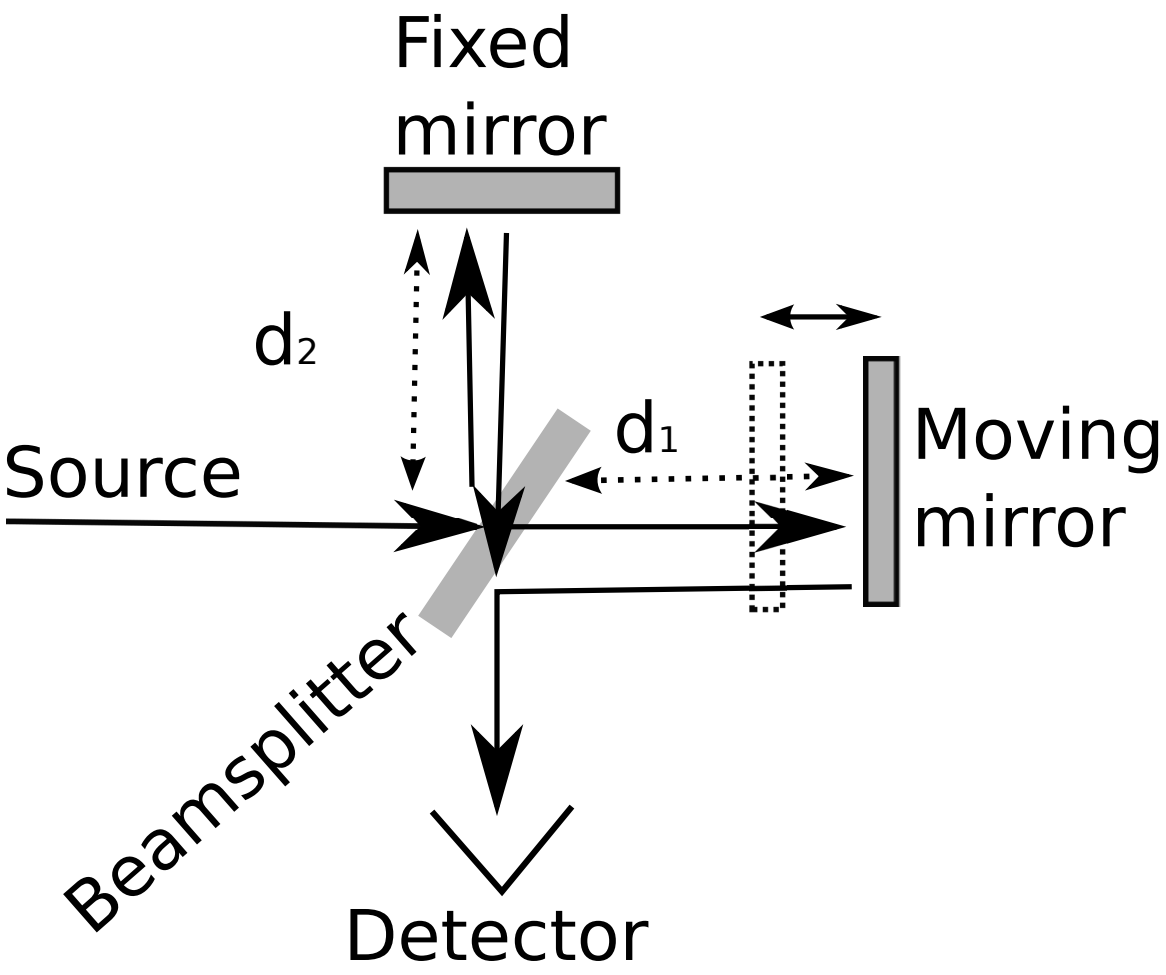

Figure 1. Schematic of Michelson interferometer

To obtain a spectrum, a fast Fourier transform (FFT) is applied to the resulting interferogram. Cooley and Tukey [37] developed an FFT algorithm that is commonly used in FTIR, substantially reducing computation time as opposed to using the classical discrete Fourier transform method. Figure 2 shows the observed signal from the detector as a function of number of OPDs (number of frames). The center burst of the interferogram contains a broadband source where all wavelengths are phase at zero path difference (ZPD). Most of the useful spectral information is contained at the wings of the

interferogram where the amplitude is lower. The FFT to the interferogram results in a spectrum, shown in Figure 3. The corresponding spectral emission of gaseous molecuar species is shown in Figure 3 for CO and CO_2. The spectral emission in Figure 3 corresponds to a combustion flame.

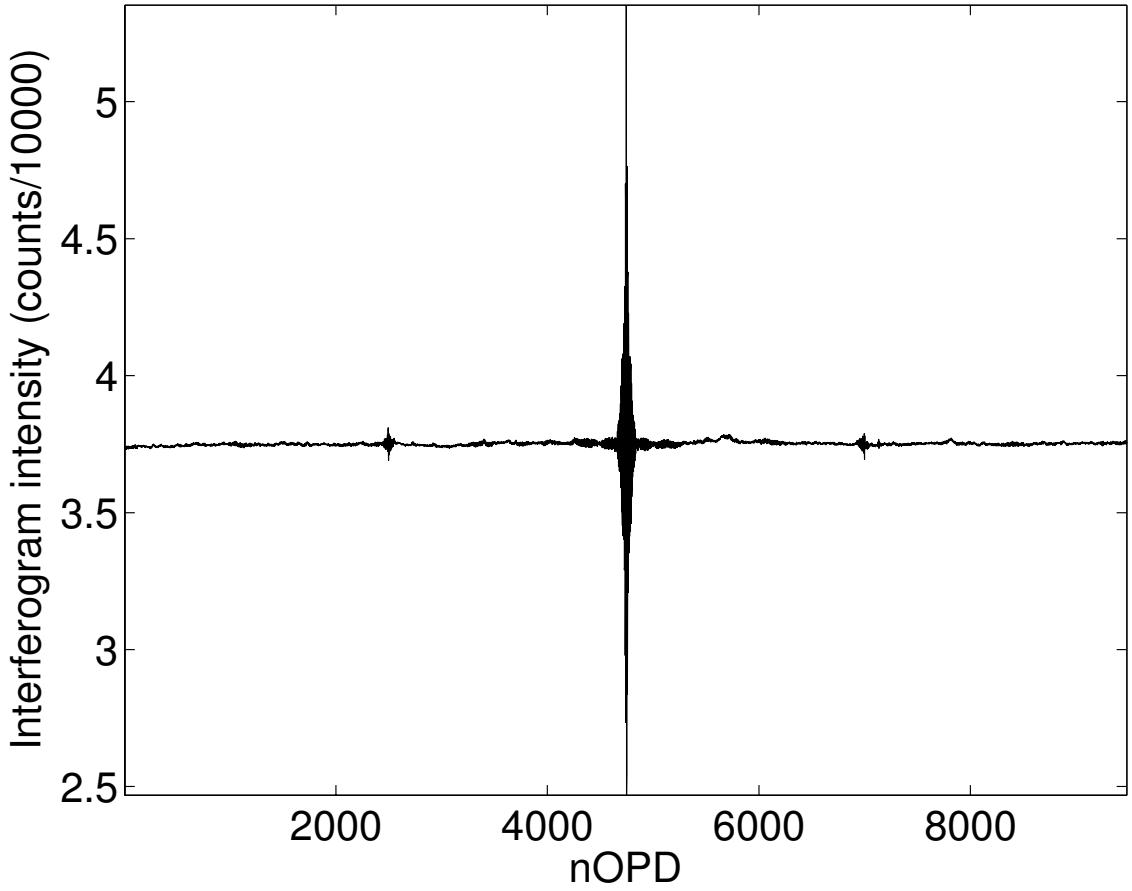

Figure 2 Interferogram as a function of number of OPD

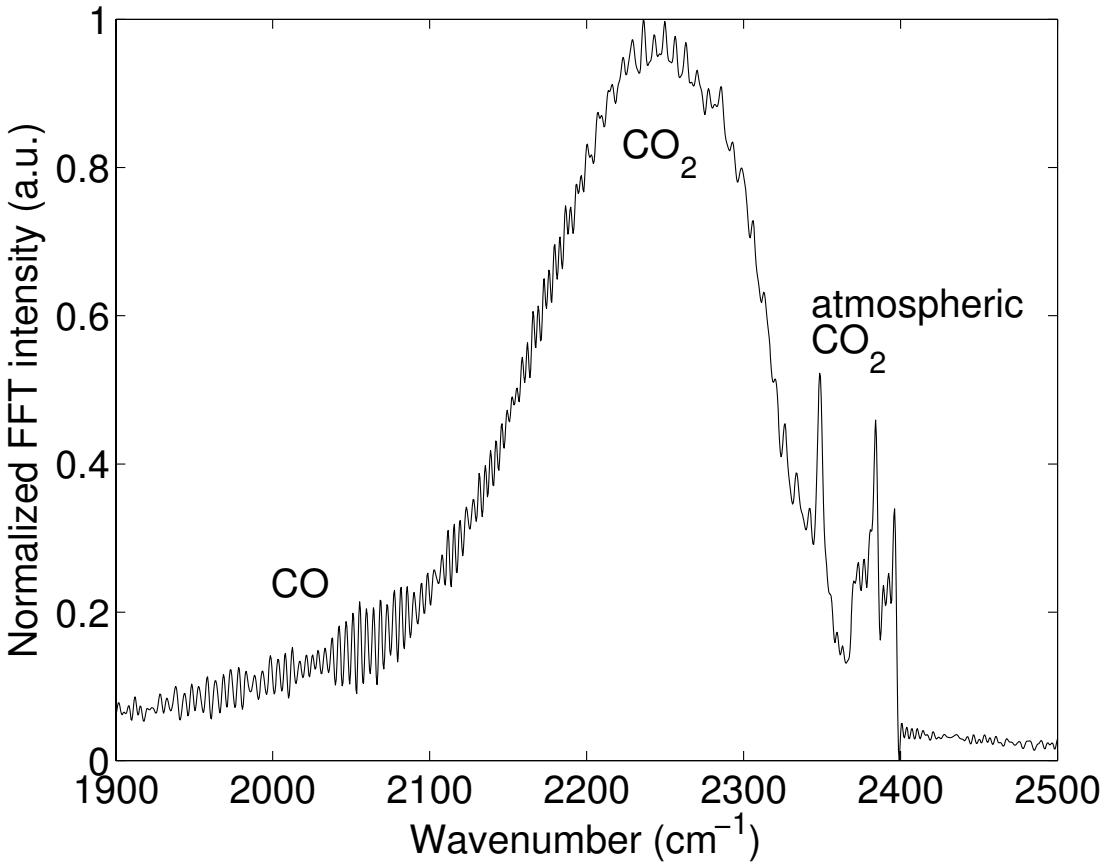

Figure 3 FTIR spectra of a combustion plume

Non-imaged FTIR spectroscopy has been used to investigate the temporal evolution of combustion gases by the Federal Aviation Agency (FAA) for cargo air protection applications [38]. Toxicity evaluation of combustion gases generated from burning materials requires fast framing and high spectral resolutions for early detection and accurate identification of volatile fuels. In combustion gases, emission of H_2O, CO and CO_2 are present, which have been monitored from FTIR measurements. Fourier transform spectroscopy is a well established characterization technique to investigate the rapid changing combustion gases. However non-imaged FTIR acquires data with a

single detector, where the scene is spatially averaged. This becomes a challenge for laser lethality experiments since spatial information from the evolved surface-boundary layer plume is lost. This can be overcome with the recent development of imaging FTIR spectrometers, where a single detector is replaced with a focal plane array (FPA) where each pixel correspond to a single spectral point in space. Another advantage from IFTS is that the high-speed broadband infrared imagery (DC+AC) reveals plume dynamics such as turbulent motion. Laser lethality experiments can benefit from imaging FTIR to investigate the evolved boundary layer plume at high spatial resolutions.

Imaging FTIR has the potential to measure both spatial and temporal variations in temperature, chemical species concentrations, and the ability to spectrally identify molecular species at high resolution and fast framing rates [4, 5]. Some of the benefits of hyperspectral imagery for examining laser lethality combustion events are: (1) turbulence in plume dynamics can be studied from high-speed broadband imagery contained in the interferogram cubes, (2) narrow instantaneous field-of-view (IFOV) simplifying spatial averaging as well the spectral interpretation for large variations in the temperature and density of combustion plumes, and (3) construction of two-dimensional dynamics of the evolved species in the gas phase to predict the chemical kinetics interplay [12].

Laser Materials Interaction

The use of Laser weapons has been attractive for military operations, particularly for engaging close-in maneuvering targets and fast ballistic targets. However, laser lethality require depositing sufficient energy or a dwell time to render a target non-functional [2]. Lasers allow acquiring targets very quickly due to the few moving

mechanical parts in laser weapons systems. Laser weapons systems have a low incremental cost per shot when compared with advanced missile systems [39]. Nonetheless, laser weapons effectiveness can be limited due to: atmospheric attenuation and turbulence, line-of-sight dependence, target suitability, and laser wavelength selection.

Laser lethality can lead to a variety of effects in the ablated material. This includes a number of complex process such as oxidation, vaporization, melting, expulsion of molten material, and breakdown/removal of an oxide layer [1-3]. Laser ablation will lead to the formation of a plume that expands out from the surface. Ejection of surface material is due to the ablation pressure generated by the expansion of the gas at the surface-boundary layer. Therefore it is important to understand the plume characteristics generated from laser ablation above the surface. As the plume evolves from the surface, it absorbs the incident radiation, thus reducing the absorbed energy at the material surface [1].

Chemical lasers have been used in laser weapons systems due to the very high energy derive from the chemical reactions that produce up to megawatts of power [39]. There has been a growing interest in scaling solid state fiber lasers to high power. Moreover, these can be powered from the aircraft electrical power source as opposed to carrying large amounts of payloads needed with chemical lasers. Recent improvements in solid state lasers, promise to provide effective laser weapons in the near-IR since these are light enough to be mounted on smaller air vehicles platforms. Therefore, there is a

growing interest to scale laser lethality experiments in the near-IR wavelength using fiber lasers with advanced materials such as polymers and carbon rich targets.

Experiments aimed to understand the interaction of laser weapons with advanced targets has been made with composite materials. For example, previous experiments with polymer targets have shown an increase in plume temperature above steady surface temperature, likely due to gas phase plume absorption of the incident radiation [25, 28, 40]. Similar results have been observed from the evolved combustion plume of laser irradiated graphite targets [29]. Several experimental techniques has been used to monitor the evolve plume from laser ablation [41-43]. However none of these offer the ability to explore the plume kinetics at high spatial resolutions to validate reactive fluid dynamics models. Moreover, as a consequence of laser ablation, a chemical reaction could occur with its surroundings producing a gas phase combustion plume above the surface. This exothermic reaction emits very strongly in the infrared, thus allowing identification of molecular species associated with combustion, such as CO, CO_2 and H_2O. Imaging FTIR promises to be a novel technique to investigate the evolved plume from laser irradiated materials [25, 28, 29, 32].

In order to validate modeling with empirical databases on laser lethality, it is important to understand the interplay between laser wavelength, type of material, and flow conditions where laser ablation occurs. For that reason, we aim to understand emissive plumes above the surface of laser irradiated polymers and carbon rich targets using novel molecular spectroscopy techniques to validate empirical models with global kinetics in an oxidizing environment.

Plume kinetics fluctuates with the type of target and material properties. Preliminary qualitative results reveal that the addition of paint in fiberglass targets had an effect on the combustion rate during laser heating experiments [32]. Painted fiberglass composite targets self-ignited 4 s earlier than unpainted fiberglass samples. The current work is focused on the plume evolution above the surface from laser irradiated fiberglass, PMMA and graphite targets. These materials are discussed further below.

Fiberglass

Few combustion studies have been made with composite materials, such as fiberglass reinforced polymers (RFP) [24, 40]. Kinsella et al. [24] applied a radiant flux to study the combustion of silicone-, melamine-, and epoxy-fiberglass composites by focusing a 600 W tungsten-halogen lamp over a 25 mm diameter area. These materials are used in the construction of aircrafts, boats, and military vehicles. Some visible physical observation on the surface of these fiberglass composites during irradiation are bubbling, charring, out-gassing, laminate separation, and spontaneous ignition. The combustion of these three fiberglass samples was monitored by non-imaging FTIR. Where the products evolving above the surface in the gas phase were identified from their corresponding spectra.

Fiberglass is primarily composed approximately of 50 % by weight of silica (SiO_2) with other inorganic and trace components as shown from Table 1 [41]. Additionally, fiberglass composite materials may contain sizings, binders, or flame retardants as well organics components [42]. Fiberglass reinforced polymers have a complex chemical structure [24, 43]. Moreover fiberglass is generally composed of

adhesive joints with many components [43] and multiple interfaces, typically epoxy or polyester based [24, 40].

Table 1. Typical fiberglass composition in percent by weight [41]

Inorganic composition	wt %
Silica (SiO_2)	54.0 %
Calcium Oxide (CaO)	20.5 %
Alumina (Al_2O_3)	14.0 %
Boron Oxide (B_2O_3)	8.0 %
Soda (Na_2O)	1.0 %
Calcium Fluoride (CaF_2)	1.0 %
Magnesia (MgO)	0.5 %
Minor oxides (K_2O, SO_3, Fe_2O_3)	1.0 %

The combustion characteristic of polyester-based fiberglass composite materials has been described by *Landrock* [44] as burning with a smoky flame, accompanied by melting, dripping and some char formation. Combustion products of polyester-based materials have been reviewed elsewhere [45-47], containing organic components such as C_6H_6 (benzene), $(C_6H_5)_2$ (biphenyl), $C_6H_5CH_2CH_3$ (ethyl benzene), C_5H_8 (pentadiene), $C_6H_5CH{=}CH_2$ (styrene), and CH_3 (toluene). It has been reported that these composite materials have a flash-ignition temperature of approximately 648 K (375 ^oC) and a self-ignition temperature of approximately 758 K (485 ^oC) [40, 41].

Fourier transform spectroscopy has the ability to distinguish the ro-vibrational bands of diatomic and polyatomic molecules in the infrared spectrum, allowing quantification of the chemical species concentration as function of time [48]. Most of the FRP combustion products are classified as toxic products. Consequently, spectral identification plays an important role for early detection applications [24, 40, 49, 50]. To the author's knowledge, laser induced combustion of fiberglass targets has not been investigated before.

Poly(Methyl Methacrylate)

Laser lethality experiments with PMMA, has been made with continuous wave (CW) CO_2 lasers at the longer wavelength of 10.6 μm [51-56], yet very few studies at the near-infrared wavelength of 1.06 μm [57-59]. This is mainly due to the poor absorption characteristic of organic materials in this region. Because of this, pigments are commonly added to acrylic thermoplastics for absorption in the near-IR. The reported average composition of black PMMA from elemental analysis are shown in Table 2 [60].

When polymers are irradiated, the incident energy is absorbed at the surface, generally to a depth of micrometers. According to Said-Galiev and Nikitin [61], the depth of absorption in the material follows the Beer-Lambert law as defined by Equation (1):

$$I(z) = I_0 \exp(-\alpha \cdot z) \tag{1}$$

where, $I(z)$ is the irradiance (W/cm^2) at depth z (cm), I_0 is the incident irradiance (W/cm^2), and α is the absorptivity (cm^{-1}) of the material. Ablation of polymeric materials with a CO_2 laser are discussed elsewhere [61].

Table 2. Elemental analysis of black PMMA [60]

Elements	Composition (wt %)
Carbon (C)	59.1
Hydrogen (H)	7.9
Oxygen (O)	31.9
Nitrogen (N)	< 0.3
Sulfur (S)	< 0.2
Chlorine (Cl)	0.1
Water (H_2O)	0.6
Total	< 100.1

Typically, polymers have low thermal conductivity, which means that the effects related to ablation are surface effects. Therefore the kinetics and mechanism of laser irradiation vary depending on the chemical structure and thermophysical properties of the material. The absorptivity of clear PMMA varies depending on the type of laser wavelength used, a value of 250 cm^{-1} was obtained with a CO_2 laser (10.6 μm), whereas values of ~ 25 cm^{-1} were assumed for hydrogen fluoride (HF) and deuterium fluoride (DF) chemical lasers at wavelengths of 2.7 μm and 3.8 μm, respectively [62]. When thermoplastic polymers were irradiated with a CO_2 laser, Cozzens and Fox [63] reported that no breakdown happened between 3-7 W/cm^2, but at 5-11 W/cm^2 a softening occurred; at the higher irradiance of ~ 22-25 W/cm^2, the material decomposed and vaporized.

Poly(methyl methacrylate) (PMMA) is an inexpensive thermoplastic that decomposes around 493 K [64]. In the presence of oxygen, the main decomposition product is the monomer methyl methacrylate (MMA) [65]. Molecular oxygen exerts a stabilizing effect on PMMA against depolymerization at low temperatures [66-68], thus increasing the initial decomposition temperature when compared to that for thermal degradation in an inert gas. Methyl methacrylate further decomposes to combustible gaseous hydrocarbon species. These hydrocarbon fuels react with oxygen to create CO, CO_2 and H_2O from combustion. Thermal decomposition kinetics of PMMA has been reviewed in detail elsewhere [69]. In general, PMMA decomposition can be summarized by reaction (2) [70]:

$$PMMA \rightarrow MMA \rightarrow HC \rightarrow CO, CO_2, H_2O \qquad (2)$$

where, PMMA decompose primarily to MMA, then MMA decompose to small combustible HC fuels and an exothermic reaction will lead to the combustion products of CO, CO_2 and H_2O.

Graphite

Combustion from laser-irradiated graphite targets using a 5 kW CO_2 laser (beam area of 11.6 cm^2) were investigated by Caminat et al. [71]. Cylindrical graphite targets of 8 cm diameter x 5 cm height with low porosity and impurities (< 100 ppm) were exposed to a radiant flux. A set of experiments consisted of irradiating the surface from 78 to 418 W/cm^2 for 300 s. In order for a sizeable combustion plume to occur, at least an irradiance of 181 W/cm^2 was required [71]. Several mechanisms have been discussed for

the graphite oxidation kinetics [72]. However, whether or not CO and CO_2 are the primary products from the oxidation of carbon it still a debate in the literature today [73]. It has been accepted as general consensus that for temperatures greater than 1200 K, the CO_2 production is small [74], but at lower temperatures both CO and CO_2 are present [75, 76]. On the other hand, several authors indicate that both CO and CO_2 are primary products of the surface heterogeneous reaction [75-79]. The primary product ratio of CO/CO_2 has been measured experimentally by many investigators and expressed empirically for the relative rates at which CO and CO_2 are produced by the Arrhenius relation of $CO/CO_2 = A \exp(-E_a/RT)$, where A and E_a are the pre-exponential and effective activation energy obtained empirically. According to Arthur [74], the CO/CO_2 ratio increases with temperature and the effective activation energy is, $E_a = E_{CO2}-E_{CO}$, which is estimated from the slope of the Arrhenius relationship by the least square method. The resulting effective activation energy, E_a, is for the production of CO and CO_2 from the heterogeneous reaction at a measured temperature range. For example, the empirical relationship from Arthur [74] is defined as: $[CO]/[CO_2] = 2500 \exp(-6240/T)$, where at T = 800 K, $[CO] = [CO_2]$, and at T = 1700 K CO was found to be 64 times higher than CO_2.

Li et al. [72] discussed the surface oxidation mechanism of graphite from gravimetric and temperature-programmed desorption experiments. The oxidation mechanism is based on the formation and dissociation of oxide complexes from Lear et al. [80]:

$$*C + O_2 \underset{k_{-3}}{\overset{k_3}{\leftrightarrow}} *C(O_2) \qquad (3)$$

$$*C(O_2) \xrightarrow{k_4} *C(O) + CO \quad (4)$$

$$*C(O) \xrightarrow{k_5} CO \quad (5)$$

$$*C(O) \xrightarrow{*C(O_2),k_6} CO_2 \quad (6)$$

$$*C + O_2 \xrightarrow{*C(O),k_7} CO_2 \quad (7)$$

Molecular oxide complexes initially form in reaction (3), but these complexes rearrange to form a stable atomic–oxide complex and evolve CO, in reaction (4). The stable oxide complex may subsequently desorb from the surface by reaction (5) or be involved in the evolution of CO_2 by reaction (7), where *C is a free carbon site, *C(O_2) is a dioxygen surface complex and *C(O) a stable oxide surface species.

Tucker and Mulcahy [81] suggested that oxygen molecules directly react with labile carbon atoms (*C) producing CO and leaving O atoms attached to the carbon surface (*C(O)) by reaction (8) according to

$$2*C + O_2 \leftrightarrow *C(O) + CO \quad (8)$$

Ahmed and Back [82] concluded that molecular oxygen initially adsorbs on the carbon surface (reaction (3)) and then slowly rearranges to a stable complex involving oxygen atoms from reaction (9):

$$*C + *C(O_2) \rightarrow 2*C(O) \quad (9)$$

Eisenhut [83] combined this previous reaction with reaction (3) and proposed the following reaction:

$$2*C + O_2 \leftrightarrow 2*C(O) \tag{10}$$

On the other hand, the mechanism for formation of CO_2 at the surface is poorly understood. For the evolution of CO_2, Vastola et al. [84] proposed:

$$2*C(O) \rightarrow CO_2 + *C \tag{11}$$

Marsh [85] agreed with the previous step and added the following two reactions:

$$*C(O) + CO \rightarrow CO_2 + *C \tag{12}$$

$$2*C(O) + \frac{1}{2}O_2 \rightarrow CO_2 + *C \tag{13}$$

Carbon dioxide (CO_2) formation requires collisions of the stable oxide complex with gas-phase species. Ahmed and Back [82] added another reaction step involving both *C(O) and *C(O_2) complexes and provided the following variation for primary CO_2 formation:

$$*C(O) + *C(O_2) \rightarrow CO_2 + *C(O) \tag{14}$$

$$*C + *C(O) + O_2 \rightarrow CO_2 + *C(O) \tag{15}$$

Lear et al. [80] proposed that a source of CO_2 is produced from direct reaction of *C(O_2) with O_2:

$$*C(O_2) + \frac{1}{2}O_2 \rightarrow CO_2 + *C(O) \tag{16}$$

Du et al. [86] proposed a mechanism involving direct reaction of O_2 with carbon sites:

$$*C + O_2 \rightarrow CO_2 \tag{17}$$

Furthermore, graphite combustion models are typically based on elementary reactions or semi-global models [78, 79, 87-89]. For simplicity, established global kinetics are considered and compare with experimental results obtained from IFTS observations. The simplified global heterogeneous [90-93] and homogeneous [94-96] reactions of carbon oxidation considered in this work are summarized in Table 3.

Table 3. Global heterogeneous and homogeneous reactions for the oxidation of carbon, where $k_j = k_{0,j} \exp(-E_j/R)$

Reaction	$k_{0,j}$	$-E_j/R$ (K)	Reference
$\frac{\alpha+\beta}{\alpha/2+\beta} C_{(s)} + O_2 \rightarrow \frac{\alpha}{\alpha/2+\beta} CO + \frac{\beta}{\alpha/2+\beta} CO_2$	3.01 x 10^5 m/s	17,966	[90-93]
$CO + 1/2\, O_2 \rightarrow CO_2$	1.3 x 10^{11} m^3/(kmol s)	15,098	[96]

III. Gas Phase Plume From Laser Irradiated Fiberglass Reinforced Polymers via Imaging Fourier-Transform Spectroscopy

Preface

A reformatted version of the original published manuscript in Applied Spectroscopy is presented in this chapter [25]. As the lead author my contributions were to collect and post-process the experimental data, hence contributing with the co-authors in the analysis, interpretation and discussion of the results. Emissive plumes from laser irradiated fiberglass reinforced polymers (FRP) were investigated using a mid-infrared imaging Fourier-transform spectrometer, operating at fast framing rates (50 kHz imagery and 2.5 Hz hyperspectral imagery) with adequate spatial (0.81 mm^2 per pixel) and spectral resolution (2 cm^{-1}). Fiberglass reinforced polymer targets were irradiated with a 1064 nm cw Nd:YAG laser for 60 s at 100 W in air. Strong emissions from H_2O, CO, CO_2 and hydrocarbons were observed between 1800 cm^{-1} and 5000 cm^{-1}. A single-layer radiative transfer model was developed for the spectral region from 2000 to 2400 cm^{-1} to estimate spatial maps of temperature and column densities of CO and CO_2 from the hyperspectral imagery. The spectral model was used to compute the absorption cross sections of CO and CO_2 using spectral line parameters from the high temperature extension of the HITRAN database. The analysis of pre-combustion spectra yields effective temperatures rising from ambient to 1200 K and suddenly increasing to 1515 K upon combustion. The peak signal-to-noise ratio for a single spectrum exceeds 60:1, enabling temperature and column density determinations with low statistical error. For example, the spectral analysis for a single pixel within a single frame yields an effective

temperature of 1019 ± 6 K, and CO and CO_2 column densities of 1.14 ± 0.05 and 1.11 ± 0.03 x 10^{18} molec/cm^2, respectively. Systematic errors associated with the radiative transfer model dominate, yielding effective temperatures with uncertainties of > 100 K and column densities to within a factor of 2-3. Hydrocarbon emission at 2800 to 3200 cm^{-1} is well correlated with CO column density.

Introduction

Imaging Fourier-transform spectrometers (IFTS) have recently been developed with the ability to measure spatial and temporal variations in plume temperature and molecular species concentrations, with fast framing rates [4-7]. The coupling of the focal plane array (FPA) to a Michelson interferometer enables collection of spectra at all pixels simultaneously, thus providing precise characterization of emissive infrared plumes. Hyperspectral IFTS imagery in the mid-infrared from an industrial smokestack has been analyzed to extract temperatures to within a few degrees and concentrations of strong emitters with statistical uncertainties of 1 - 6 % [16]. Jet engine exhaust has also been analyzed with similar uncertainty despite the presence of significant turbulence [12-15]. For cases where scene fluctuations are driven by a random global parameter, such as temperature, one can take advantage of the DC-coupled interferograms (modulated image) to extract turbulence information [12]. Recently there has been a growing interest in measuring gaseous emission of flares [17] and laminar flames [18] to identify and quantify such emissions. Mass flow rates from gaseous emitters in flares were obtained by integrating the plume speed and column density profiles with a combustion efficiency of 85 % and 16 % uncertainty [17]. Temperature and concentrations of H_2O and CO_2

were estimated for an ethylene flame produced by a Hencken burner [18]. Finally, imaging FTIR may also add key fidelity to recent fast framing FTIR studies of detonation fireballs and muzzle flash [8-11, 97].

In the current work, we evaluate the potential of IFTS for monitoring thermal decomposition and combustion in the gas plumes generated by laser irradiation of surfaces containing carbon or hydrocarbon materials. The effectiveness of high energy lasers to render a target nonfunctional depends on propagation of the laser through these evolving gas plumes, heat released in exothermic gas phase reactions, and changes to surface oxidation kinetics [1-3, 14, 20, 21]. Extension of the IFTS instrument to these laser material interactions requires: (1) application to short focal distances (a few meters rather than the kilometer paths used for smokestack and jet/rocket engine observations) [12, 13, 16], (2) high spatial resolution (~ 1 mm sampling for laser spot sizes of 1-10 cm), (3) handling large changes in source radiance (pre and post combustion) and managing the instrument dynamic range, (4) evaluating high gas temperatures (> 2800 K) and large temporal-spatial variations in column density for various materials including graphite, carbon composites, painted metals, and polymers films [22-24], and (5) radiative modeling of complex hydrocarbon spectra and kinetics. In the present work, we demonstrate the first use of IFTS to reveal complex pre-combustion dynamics of the evolved molecular species in the gas phase for laser irradiated fiberglass reinforced polymers (FRP). Following identification of gaseous species in the plume [32], a simplified line-by-line radiative transfer model is developed to obtain spatial maps of temperature and effluents column densities. For a single pixel above the surface, the

temporal dependence of the gas temperature and column densities is developed.

Two-dimensional imaging of combustion plumes above laser irradiated samples in laminar shear flow would be particularly useful in developing specie and temperature profiles in the boundary layer and benchmarking reactive fluid dynamic calculations. For example, the kinetics of combustion above graphite samples in M = 0.2 - 0.9 laminar flows is of particular interest to both the combustion and laser communities. In this application, lateral observations with column densities and temperatures averaged over nearly constant line-of site conditions would lead to well quantified results. However, such studies require high laser fluence, ~ 1 kW/cm^2 to achieve surface temperatures of T = 2000 – 4000 K, and spatial resolution of ~ 0.1 mm. As part of an effort to develop IFTS for this application, we begin with this study of buoyant flow above fiberglass, requiring laser fluences of ~ .04 kW/cm^2 and spatial resolution of a > 1 mm.

Lateral, line-of-sight observations are also necessary for the interpretation of IFTS surface measurements. The estimation of front surface temperatures are complicated by evolving surface emissivity and intervening gas plume emissivity. By monitoring the gas plume from the side, much of the information necessary for separating surface temperature from gas emissions becomes available. The present work seeks to begin the development of IFTS for these applications.

Prior experimental efforts have been aimed to understand the combustion products of composite materials, such as fiberglass reinforced polymers but are rather limited [24, 40]. Fiberglass polymeric materials may contain sizings, binders or flame retardants and organic components [42], resulting in a complex chemical structure [40, 43]. Fiberglass

reinforced polymers are typically epoxy or polyester based, comprised of adhesive joints with many components and multiple interfaces [24, 40]. Landrock et al. [44] described the combustion characteristic of polyester based-FRP as burning with a smoky flame, accompanied by melting, dripping and char formation. Combustion products of polyester-based materials have been reviewed elsewhere [45-47], containing organic components such as C_6H_6 (benzene), $(C_6H_5)_2$ (biphenyl), $C_6H_5CH_2CH_3$ (ethyl benzene), C_5H_8 (pentadiene), $C_6H_5CH{=}CH_2$ (styrene), and $C_6H_5CH_3$ (toluene). It has been reported that these composite materials have a flash-ignition temperature of approximately 648 K and a self-ignition temperature of approximately 758 K [40, 44].

Experimental

An schematic diagram illustrating the experiment set-up is shown in Figure 4. Epoxy fiberglass reinforced composite samples of 6.45 cm^2 were positioned normal to the incident laser beam. A 1064 nm cw Nd:YAG laser with a flat top beam (2.14 cm x 1.80 diameter) heated the surface for 60 s in air at atmospheric pressure with an irradiance of 45 $W/cm^{2.}$ Figure 5a illustrates a visible image of the laser induced hot spot on the fiberglass sample. A room temperature graphite plate was positioned behind the plume for the emission measurements. A fume hood was placed above the sample to slowly vent the plume. Additional details regarding the fiberglass samples have been reported [32].

A Telops, Inc (Quebec, Canada) Hyper-Cam IFTS with spectral response ranging from 1800 to 6667 cm^{-1} (1.5 to 5.5 μm) was used to observe the resulting gas plume. It features a 320 x 256 InSb FPA that was narrowed to a 32 x 32 pixel window size with a

focal distance of 3.12 m. The individual pixel field of view (FOV) was 0.326 mrad, yielding a spatial resolution of 0.9 mm per pixel. A series of modulated intensity images corresponding to optical path differences were collected on the FPA, forming an interferogram at each pixel. Fast Fourier Transform (FFT) of each pixel's interferogram produces a raw spectrum which was calibrated for absolute spectral radiance ($\mu W/(cm^2\ sr\ cm^{-1})$) with two internal wide-area black body sources at 333 and 363 K. Established radiometric calibration procedures are employed to determine the spectrally dependent gain and background for each pixel [19].

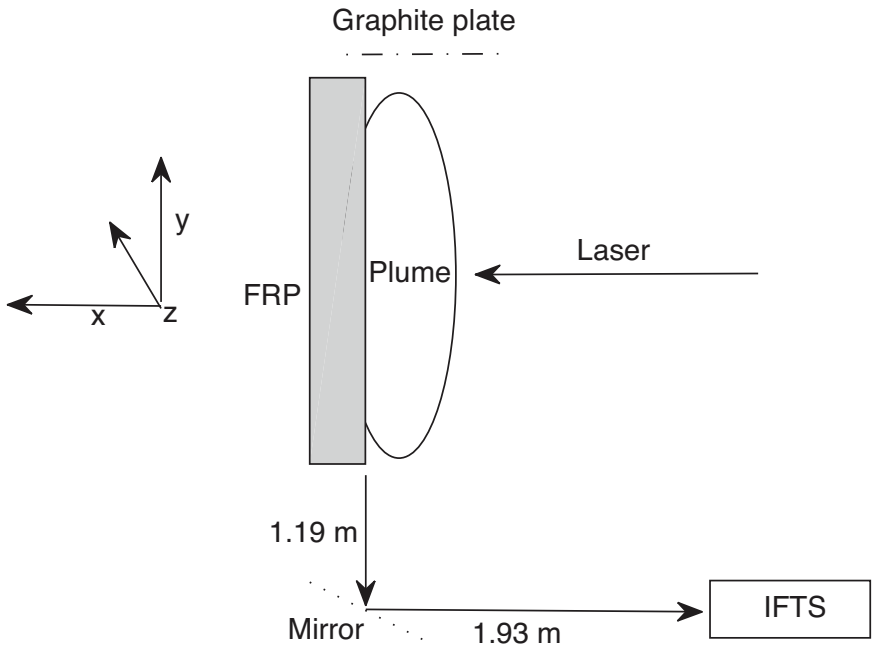

Figure 4. Schematic diagram of the experimental apparatus. The imaging Fourier transform spectrometer is positioned to observe the surface-gas boundary layer, with a spatial resolution of 0.9 mm per pixel. The fiberglass surface is normal to the laser beam, with an irradiance of 45 W/cm^2. A cold graphite plate is positioned within the instrument FOV.

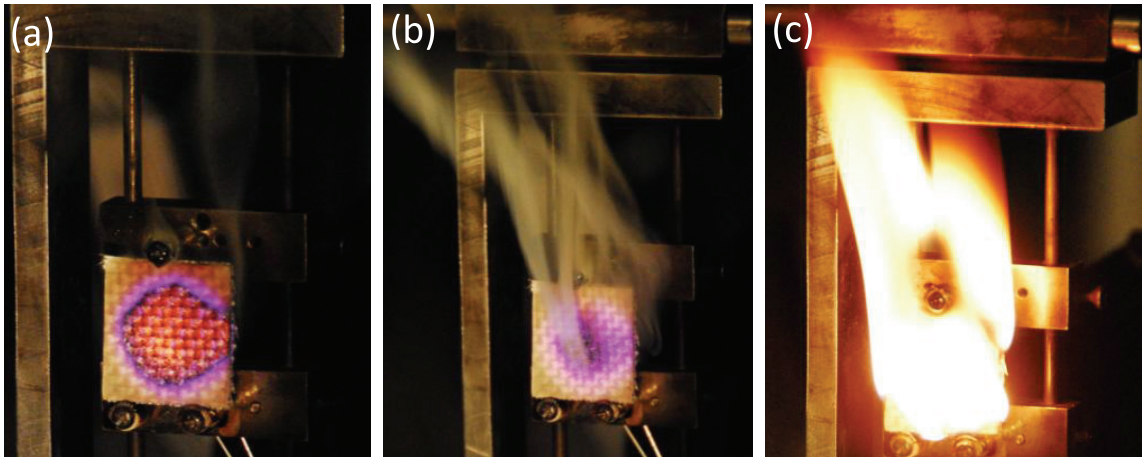

Figure 5. Visible images of: (a) the laser irradiated fiberglass sample, (b) the optically thin, smoky plume before combustion, and (c) the optically thick plume after ignition.

A hyper-spectral data cube was acquired every 0.4 s. Each cube is comprised of a stack of 2D images (32 x 32 pixels in the (x,y) plane) corresponding to different optical path differences. The rate at which a data cube can be acquired is dependent on spectral resolution, FPA integration time, and the number of pixels within the image. In the current work, data was collected with fast framing rates of 50 kHz, spectral resolution of 2 cm^{-1}, and an integration time of 20 µs per frame. The 16-bit FPA using a 0.3 optical density neutral density filter saturates with 65,000 counts at 300 µW/(cm^2 sr cm^{-1}), with a background radiance of 6 µW/(cm^2 sr cm^{-1}). For the typical conditions encountered in this study with gas plume temperatures near 1000 K, the DC component of the interferogram represents 28 % of the dynamic range, with the interferometer producing an 8 % modulation at zero optical path difference (ZPD). Additional instrument details have been reported previously [4, 5].

The imaging properties of the IFTS instrument are defined by optics aft of the interferometer and before the InSb array. The effective focal length is 76 – 86 mm, for objects at 3 m and infinity, respectively. Spatial resolution is approximately twice the diffraction limit, with 73% of the energy at 4.3 μm from an on-axis pixel delivered to a single pixel. Variation in spatial resolution across the central 32 x 32 pixels is less than 1%. The point spread function changes by less than 5% along a 5 cm depth of field.

The pre-combustion plumes are not spatially uniform with unstable, turbulent characteristics as shown in Figure 5b. The IFTS instrument observes emission from a column in the y-direction to produce an image in the (x,y) plane. Temperature and concentration gradients in the y-direction are averaged along this line of sight. A simple radiation transfer model is developed below to interpret the images and report column densities and effective temperatures. The temperatures represent a nonlinear weighting of pixel temperatures along the line of sight with regions of higher temperature and less optical thickness along the path to the sensor weighted more heavily. After ignition, the plume becomes optically thick, as seen in Figure 5c.

Results and Discussion

Spectral Assignments

A single, un-processed image (32 x 32 pixels) captured at an optical path difference of 0.25 cm during laser irradiation at 24 s is shown in Figure 6. The plume structure is clearly evident, with the effect of buoyancy (and the fume hood flow towards the vertical y-direction) observed in the shape of the plume. A square box at (x,y) = (1.8 mm, 12.6 mm) indicates the most intense plume emission and the corresponding un-calibrated

spectrum is provided in Figure 7.

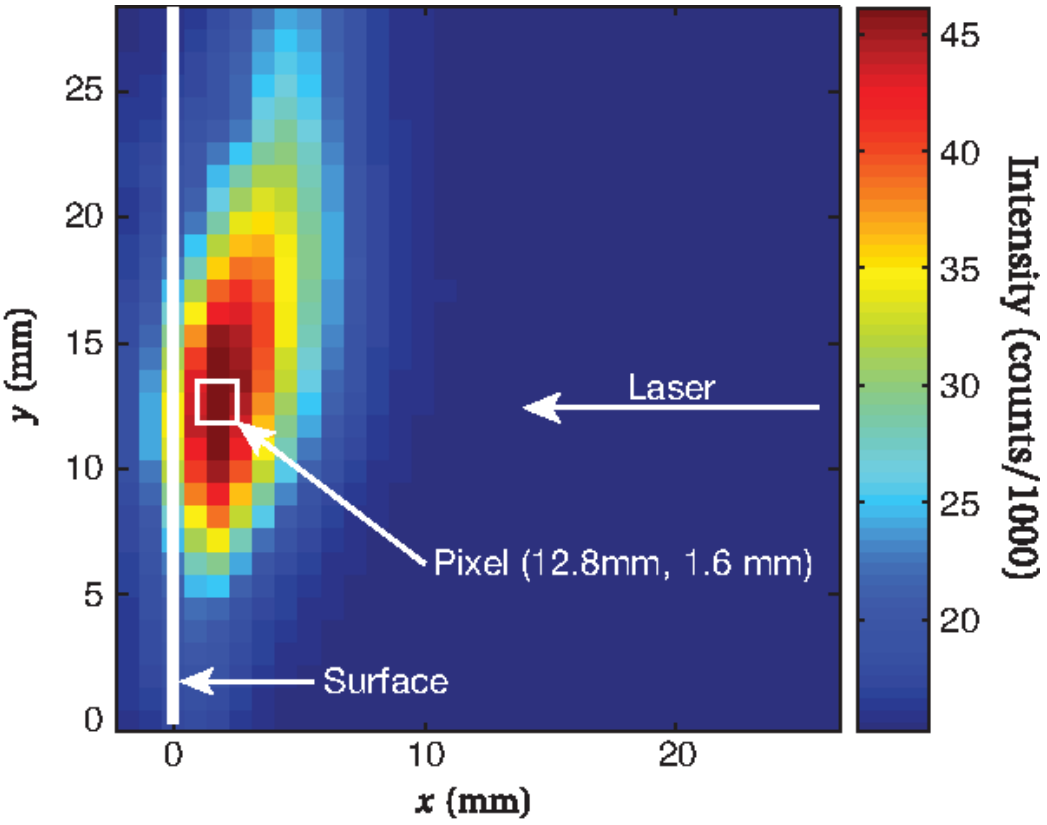

Figure 6. Single broadband image of an interferogram in the far DC wing for laser irradiated fiberglass reinforced polymer at 24 s. The plume extends above the surface 10 mm in the x-direction and above 25 mm in the y-direction.

Emission from gaseous H_2O, CO, CO_2, and hydrocarbon effluents are readily identified by their corresponding rotational-vibrational spectral signatures. The most easily recognizable spectral features are the P- and R- branch emission lines arising from

the fundamental CO band between 2000 cm^{-1} and 2220 cm^{-1}. The R- branch of CO lies near the antisymmetric stretching band of CO_2 (ν_3) and is strongly overlapped with the intense CO_2 spectrum, whereas the P- branch of CO suffers little CO_2 interference [98]. A portion of the CO_2 emissions is highly absorbed by the colder atmospheric CO_2 near ~ 2300 - 2365 cm^{-1}. The wings of the CO_2 bands are less attenuated and produce peaks at 2285 and 2295 cm^{-1} respectively [99]. No significant emissions from the hot CO (2,1) band or hot CO_2 bands are observed at the modest temperatures reported below.

The presence of hydrocarbon (HC) emission was identified between 2800 to 3200 cm^{-1}. The sp^2 and sp^3 orbital for C-H stretching modes occur at 3000 - 3100 cm^{-1} and 2850 - 2960 cm^{-1} respectively. Another interesting feature is the smooth exponential-like baseline that decays from 1800 cm^{-1} at the instrument limit. Several atmospheric water absorption lines are also observed near 1800 cm^{-1}.

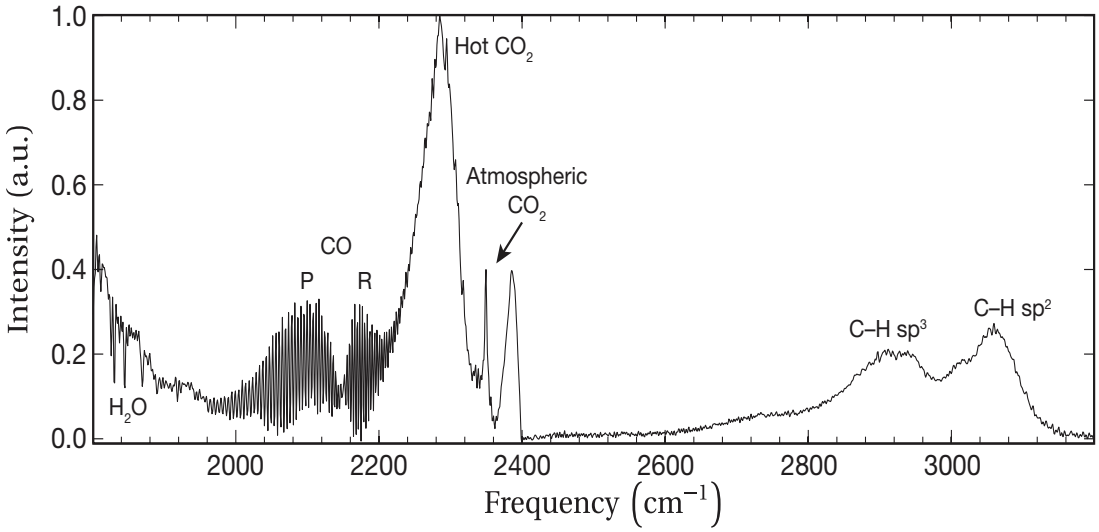

Figure 7. Normalized FTIR spectra for (x,y) = (1.8 mm, 12.6 mm) at 24 s.

Spectral fitting

A simplified line-by-line radiative transfer model (LBLRTM) [26] was developed to extract temperature and column densities from the observed plume spectra. By assuming that the plume is in local thermodynamic equilibrium (LTE), and ignoring scattering, background radiation, and self-emission of the atmosphere, the apparent radiance, L, at a single pixel can be expressed as

$$L(\nu) = \int \tau_{atm}(\nu')\varepsilon(\nu')B(\nu',T)ILS(\nu-\nu')d\nu' \tag{18}$$

where τ_{atm} is the atmospheric transmittance along the 3.12 m path between the instrument and plume, ε represents the plume's spectral emissivity, B is Planck's distribution for blackbody radiation at temperature T, and ILS is the instrument spectral lineshape. The instrument line shape (ILS) function is controlled by the interferogram length and symmetry as well any apodization [100]. For our model no apodization function was applied, and the line shape is the canonical FTS function $ILS(v) = 2a\ Sinc(2\pi av)$, where a = 0.3 cm is the instrument maximum optical path difference (MOPD). Equation 19 assumes a single layer model and the plume path length is taken approximately as the beam diameter where l = 2.43 cm and N is the total gas density.

The spectral emissivity is defined as

$$\varepsilon(\nu) = 1 - \exp\left(-\sum_i q_i N \sigma_i(\nu,T)\right)\tau_p\tau_{emp} \tag{19}$$

where q_i represents the fractional column density as $q_i = \xi_i\ l$, ξ_i is the ith species volume mixing fraction, and l is the path length through the plume. The absorption cross-section

σ_i for the i^{th} molecule is computed using the HITEMP [101] extension to the HITRAN [102] spectral database and includes the temperature dependent partition function. Two models for particulate (soot) transmittance, τ_p, are used: (1) emissivity is independent of frequency (greybody) and (2) the logarithmic polynomial in wavelength dependence of reference 103. The last term in Equation 20, $\tau_{emp} = exp\ (-A)$ where A is defined as the product of a Gaussian function with linear baseline:

$$A(\nu) = \exp\left[-\frac{(\nu - c_2)^2}{c_3}\right] \bullet \left(c_1 + c_4 \nu\right) \tag{20}$$

was included as an optional parameter to improve fitting in the region of the CO band. By including a small rise in the baseline near c_2 = 2100 cm^{-1}, a small fit residual associated with a difference in the intensities of the P- and R- branches of the CO band can be avoided. The identity and impact of this empirical emissivity term on the fit column densities and temperature is discussed below.

Figure 8a illustrates the calibrated radiance for the 2000 - 2400 cm^{-1} region where the CO and CO_2 features are clearly evident. Best estimates for the column density, plume temperature, and particulate emissivity were obtained from a nonlinear fit of Equation 18 to the spectrum using a Levenberg-Marquardt algorithm. We allow T, ξ_i, the baseline parameters c_1-c_4, τ_p, and the atmospheric CO_2 absorption ξ to be real positive free fit parameters. Systematic errors associated with the radiative transfer model were evaluated by examining the dependence of the fit parameters and quality of the fit on: (1) the empirical emissivity τ_{emp}, and (2) the soot emissivity model.

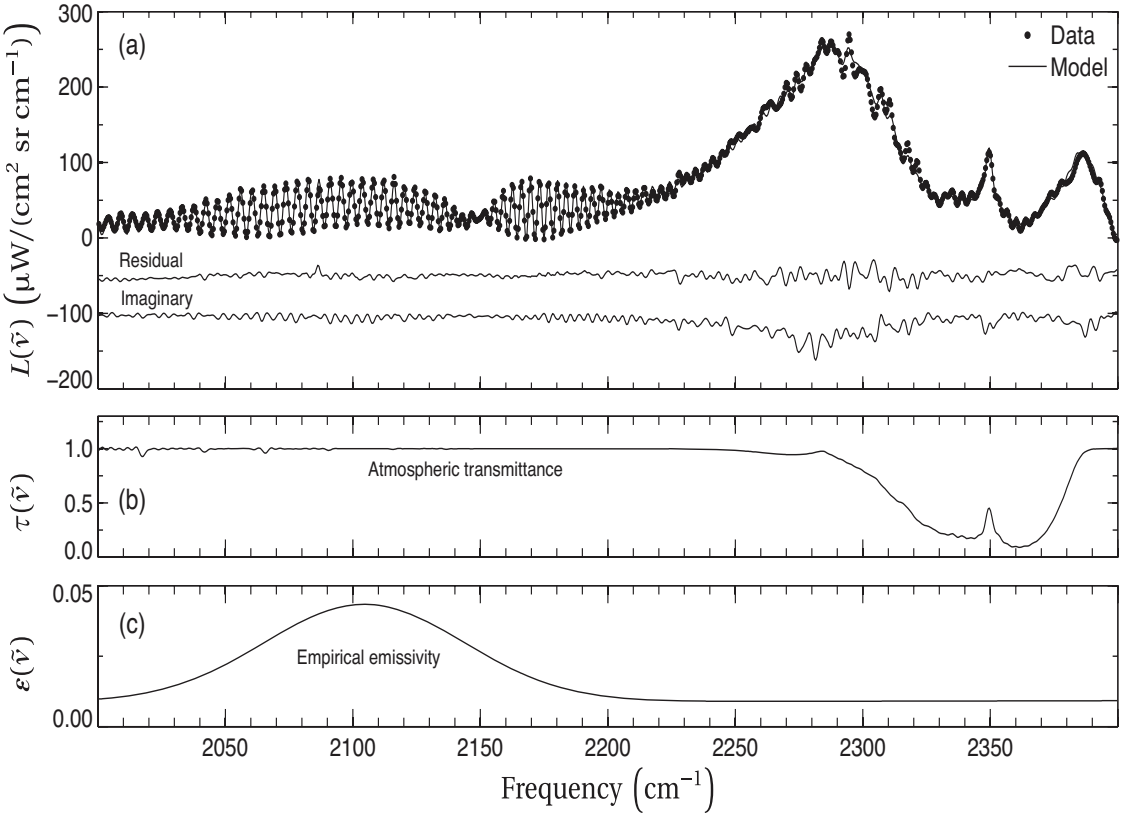

Figure 8. (a) Data, model, fit residual, and imaginary component of the spectrum at t = 24 s for (x,y) = (1.8 mm, 12.6 mm) in the spectral region between 2000 - 2400 cm^{-1}. Fit results were T =1019 ± 7 K, q_{CO} = 1.14 ± 0.05 x 10^{18} CO molec/cm^2 and q_{CO2} = 1.11 ± 0.03 x 10^{18} CO_2 molec/cm^2. (b) Atmospheric transmittance profile for 3.12 m path between the plume and the instrument with atmospheric CO_2 concentration of 369 ppm. (c) Empirical emissivity to possibly account for -C ≡ C- stretch.

Figure 8a shows the data and fit at 24 s after the beginning of laser irradiation for a pixel near the center of the laser spot and 2 pixels (1.8 mm) from the surface. The

radiative transfer model included the empirical emissivity, τ_{emp}, and the grey body soot emissivity. The best fit yields an effective temperature of $T = 1019 \pm 7$ K, and effective column densities of $q_{CO} = 1.14 \pm 0.05 \times 10^{18}$ molec/cm^2 and $q_{CO2} = 1.11 \pm 0.03 \times 10^{18}$ molec/cm^2. The reported statistical uncertainties for all the results are defined as the half-width of the 95% confidence interval and do not include systematic errors associated with the assumption of a homogeneous plume or the effects of turbulence. The particulate transmittance τ_p is ~ 1, consistent with a small soot volume mixing fraction. The transmittance profile for the atmospheric path length of 3.12 m is shown in Figure 8b. Atmospheric CO_2 absorption is seen from 2300 to 2400 cm^{-1} with a mixing fraction of 480 ppm.

The residuals are a small fraction of the observed radiance with a root mean square error (RMSE) of less than 0.198 $\mu W/(cm^2\ sr\ cm^{-1})$. The imaginary component of the FTIR provides an estimate of the noise level of the instrument. The RMSE for the imaginary component is 0.240 $\mu W/(cm^2\ sr\ cm^{-1})$, somewhat greater than the fit error.

The high quality fit requires a small contribution from the empirical Gaussian of Equation 20 with peak emissivity of 0.04, as seen in Figure 8c. Without this empirical modification, the fit RMSE is 1.35 greater than with the empirical emissivity, the fit temperatures are reduced by 67 K, and the column densities of CO_2 and CO are increased by a factor of 1.4 and 2.3, respectively. The affect of the empirical emissivity is greater for pixels downstream of the irradiated spot. At (x,y) = (2.7 mm, 17.1 mm) where the change in fit temperature excluding the empirical emissivity is – 128 K, and column densities of CO_2 and CO are increased by a factor of 2.0 and 2.9, respectively.

We tentatively attribute this additional intensity near 2100 cm^{-1} to emission from triple carbon bond, hydrocarbon emission. The presence of -C ≡ C- stretching has been reported for RC≡CH between 2080 - 2140 cm^{-1}, RC≡CR between 2080 - 2140 cm^{-1}, and RC≡C-C RC≡CR' between 2200 - 2270 cm^{-1} and 2080 to 2140 cm^{-1} [104]. These spectral features are not included in the HITRAN database and appear to be the most likely contribution to the minor CO P- branch asymmetry. For example, the spectrum for 1-octyne at room temperature is shown in Figure 9a [105]. Also shown is the fit empirical emissivity of Equation (20). The spectral location of the empirical feature corresponds with the hydrocarbon feature. The width of the empirical emissivity at T = 444 K is 1.27 times greater than the reference spectrum at room temperature, as might be expected from population of higher rotation levels at the elevated temperatures in the present work. The width of the empirical emissivity at T = 848 K increases to 2.44 times the reference spectrum width. Furthermore, the amplitude of the empirical emissivity systematically trends with gas temperature as shown in Figure 9b. At gas temperatures up to 900 K, the emission is steady, and then decreases by a factor of ~ 4, with little impact on the radiative transfer model.

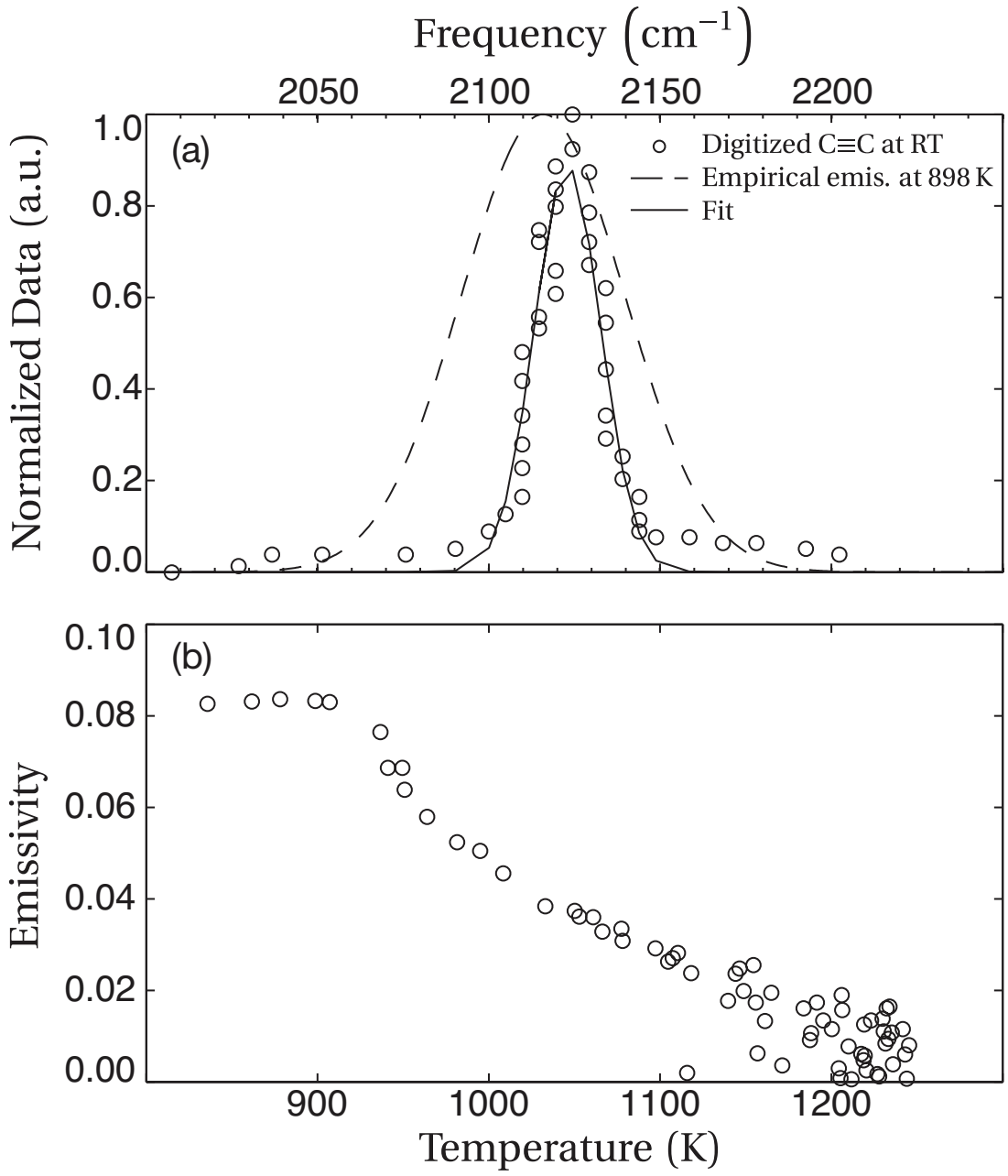

Figure 9. (a) Comparison of (o) -C≡C- spectra from 1-octyne at room temperature (RT) [105] with (---) empirical emissivity of equation (3) for the pixel (x,y) = (1.88 mm, 12.6 mm) at 24 s, with temperature T= 898 K, and (b) peak amplitude of empirical emissivity, $A(\nu=c_2)$, as effective plume temperature increases.

The observed emissivity may also be driven by the multi-layer nature of the plumes and errors in extrapolating the HITRAN [102] and HITEMP [101] database to high temperature. HITEMP underestimates the band wings of the 4.3 μm fundamental asymmetric CO_2 band at temperatures above 2000 K [101, 102, 106-108]. However, significantly lower temperatures were observed in the present work. The imaginary component of the Fourier transform seems to mirror some of the CO_2 spectral features from 2250 to 2400 cm^{-1}, indicative of scene change artifacts attributable to the dynamic nature of the plume. Their small magnitude indicates that the real part of the spectrum is likely unaffected by these artifacts [12, 109]. Further analysis of the empirical emissivity is outside the scope of the current results, and a detailed examination will be subject to future work.

The sensitivity of the fit parameters to soot model is rather weak. The emission intensity at 2400 – 2500 cm^{-1} is low and largely due to soot. With a soot volume fraction constrained at 0.2 %, the modeled intensity in this spectral region is more than four times larger than observed. Even at this high soot fraction, the choice of soot model influences temperature extraction by less than 7 K and column densities by less than 5%.

In summary, we prefer the radiative transfer model with the empirical emissivity representing hydrocarbon emission and gray body soot emissivity for simplicity. The spatial and temporal descriptions of the plume developed below are based on this version of the model. The effective temperatures represent a nonlinear weighting along the IFTS line of site.

Spatial Maps of Temperature and Concentrations

Spatial maps of the fit temperature from LBLRTM, are compared with the brightness temperature (T_b) at ν = 2295 cm^{-1} in Figure 10. Figure 10a shows the plume temperature from the LBLRTM calculation. Temperature is highest at the edge of the surface (T > 1100 K). The temperature declines as the plume expands away from the surface and hot gases rise, driven by buoyancy and fume hood flow rate. The laser spot is centered at y = 12.6 mm and extends from y = 2.7 - 24.3 mm. The statistical fit uncertainty in temperatures are small ΔT < 35 K, and on average ΔT = 7 K in the region where the temperature exceeds 900 K. The brightness temperature is defined by:

$$T_b = c_2 \left(\frac{\nu}{\ln\left(\frac{c_1 \nu^3}{L(\nu)+1} \right)} \right) \tag{21}$$

where c_1 and c_2 are the first and second radiation constants, respectively, $L(\tilde{\nu})$ the apparent radiance or calibrated spectra and ν is the corresponding wavenumber. The spatial map for T_b, corresponding to the hot CO_2 peak at 2295 cm^{-1} is shown in Figure 10b. The brightness temperature is influenced by both the plume temperature and effluents concentration. The fit temperature is ~ 50 % greater than the brightness temperature, T_b, consistent with an emissivity for the hot CO_2 peak of ε ≅ 0.2.

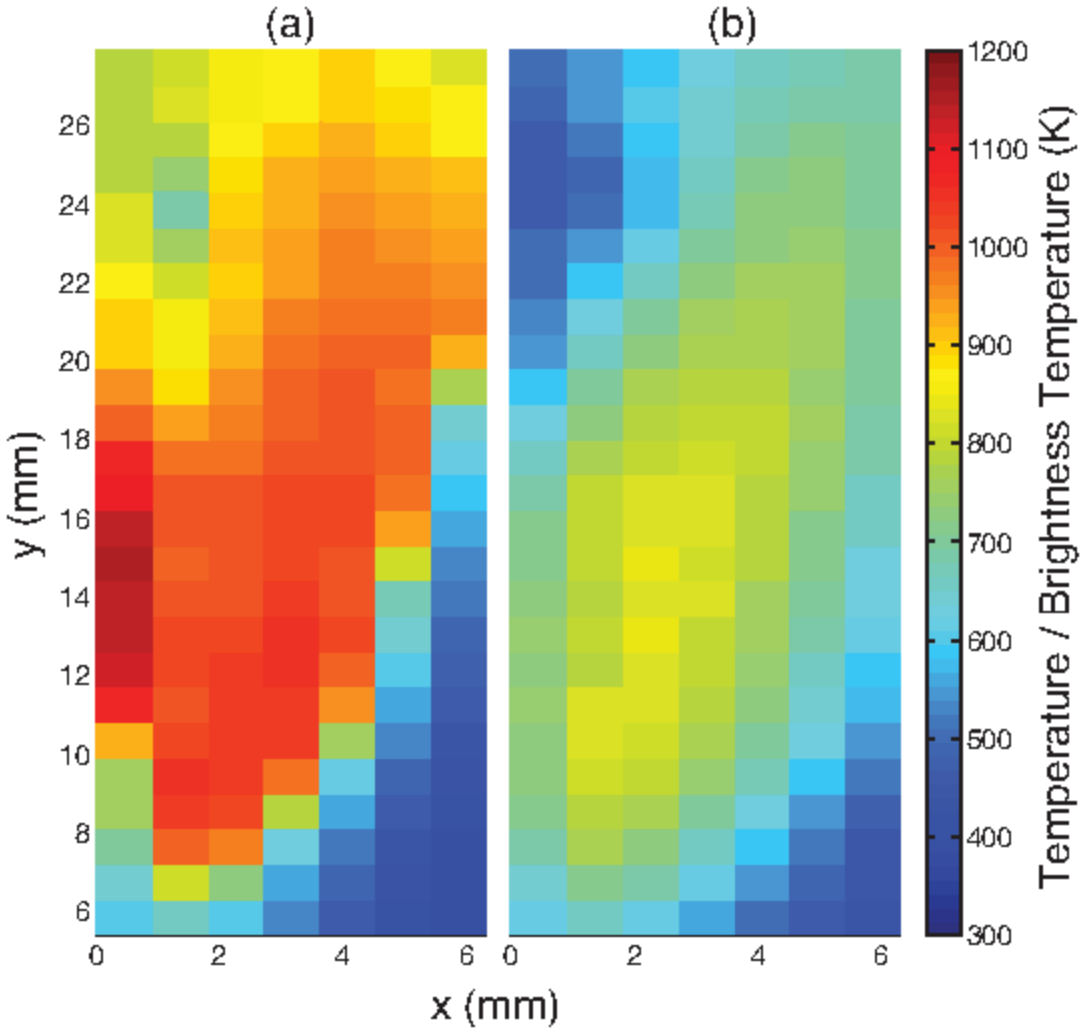

Figure 10. Spatial maps of the: (a) Fit plume temperature, *T* obtained from the LBLRTM calculation at t = 24 s, (b) Brightness temperature that correspond to a hot CO_2 peak at 2295 cm^{-1}.

The corresponding column densities for CO and CO_2 are provided in Figure 11. At the center of the plume the fit uncertainties are small, typically < 4 %. The spatial maps for temperature and column densities are temporally resolved at 0.406 s per frame.

The pre-combustion densities are significant, ~ 10^{18} molec/cm^2 and comparable to those observed in laminar flames with good combustion efficiency [18]. Note that the maximum column densities are observed at 2 mm away from the surface where the temperature has decreased by about 90 K. At t = 24 s the CO/CO_2 ratio ~ 1:1 and fairly uniform spatially. The molecular species travel upward driven by buoyancy and fume hood flow, with the maximum extent of the plume perpendicular from the surface of about 5 mm. The hotter region of the plume extends in the vertical direction to y ≅ 25 mm, x ≅ 3 mm above the laser irradiated region.

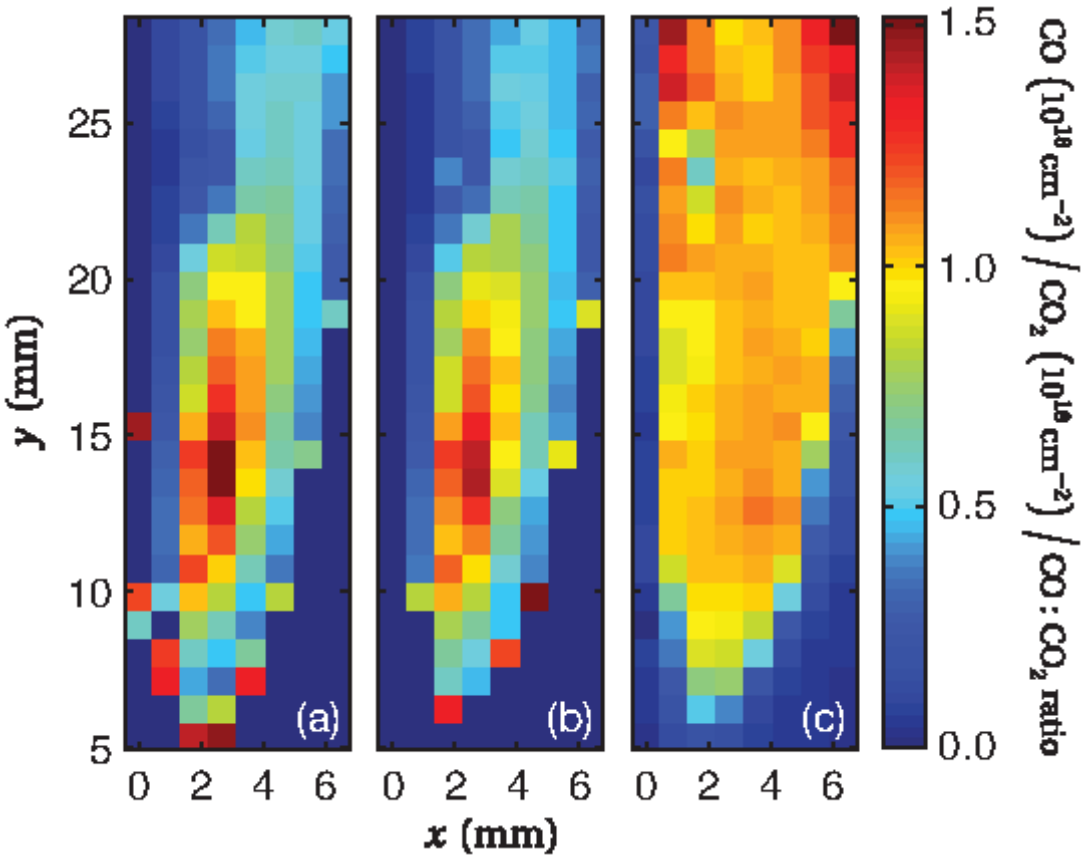

Figure 11. (a) Spatial maps of column density of CO, and (b) CO_2 (middle panel) in units of (10^{18} molec/cm^2). (c) Corresponding map of the [CO]/[CO_2] column density ratio.

To partially illustrate the evolving plume, the temporal dependence of temperature and column densities for a single pixel is explored in Figure 12. The temperature slowly rises from ambient conditions to steady value of ~ 1140 K in about 30s. Sustained combustion occurs at 49s for the unpainted fiberglass samples and the temperature rises by ~ 30%. Painted fiberglass composite targets were studied previously and self-ignite earlier (t = 45s) than the unpainted fiberglass targets (t = 49s) [32]. The dynamic range of the IFTS instrument is limited by the DC component and modulation depth, so both pre-combustion and post combustion images cannot be obtained with the same instrument settings. The pre-combustion data correspond to the pixel (x,y) = (1.8mm, 12.6mm) and the combustion plots are for (x,y) = (6.3mm, 12.6mm). The edge of a combustion flame reacts continuously with the atmosphere and exhibits the highest turbulence. Therefore temperature fluctuations will be more evident at the edge than at the center of the combustion plume.

Combustion ignition temperatures depend significantly on both fiberglass composition and heating rates [24]. This previous study has shown that melamine fiberglass readily combusts at surface temperatures of ~ 620 K. Epoxy and silicone fiberglass are more resistant, requiring surface temperatures of ~ 1030 K and ~ 1170 K, respectively. However, the epoxy fiberglass combustion temperature is significantly reduced to ~ 830 K for radiant heat fluxes of 30 W/cm^2 [24]. For our current epoxy fiberglass samples, with laser irradiation of 45 W/cm^2, the gas temperature rises for an extended period to a steady value of ~ 1140 K and when combusting the plume temperature reaches 1300 K. However, the surface temperatures are lower.

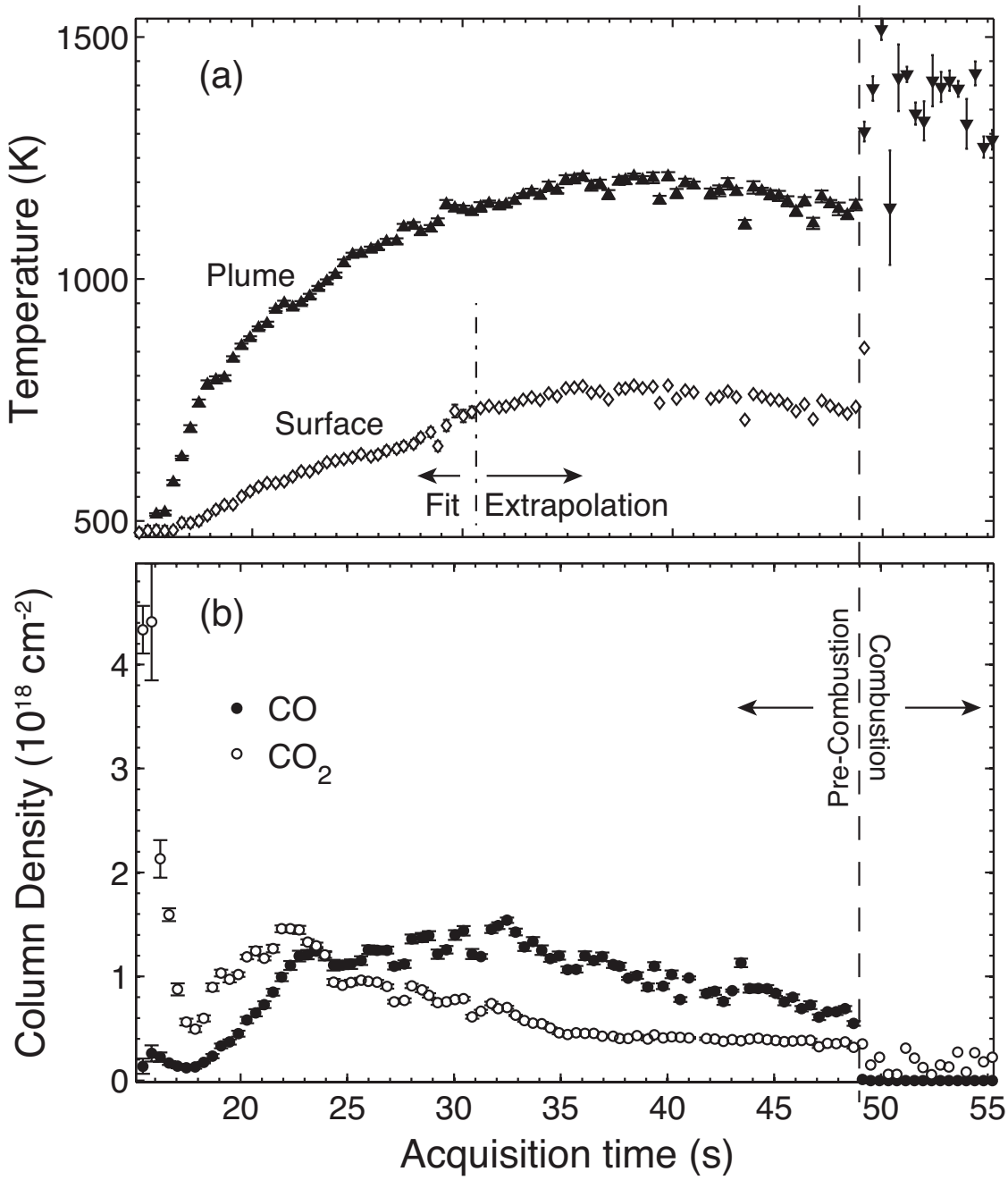

Figure 12. (a) Temporal evolution of plume and surface temperature and (b) temporal CO, CO_2 column densities for t $\geq$ 15 s. The pre-combustion data is for (x,y) = (1.8 mm, 12.6 mm) and the combustion data is reported for (x,y) = (6.3 mm, 12.6 mm).

Surface temperatures are determined to within ± 6 K from a Planckian fit of the blackbody emission at the edge of the fiberglass sample. The surface temperature rises to ~ 700 K at t = 31 s, about ~ 65% of the plume temperature. Due to the instrument dynamic range limit, surface temperatures for t > 31 s are extrapolated from the correlation (r^2=0.98) between the gas plume and surface temperatures. The resulting FRP surface temperature at combustion is ~ 856 K, comparable with reported epoxy fiberglass combustion temperature of 830 K at a 67% lower irradiance [24].

Induction times for FRP combustion can be quite long, particularly for lower heat fluxes. Heat fluxes of 1 - 4 W/cm^2 applied to polypropylene fiberglass induce combustion with delays of 100 - 1000 s [110]. For modest flow rates, ~ 1 m/s, ignition delay times are controlled by the pyrolysis rate and occur when a minimum concentration of hydrocarbon is attained in the gas phase.

Carbon monoxide and hydrocarbon concentrations are often highly correlated and corrections to combustion efficiency based on these correlations have been developed [111]. There is a strong correlation between carbon monoxide and HC concentrations in the present study as shown in Figure 13, where the fit CO column density and the spectrally integrated intensity for the C-H stretching feature are compared. The database for radiative transfer modeling of complex hydrocarbon spectra is rather limited and insufficient for our spectral fitting. An increase in the HC thermal decomposition in the gas phase occurs between 15 - 19 s. The initial production of CO is delayed from the HC evolution by a few seconds. Hydrocarbon emission peaks at t = 20s, where a temperature rise of ~ 520 K and 792 K occurs in the surface and gas plume, respectively. At

temperatures between T = 520 - 770 K, emission of organic fuels and aromatic compounds occurs and the duration of this phase is determined by the amount of available fuel in the material [111].

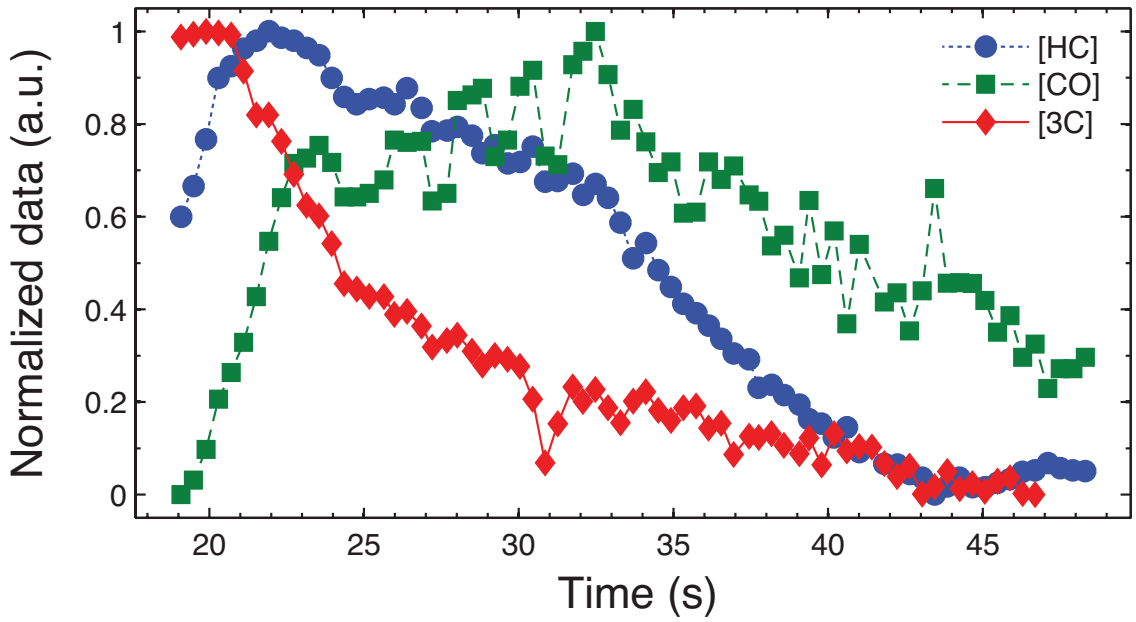

Figure 13. Temporal correlation between the pre-combustion concentrations for: (□) CO, (O) HC, and (◇) –C≡C- at (x,y) = (1.8 mm, 12.6 mm).

The spatial and temporal dependence of the evolved gas phase products are rather complex and the current qualitative observations are not well organized by established kinetic mechanisms. Initially the CO_2 concentration is much higher than the CO and hydrocarbon emissions, suggesting a pyrolysis rather than standard combustion mechanism. As the surface temperature rises above 700 C, the out-gassing of hydrocarbons and CO production rates significantly increases, but the CO_2 production

still exceeds the carbon monoxide. As the surface temperature begins to stabilize, the hydrocarbon and CO production declines, possibly due to depletion of volatile organics in the sample. Despite the surface temperature stabilization and the decline in gas phase fuel, combustion is delayed for another 10-20s. For all but the earliest portion of the plume evolution, the combustion efficiency, estimated by the ratio of CO_2 to CO + CO_2 concentrations is low, < 50%, consistent with the smokey, pre-combustion nature of the plume. Upon ignition, the CO concentration is greatly reduced and the combustion efficiency exceeds 98%, as expected. The spatial dependence of the emission is inconsistent with heterogeneous, surface oxidation to produce CO, followed by gas phase oxidation to produce CO_2. Prior to combustion, both CO and CO_2 emissions peak at ~2 mm from the surface and the ratio is relatively uniform spatially. The weak spatial variation suggests the CO/CO_2 ratio increases farther from the surface.

The current results appear qualitatively consistent with the prior fire hazard study [24]. The combustion efficiency for fiberglass can be low, < 50 %, even for sustained flames. For epoxy fiberglass, CO_2 concentrations are initially somewhat larger than CO, but the ratio quickly reverses and CO can exceed CO_2 by more than 30 % at peak combustion [24]. Kinsella et al. [24] report the evolution of hydrocarbons (i.e. C_6H_6, CH_2O and C_2H_2) occurs first, then CO and CH_4 (for silicone FRP). While these two studies appear qualitatively similar, a unified set of kinetic mechanisms remains elusive. In short, the mechanisms controlling the gas plume from these laser irradiated surfaces are unclear and require further analysis.

Conclusions

A first quantitative analysis of emissive plumes from laser irradiated fiberglass composite surfaces was developed from fast framing hyperspectral observations. Based on the characteristic FTIR spectra of effluents in the plume, we readily identified H_2O, CO, CO_2, and hydrocarbon species as combustion products of FRP. Moreover, the development of a simplified radiative transfer model illustrates time dependent, spatial maps of temperature and column densities. The use of a single-layer plume model to retrieve species column densities proved to be an adequate approximation. However, a small structured residual on the red side of the CO_2 emission requires further interpretation. The temporal evolution of temperature and column density demonstrated the feasibility of using IFTS to study the kinetics interplay between CO and CO_2 spatially throughout laser irradiation. A detailed evaluation of pyrolysis kinetics is complicated due to the chemical structure of the epoxy fiberglass composite. However, our observations were validated with prior FTIR fiberglass study [24] where initial larger concentrations CO_2 are somewhat larger than CO. We intend to explore the gas phase combustion for porous graphite targets where well-established kinetic models exist to enable detailed kinetic and fluid dynamic modeling.

IV. Thermal Degradation of Poly(methyl methacrylate) with a 1.06 µm Nd:YAG Laser in a Buoyant Flow

Preface

The laser radiative oxidative decomposition of PMMA and the evolved decomposition products in the gas-phase are investigated from Fourier transform infrared (FTIR) spectroscopy. The spatial and temporal evolution of the gas plume from laser irradiated poly(methyl methacrylate) (PMMA) in air were investigated primarily from imaging-FTIR with adequate spatial (0.81 mm^2 per pixel) and spectral resolutions (2 cm^{-1}). Bulk surfaces of black PMMA samples were irradiated from 4 - 22 W/cm^2 with a 1.064 µm Nd:YAG laser. Strong spectral emission of methyl methacrylate (MMA) was observed in the infrared. Spatial maps of plume temperature and MMA column density were obtained from modeling the observed spectra by assuming a homogeneous single-plume radiative transfer model (RTM). The spectral model was used to compute the gas emissivity from experimentally measured, interpolated and extrapolated MMA absorption coefficient database. The spectral radiance from the irradiated PMMA surface at 22 W/cm^2 was fitted with Planck's distribution to obtain temporal and spatial surface temperature profiles. The flat beam laser profile is shown along a row of pixels from the spatial surface temperature map. Laser irradiated PMMA reached a steady surface temperature of 613.9 ± 0.8 K and an effective gas-phase temperature of 700 ± 19 K at 22 W/cm^2, obtained from the RTM. The reported statistical uncertainties for all the results are defined as the half-width of the 95% confidence interval and do not include systematic errors associated with the assumption of a homogeneous plume or the effects

of turbulence. At the surface-boundary layer, plume temperature was higher at the lower irradiance of 4 W/cm^2. As power density increased, gas temperature decreased at the surface-boundary layer. The peak signal-to-noise exceeded 50:1, allowing plume temperature and MMA column density determinations with low statistical errors. A simplified thermal analysis was developed to understand the wavelength dependent surface heating rates from using both CO_2 and Nd:YAG lasers. The surface gas-phase boundary layer kinetics of laser-irradiated PMMA at 22 W/cm^2 was investigated. An Arrhenius plot of MMA formation at the surface for a single pixel was compared against established kinetics models. At surface temperatures of 450 to 600 K, an effective activation energy of 30.83 ± 8.29 kJ/mol was obtained. This effective activation energy is rather consistent with surface desorption of the monomer. Therefore at the 22 W/cm^2 irradiance, vaporization and desorption kinetics described the rate of production of MMA from the laser irradiated PMMA surface.

Introduction

Poly(methyl methacrylate) (PMMA) is an inexpensive thermoplastic that decomposes at ~ 493 K [64]. In the presence of oxygen, the main decomposition product is the monomer methyl methacrylate (MMA) [65]. Molecular oxygen exerts a stabilizing effect on PMMA against depolymerization at low temperatures [66-68], thus increasing the initial decomposition temperature when compared to that for thermal degradation in an inert gas. Methyl methacrylate further decomposes to combustible gaseous hydrocarbon species. These hydrocarbon fuels react with oxygen leading to produce CO,

CO_2 and H_2O from combustion. The thermal decomposition of PMMA is a zero or first-order kinetics process and has been reviewed in detail elsewhere [69].

Fourier transform infrared (FTIR) spectroscopy has been used to investigate the time dependent thermal degradation of polymers [112]. Recently, imaging Fourier transform spectroscopy (IFTS) demonstrated the ability to monitor the thermal decomposition products from laser irradiated fiberglass reinforced polymers at high spatial resolutions (0.81 mm^2 per pixel) [25]. The use of IFTS at short focal distances allows evaluating temporal and spatial variations of the evolved molecular species in the gas phase, the imagery allows correlating the fluid dynamics to the thermal degradation kinetics of polymers. Since PMMA predominantly depropagates to its monomer as a result of thermal degradation, it is important to monitor the infrared emission of MMA with high fidelity. The principal infrared bands of gaseous MMA have been reported previously and are summarized in Table 4 [113].

Table 4. Principal infrared bands of MMA [113]

Wavenumber (frequency)	Characteristic bands
820 cm-1 (12.2 μm)	C-H and C-O-C deformation
950 cm-1 (10.5 μm)	
1035 cm-1 (9.7 μm)	=CH (out of plane bending)
1170 cm-1 (8.5 μm)	C-O stretching
1310 cm-1 (7.6 μm)	
1440 cm-1 (6.9 μm)	CH_3- bending
1730 cm-1 (5.8 μm)	C=O stretching
2940 cm-1 (3.4 μm)	CH_3- stretching

Radiative transfer models allow accurate quantification of temperature and column densities from the observed plume spectra with low statistical errors [25, 114].

For fiberglass reinforced polymers, a simple spectral model describing the apparent plume radiance was developed to quantitatively interpret a pixel's spectrum in terms of the temperature and column densities of the emissive plume molecular species [25]. Radiative modeling requires *a priori* knowledge of the absorption cross section of the emitted products for accurate spectral quantification. Although the HITRAN [102] spectral database contains a comprehensive collection of spectroscopic parameters to compute the absorption cross-section for several molecules, complex hydrocarbon molecular species are not currently included. The oxidative thermal degradation of polymers usually results in complex kinetics with emission from molecular species not readily available in the current spectral databases. Park et al. [113] investigated the infrared radiation properties of MMA from statistical narrow band models to fit the measured FTIR spectra. The monomer column density can also be estimated from total band emissivity calculations from Park et al. [113] as well from radiative transfer models. In the present work these two methods are not compared for systematic errors on their quantitative estimations.

Laser lethality experiments with PMMA have been reported with continuous wave (CW) CO_2 lasers at the longer wavelength of 10.6 μm [51-56]. However, few studies have been conducted at the near-infrared wavelength of 1.06 μm [57-59]. This is primarily due to the poor absorption characteristics of organic materials in this region. Consequently, pigments are commonly added to acrylic thermoplastics to increase absorption in the near-IR. When polymers are irradiated in the longer infrared wavelength, the incident energy is mostly absorbed within a few micrometers from the

surface. According to Said-Galiev and Nikitin [61], this in-depth absorption follows the Beer-Lambert law as defined by Equation (1), where, $I(z)$ is the irradiance (W/cm^2) at depth z (cm), I_0 is the incident irradiance (W/cm^2), and α is the absorptivity (cm^{-1}) of the material. Typically, polymers have low thermal conductivity, which means that the effects related to ablation are surface effects. Therefore the kinetics and mechanism of laser irradiation vary depending on the chemical structure and thermophysical properties of the material. The absorptivity of clear PMMA varies depending on the type of laser wavelength used, a value of 250 cm^{-1} was obtained with a CO_2 laser (10.6 μm), whereas values of ~ 25 cm^{-1} were assumed for hydrogen fluoride (HF) and deuterium fluoride (DF) chemical lasers with wavelengths of 2.7 μm and 3.8 μm respectively [62]. When thermoplastic polymers were irradiated with a CO_2 laser, Cozzens and Fox [63] reported that no breakdown ocurred between 3-7 W/cm^2, but at 5-11 W/cm^2 softening occurred. At a higher irradiance of ~ 22-25 W/cm^2, the material decomposed and vaporized. Since the thermal degradation of PMMA with a CW 1.06 μm Nd:YAG laser has not been thoroughly investigated, this effort aim to explore the spectral emission of the surface-plume boundary layer from IFTS.

The objective of the present work was to investigate the thermal degradation of black PMMA with a Nd:YAG laser at radiative fluxes between 4 to 22 W/cm^2. The evolved gas phase plume was monitored through FTIR measurements. Following spectral identification of emissive plumes in the infrared, a simplified single layer LBLRTM was developed for quantification of spatial and temporal variations in plume temperature and molecular column densities from IFTS. Also, non-imaging long wave

infrared (LWIR) FTIR was employed to investigate the temporal evolution of effluents in the gas phase. The influence of radiative flux was investigated to understand the laser effects on the thermal degradation of PMMA. The effect of plume bending due to buoyancy is correlated between the infrared imagery and spatial maps of temperature and column density as a function of power density. To our knowledge, we present the first two-dimensional spatial maps on the evolved plume temperature and MMA concentration profiles from the surface-boundary layer of laser irradiated PMMA. A kinetics interpretation from established models was made based on the statistical results from the spectral fit of the irradiated surface at 22 W/cm^2.

Experimental Methods

Black plexiglass®, PMMA with carbon black pigmentation samples, were irradiated by a cw Nd:YAG 1.06 μm laser at 4 – 22 W/cm^2 in air at atmospheric pressure for 70 – 420s. The nearly flat top beam with 2.42 cm diameter nearly filled the 6.45 cm^2 square and 1.27 cm thick samples. Approximate values for various properties of black PMMA are provided in Table 5. The absorption coefficient or absorptivity of a material is wavelength dependent. At 10.6 μm (CO_2 laser radiation), the absorptivity of black PMMA is ~ 100 cm^{-1} [56]. However at 1.06 μm (Nd:YAG laser radiation) it has been reported between ~ 0.25 to 4.5 cm^{-1}, depending on the amount of carbon-black pigmentation in PMMA, from 0.01 to 1 % by weight respectively [57, 58].

Table 5. Thermo-physical properties of black PMMA

Name	Symbol	Value	Units	Reference
Density	ρ_{PMMA}	1190	kg/m^3	[115]
Surface conductivity	k	0.188	W/(m K)	[115]
Heat capacity	c_p	1465	J/(kg K)	[115]
Absorption coefficient	$\alpha(10.6\ \mu m)$	100	cm^{-1}	[56]
	$\alpha(1.06\ \mu m)$	0.25 – 4.5	cm^{-1}	[57, 58]
Reflectivity	$R(10.6\ \mu m)$	5	%	[56]
	$R(1.06\ \mu m)$	50	%	[57, 58]

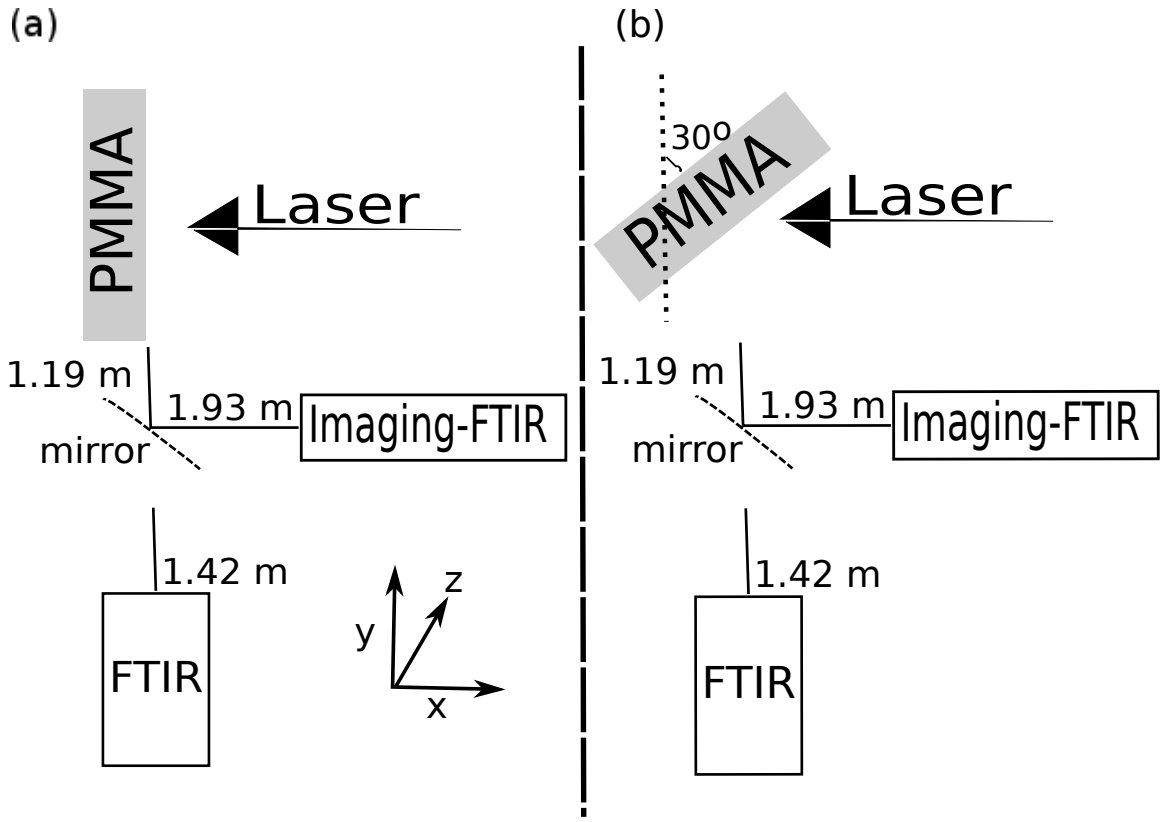

Figure 14. Schematic diagram of the experimental set-up for the (a) side-view experiments (b) sample rotated at 30° to investigate the surface at 21.7 W/cm^2. Non imaged FTIR focal distance of 1.42 m is from the instrument to PMMA target.

The evolution of the non-combusting, gas plume was monitored with both an imaging mid-wave infrared Fourier-transform spectrometer (IFTS), and non-imaging high-speed mid- and long-wave Fourier-transform spectrometer (FTS) perpendicular to the laser axis. The majority of the experiments were design to view the gas plume in front of the sample surface with the laser incident normal to the surface, as illustrated in Figure 14a. A few experiments were conducted with the sample rotated at 30° so the surface temperature could be observed, as shown in Figure 14b. For these surface observations, larger samples of 2.54 cm x 5.08 cm were employed to allow for the same illuminated area.

The IFTS has been described in some detail previously [4, 5]. The 16-tap InSb focal plane array (FPA), with spectral response from 1800 to 6667 cm^{-1}, was narrowed to the central 32 x 32 pixels. With a focal distance of 3.12 m, the spatial resolution is ~ 0.81 mm^2/pixel. A series of 9480 (number of optical path differences samples) modulated images comprise a double-side interferogram on each pixel as the mirror path difference is scanned by 0.3 cm (2 cm^{-1} spectral resolution). A hyperspectral data cube is acquired every 0.3 s. A neutral density filter of optical density 0.3 was employed to avoid camera saturation. Typical signals at zero optical path difference (OPD) were 15,000 counts, or 24 % of the camera's dynamic range. Two wide area blackbody sources at 363 K and 473 K were used to calibrate the instrument for absolute units of spectral radiance [116]. Spectral resolution was degraded to 16 cm^{-1} for the surface observations, improving the temporal resolution to 0.08 s per hyperspectral cube.

Non-imaged FTIR spectra were collected using an ABB BOMEM MR-304 spectrometer at higher spectral resolution of 0.6 cm^{-1} and enhanced temporal resolution of 0.09 s/spectrum. The FTIR is equipped with two single element detectors, InSb with spectral response of 1800 – 5000 cm^{-1}, and HgCdTe with response of 600 – 2500 cm^{-1}. The field of view (FOV) was 45 mrad which covers a 6.39 cm diameter at the target distance of 1.42 m.

Results and Discussions

Imagery

A visible photograph of a PMMA sample after irradiation at 21.7 W/cm^2 for 70 s is provided in Figure 15. The laser beam covers most of the sample, and re-solidification of a melt layer can be observed in a small region, 3.36 – 4.12 mm from the sample edge. Similar observations of re-solidified of molten material have been reported around the edge of irradiated PMMA targets [57, 58]. In the central region of 15 mm, bubbles are generated as sub-surface vapor is formed. The carbon-black pigmentation in PMMA allows for absorption of the Nd:YAG beam into some depth of the sample. The absorptivity at 1.06 μm is considerably less, $\alpha \cong 4.5\ cm^{-1}$, than for the 10.6 μm CO_2 laser, $\alpha \cong 100\ cm^{-1}$, depending on the concentration of carbon, see Table 5. This in-depth absorption can lead to subsurface boiling. The size of the bubbles decreases at longer laser wavelength and higher irradiance [62]. From Figure 15, the bubbles are approximately less than 0.02 mm in diameter. The damaged zone on the post-irradiated PMMA exhibit well defined sharp edges, confirming that there is a threshold fluence for generating bubbles only in the center of the beam [62].

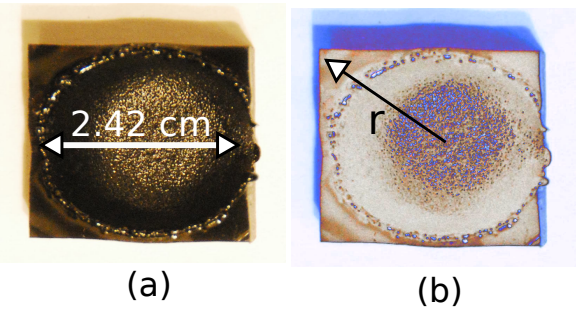

Figure 15. Picture of post-irradiated PMMA (a) original and (b) with contrast filter.

Broadband MWIR imagery of the optically thin, smoky plume can be obtained from the IFTS by averaging many modulated frames, yielding the DC component of the interferogram shown in Figure 16. For radiative fluxes between 4 – 22 W/cm^2, the observed infrared emission in our work was for pre-combustion plumes. At 21.7 W/cm^2, the intensity and spatial extent of the plume decreased significantly as the irradiation time increased from 9 to 57 s. The production of volatile decomposition products declines as surface reactivity degraded, followed by in-depth boiling and bubble formation. The plumes are unstable with significant turbulence, as illustrated in the high framing rate images of Figure 17. Plume turbulence can be investigated by looking at differences in intensities between images at two different frames. Figure 17 illustrates the difference between two OPDs of $\Delta t = 0.005$ s, the swirling turbulent eddies are evident as oval-like regions in the difference image. Subsequent difference images revealed the temporal evolution of these eddies as they break up while traveling down the turbulent plume. A small portion of variation in intensity is due to the change in interference pattern, which accompanies a change in the OPD. The 16-bit FPA saturates at 65,000 counts, with a 0.3

optical density neutral density filter, the average signal at center burst is 16,000 counts or 25 % below saturation limit. The interferograms appeared noisy as a result of stochastic intensity fluctuations caused by turbulence in the plume. Temporal averaging substantially reduced the noise in the interferogram [12, 13].

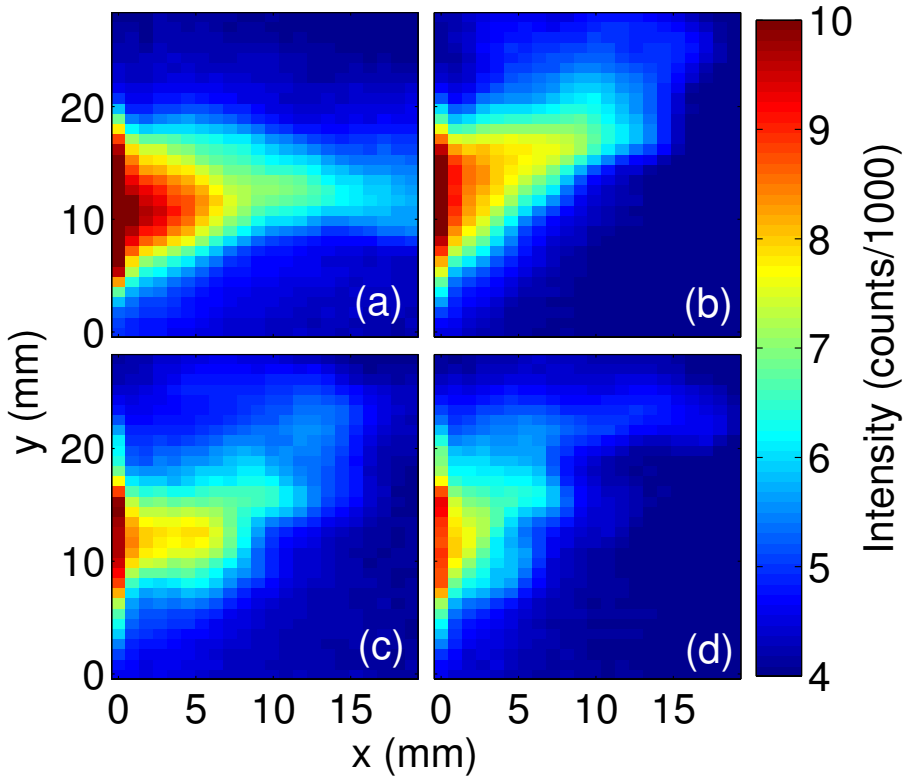

Figure 16. Infrared plume imagery of irradiated PMMA at 21.7 W/cm^2 at time intervals of (a) 9 s (b) 18 s (c) 37 s and (d) 57 s.

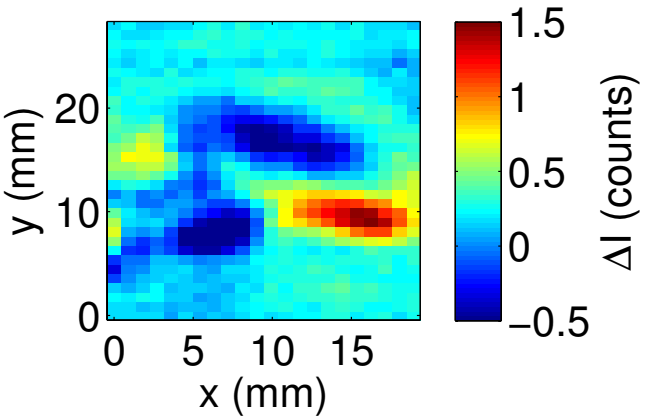

Figure 17. Difference between two frames ($\Delta t = 0.005$ s) at $t \cong 9$ s for 21.7 W/cm^2 reveal the turbulent eddies and their effect on the DC component of the interferogram.

The plume images for several irradiance levels after 24 s are illustrated in Figures 18(a-d). The plexiglass surface is located in the first, left high side column of each image. For I = 17.4 W/cm^2 surface outgasing begins at 8 s, but bubble formation does not occur until after 31 s. Minimal vaporization occurs for a delivered fluence of 208 J/cm^2. At 418 J/cm^2, a bright plume extends 10 mm from the surface and lofts to 13 mm from the center of the beam. The plumes are more similar when compared for similar delivered fluences (418 J/cm^2), as seen in Figures 18(e-f). However for the lower irradiances of 4 – 8 W/cm^2, the plume appears weaker at longer irradiation times in Figures 18(g-h).

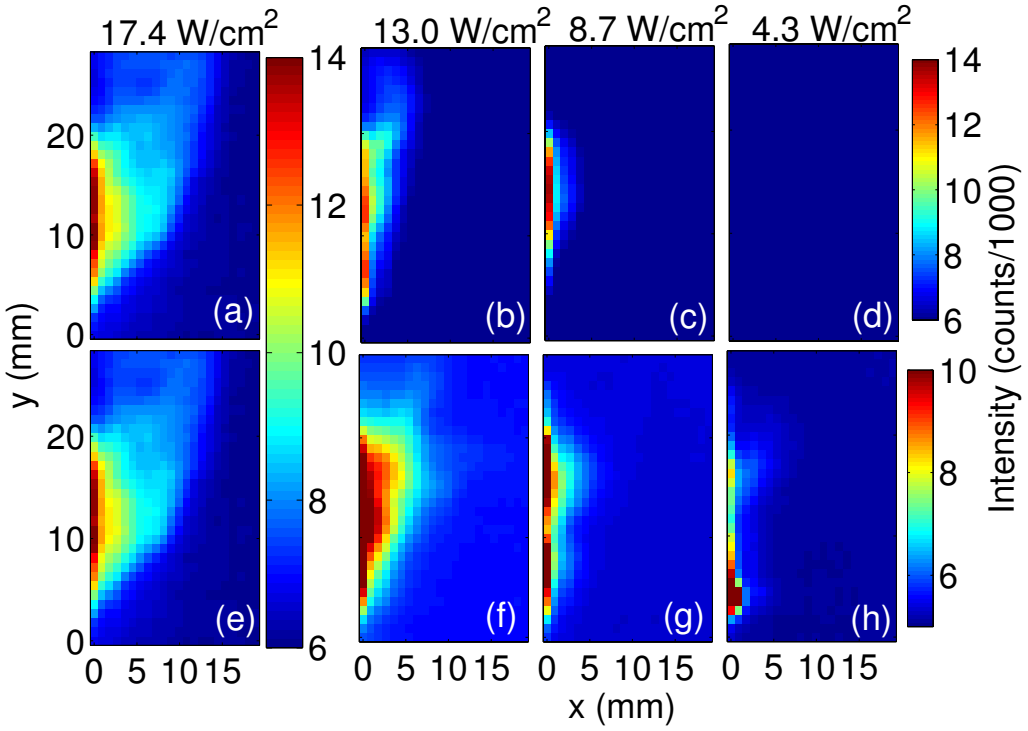

Figure 18. Infrared plume imagery of surface irradiated PMMA at t = 24 s for (a) 17.4 W/cm^2 (b) 13.0 W/cm^2 (c) 8.7 W/cm^2 and (d) 4.3 W/cm^2. Plume imagery at different time intervals of (e) 24 s (17.4 W/cm^2), (f) 32 s (13.0 W/cm^2), (g) 131 s (8.7 W/cm^2) and (h) 214 s (4.3 W/cm^2).

Spectral Features

The temporally averaged, non-imaged, long- and MWIR spectra of the plume at 0.6 cm^{-1} resolution are shown in Fig. 19. From Fig. 19a, the spectral ringing along most of the spectrum occurs as a consequence of the infinite interferogram length, which can be attenuated by the apodization function [100]. The observed spectral features are characteristic for the emission of MMA [113]. As sumarized in Table 4, we can identify

in the LWIR, combination of C-H and C-O-C deformation at 811 cm^{-1}, out of plane bending peaks for =CH at 938 and 1015 cm^{-1}, C-O stretching at 1159 and 1202 cm^{-1}, CH_3- bending peaks at 1308 and 1446 cm^{-1}, a C=C stretching peak at ~ 1632 cm-1, a C=O stretching peak at ~ 1737 cm^{-1}, and atmospheric H_2O absorption overlapping with the C=C and C=O stretching peaks from ~ 1330 to 1800 cm^{-1}. Similar spectral bands for the emission of MMA has been reported elsewhere from thermally decomposed PMMA [112, 117, 118]. The LWIR bands are analyzed semi-quantitatively in an effort to investigate the presence of other molecular species in the plume. The small gaseous species that are typically associated with the thermal decomposition of monomer MMA in air are: methanol, methane, propylene, 2-methyl propylene, acetone, formaldehyde, and methyl pyruvate [70]. The molecular structure of PMMA is shown in Fig. 20.

The =CH stretching band between 2800 – 3200 cm^{-1} is the most dominant spectral feature in the MWIR. Atmospheric H_2O and CO_2 absorption features are also evident in Fig. 19b. Based on the spectra, MMA was the primary decomposition product for the thermally decomposed PMMA at the laser irradiances between 4 to 22 W/cm^2.

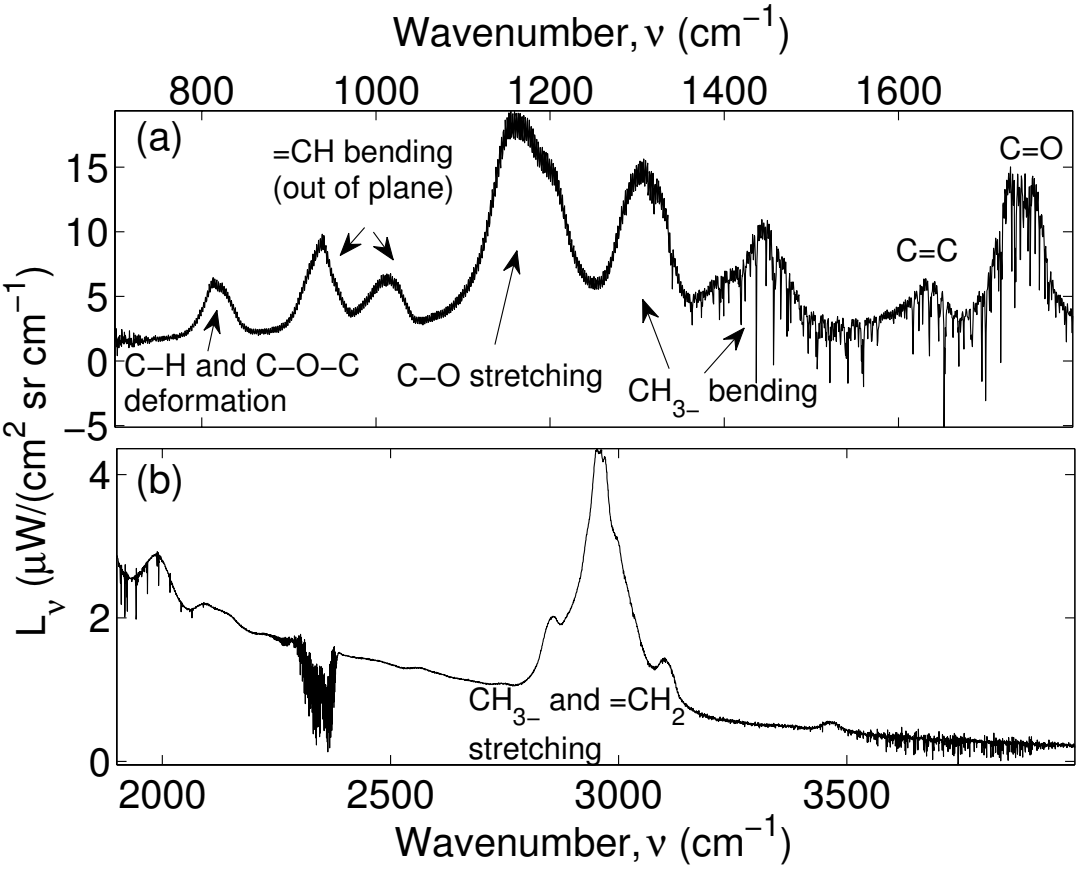

Figure 19. Non-imaging FTIR time averaged spectra for laser irradiated PMMA at 21.7 W/cm^2 showing the spectral radiance (L_ν) of MMA in the (a) LWIR and (b) MWIR.

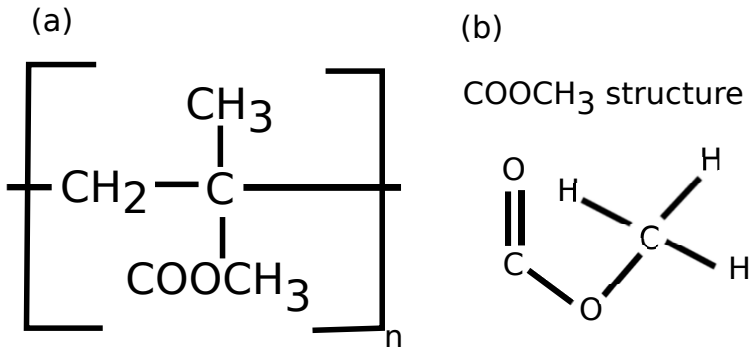

Figure 20. (a) Molecular structure of PMMA. (b) Structure of the $COOCH_3$ moiety

The temporal dependence of the non-imaged FTIR spectra of Figure 19a is summarized in Figure 21. The band integrated radiance, L, is defined by Equation (22). The temporal evolution of L for selected infrared bands is shown in Figure 21a. The C-H and C-O-C combination bands at 811 cm^{-1} and the =CH bands at 938 and 1015 cm-1, quickly reached steady values with no spectral variations in the first 12 s. However the band integrated radiance for the C-O stretching at 1159 and 1202 cm^{-1} have considerable upward curvature. By plotting the other bands as a function of the 811 cm^{-1} integrated radiance in Figure 21b, the C-O stretching at 1159 and 1202 cm^{-1} seem to have an additional kinetic influence as oppose to the other features which are linear. When comparing the fits of exponential and linear models for the C-O stretching band, the adjusted R-squared are 0.95 and 0.88 for the exponential and linear functions respectively. Therefore the linear bands reflect the same emitter, whereas a nonlinear feature possibly reflects another small hydrocarbon gaseous specie contributing to the signal as a result from the decomposition of MMA.

$$L = \int_{\nu}^{\nu+\Delta\nu} L_{\nu}(\nu)d\nu \tag{22}$$

Although MMA is the dominant product of thermally decomposed PMMA, methyl pyruvate has been reported as a major volatile decomposition product [70, 117]. At temperatures between 323 to 398 K, Martin et al. [119] reported the presence of methyl pyruvate as a product of thermally decomposed PMMA in air. However the concentration of this volatile fuel is very small, typically reported on the order of 0.06 wt % [119]. The fundamental infrared bands for methyl pyruvate has been reported

elsewhere [120]. The fundamental C-O stretching (ν_{12}) and OCH_3 rocking (ν_{11}) bands for the two fundamental isomers of methyl pyruvate overlap with the MMA emission bands at ~ 1159 and 1202 cm^{-1}.

The ν_{12} and ν_{11} bands of methyl pyruvate appears as narrower peaks in the reported infrared spectra of Wilmshurst and Horwood [120]. It may be possible that a small contribution of these two bands when overlapped with the MMA C-O band will give rise to a wider spectral band. In previous experiments with fiberglass polymeric materials, it was noticed that the CO ro-vibrational band from the pre-combustion plume appeared asymmetric, most likely due to a minor contribution of the -C ≡ C- stretching band overlapping with the CO P- branch [25]. Without a spectral infrared database of methyl pyruvate to model the data, the observations appear consistent with previous reports on methyl pyruvate as a decomposition product from thermally decomposed PMMA in air at comparable temperatures [65, 119].

The absorption coefficient for the MMA =CH stretch has been experimentally measured at 300 – 1000 K at atmospheric pressure [121]. Using the semi-quantitative technique developed in reference [122] where the experimental absorption coefficient is adjusted with empirical parameters, the database has been extended to 1400 K and interpolated in 50 K increments. A sample of this database is provided in Figure 22. The infrared absorption coefficient of MMA, κ was obtained from Prof. Greg Jackson at the University of Maryland. Fundamentally, the absorption coefficient, κ defined by Equation (23) is the product of line intensity, S, line shape, $g(\nu-\nu_o)$, and the number of

absorbing molecules per unit volume and pressure, N_L (Loschmidt's number = 2.447 x 10^{19} molec/cm^3/kPa at 296 K) [123].

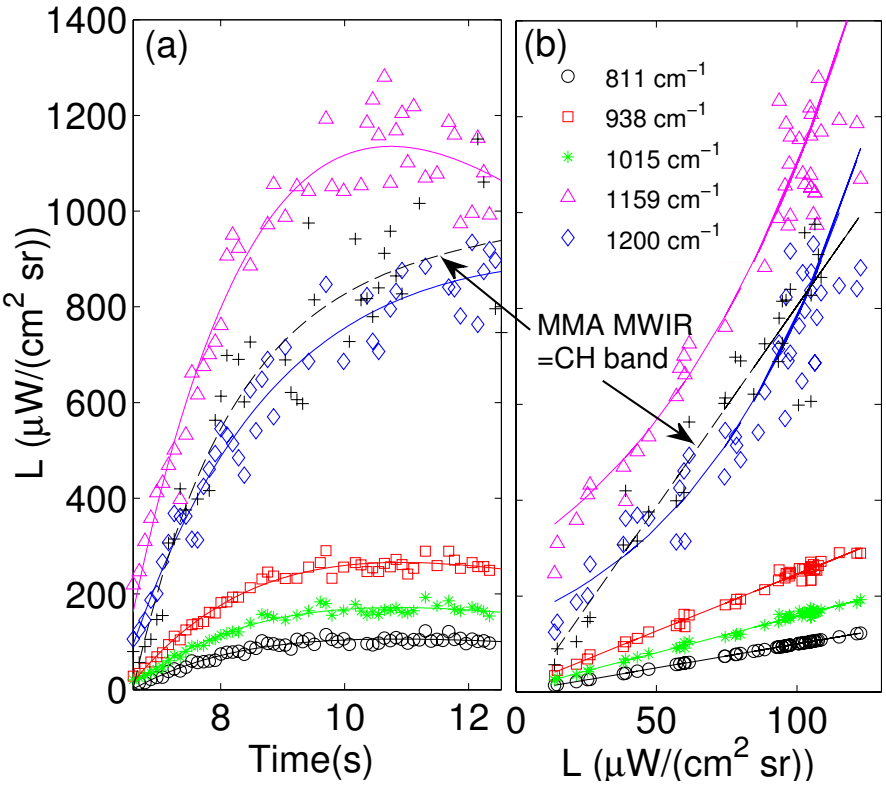

Figure 21. (a) Temporal variations of the band integrated radiance, L of selected infrared bands in the LWIR. (b) Band integrated radiance, L, of =CH and C-O bands plotted as a function of the irradiance for the 811 cm^{-1} band.

$$\kappa = Sg(\nu - \nu_0)N_L\left(\frac{296}{T}\right) \tag{23}$$

The absorption coefficient, κ, is related to the predicated radiance by:

$$L(\nu') = \int \varepsilon_{MMA}(\nu') \cdot B(\nu', T) \cdot ILS(\nu - \nu')d\nu' \tag{24}$$

$$\varepsilon(\nu) = 1 - \exp\left(-\xi \cdot \kappa(\nu, T) \cdot P \cdot l\right)\tau_p \tag{25}$$

where,

ξ = Volume mixing fraction of MMA

l = Plume path length (cm)

P = Pressure (Pa)

κ = Absorption coefficient of MMA (cm^{-1} Pa^{-1})

τ_p = Particulate transmittance

This radiative transfer model assumes a single layer, homogeneous plume in local thermodynamic equilibrium. The apparent spectral radiance, L_v, is defined by Equation (24), where ILS, is the instrument line shape, B is the Planck's distribution for blackbody radiation at temperature T, and ε is the monomer spectral emissivity as defined by Equation (25). The ILS function is determined by the interferogram length, $a = 0.3\ cm$, and a Hanning apodization function [100]. From the molar form of the ideal gas law, the gas pressure is defined as $P = \rho\, T\, (R/M)$, where ρ is the density of MMA (0.94 g/mol), R is the universal gas constant, and M is the molar mass of MMA (100.12 g/mol). The plume path length, l was assumed to be homogeneous and taken as the laser beam diameter of ~ 2.42 cm. The particulate transmittance is assumed independent of frequency, as described in recent fiberglass study [25].

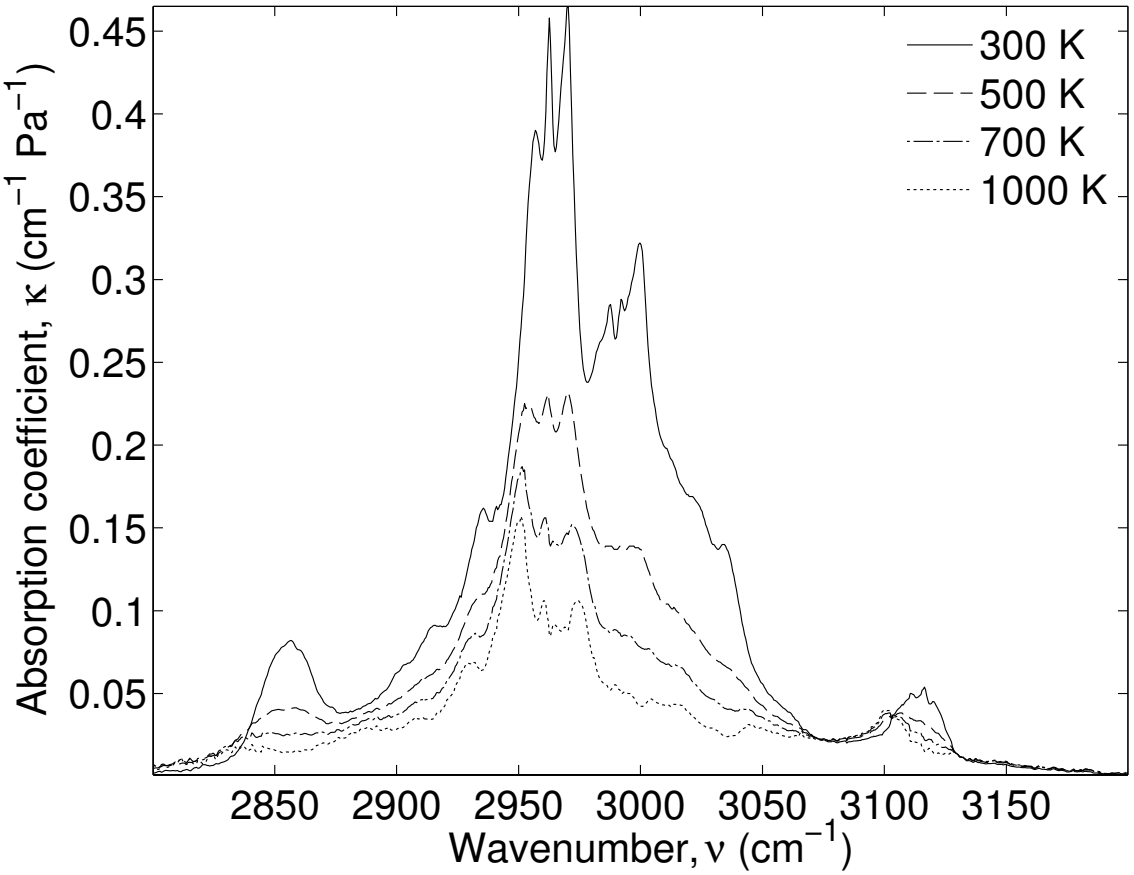

Figure 22. Temperature dependent absorption coefficient of MMA, κ, at 300 (–), 500 (--), 700 (·–) and 1000 (··) K for the CH_3- and $=CH_2$ stretching band in the MWIR [56].

The spectral radiance near 3.4 μm from the IFTS instrument for a pixel just above the surface in the center of the beam is provided in Figure 23. A fit of Equation (24) using the database of Figure 22 and the corresponding residual is also provided. The residuals are a small fraction of the observed radiance with a root mean square error (RMSE) of less than 0.2272 μW/(cm^2 sr cm^{-1}). The imaginary component of the FTIR provides an estimate of the noise level of the instrument. The RMSE for the imaginary

component is 0.1053 μW/(cm^2 sr cm^{-1}), somewhat lower than the fit error. The best estimates for the plume temperature and monomer column density from the nonlinear fit are 549 ± 1 K, and 2.77 ± 0.08 10^{16} molec/cm^2, respectively. The reported statistical uncertainties for all the results are defined as the half-width of the 95 % confidence interval and do not include systematic errors associated with the assumption of a homogeneous plume or the effects of turbulence. Further analysis of the gas plume to develop spatial maps and temporal evolution of the temperature and MMA concentration is present below (*plume dynamics section*).

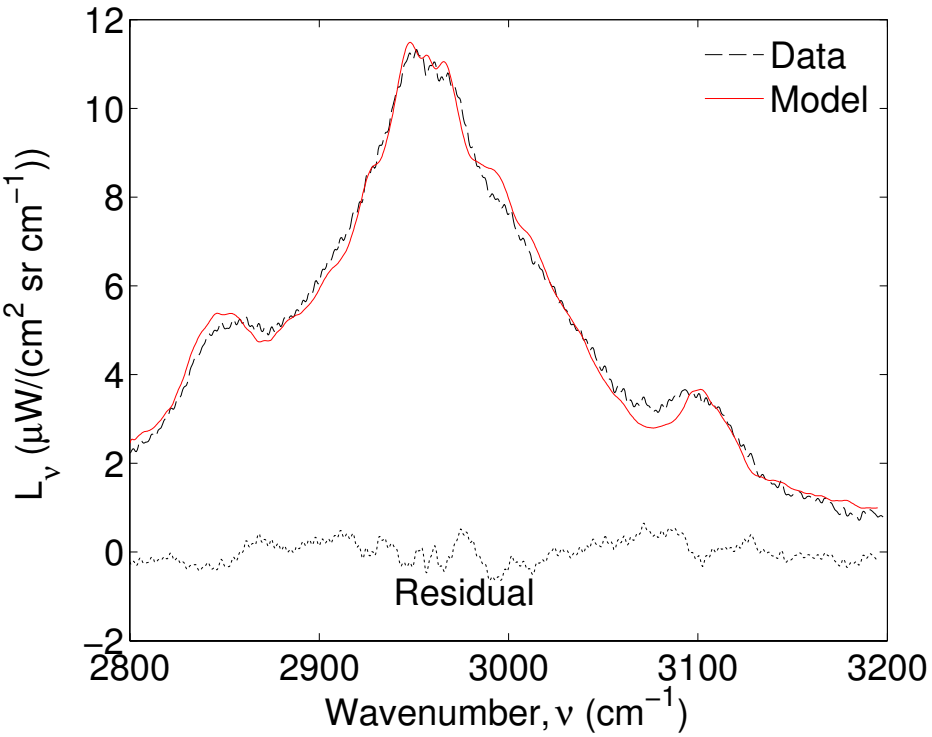

Figure 23. IFTS observed spectral radiance (--), fit (-) and residual (··) of the MMA 3.4 μm band at (x,y) = (0 mm, 11.7 mm).

Surface Temperature

The sample surface temperatures were investigated with the IFTS by rotating the sample at 30° angle relative to the incident laser beam as shown in Figure 14b. The spectral emissivity of the plume is low relative to the surface emission. From the non-imaging FTIR the monomer =CH emission is 18 % of the surface spectral radiance, as seen from Figure 24. For surface temperature estimation, the spectral region between 1900 - 2500 cm^{-1} was investigated to avoid any temperature contribution from the hot gas plume. The surface temperature studies were performed at 16 cm^{-1} spectral resolution to increase the temporal sampling to 855 Hz. A typical surface spectrum near the center of the irradiated spot for I = 21.7 W/cm^2, is shown in Figure 25a. A fit of Equation (24) with the emissivity defined by the gray body surface rather than the MMA, is also shown in the figure, yielding a surface temperature of 613.9 ± 0.8 K. The surface emissivity was assumed for black PMMA to be 0.96 [115, 124], also note the atmospheric CO_2 concentration required (257 ± 21 ppm).

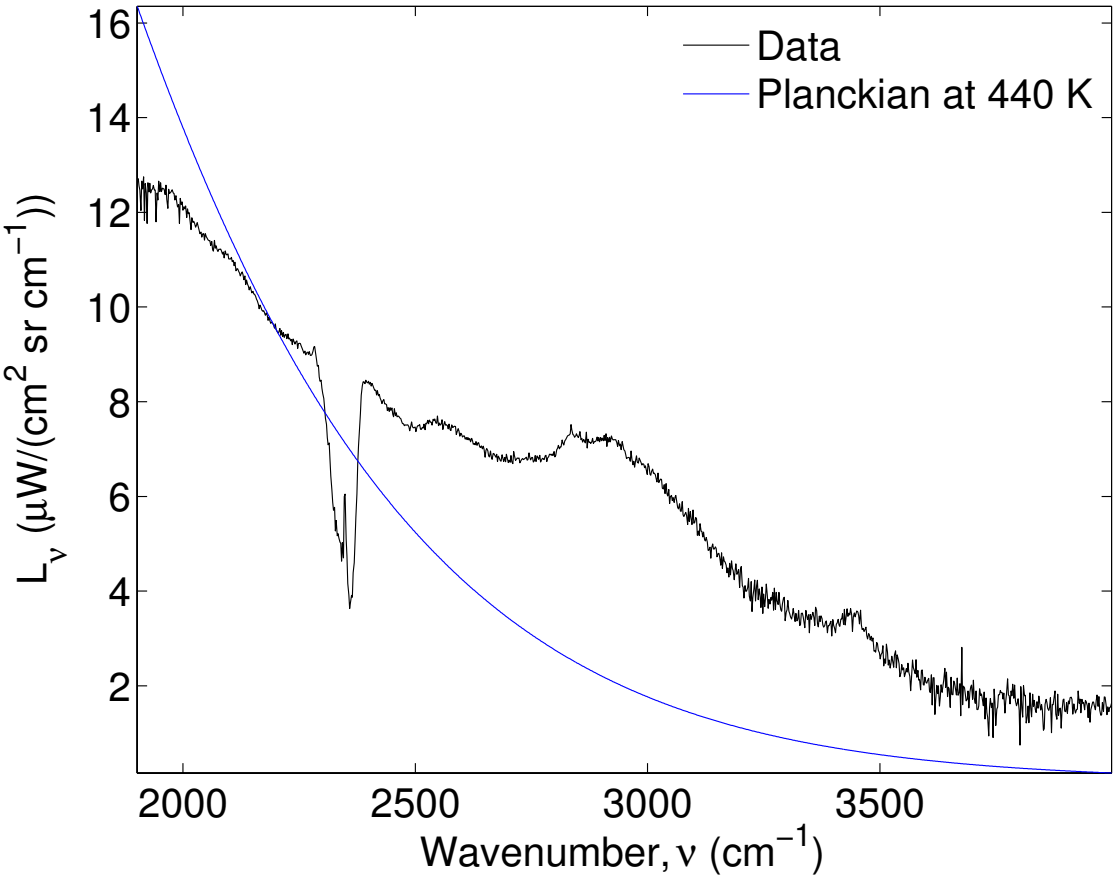

Figure 24. Non-imaged FTIR surface and plume spectral radiance at t = 51 s for the rotated 30° PMMA sample with a Planckian black body distribution at 440 K. The atmospheric CO_2 absorption feature appears near 2400 cm^{-1}.

A spatial map of the temperature distribution is provided in Figure 25b. Each pixel views a surface spot of y = 0.9 mm and x = 1.8 mm, due to the angled surface. There is a slight asymmetry in the temperature distribution, with ΔT = 17 K between the left and right sides of the beam at x = 18 mm. The plume is hotter towards the right side at x > 14 mm. The statistical error bounds for the fit temperatures are 1.4 to 1.8 K. The

temperature map reflects the laser beam spot profile with a near flat top beam of diameter 2.42 cm.

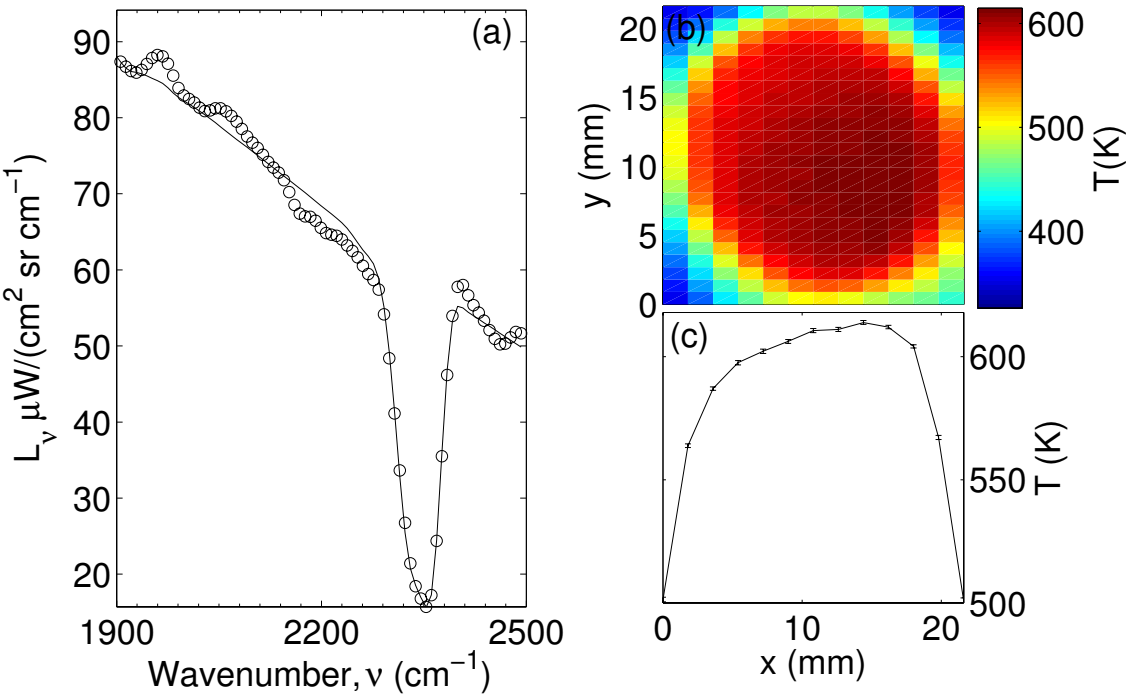

Figure 25. (a) Time averaged (t > 12 s) observed spectral radiance (O) from center pixel and spectral model (-), yielding an effective surface temperature of 613.9 ± 0.8 K. (b) Timed averaged spatial surface temperature distribution of irradiated PMMA at 21.7 W/cm^2. (c) Laser beam profile at y = 10 mm.

Figure 26 illustrates the surface temperatures evolving with an initial rise of about 20 K/s, and approach a steady state at about 600 K after 10 s, when irradiated at 21.7 W/cm^2. The temperature declines slightly over the next 60 s, probably due to surface emissivity changes. When the laser power is terminated, the temperature decays back

toward ambient with an initial decay rate of ~ 15 s. Laser heating balanced primarily by conduction suggests temperature dynamics described as:

$$c_p V \rho \frac{dT}{dt} = I(1-R)A - k\nabla TA \qquad (26)$$

where the heat capacity, c_p, density, ρ, and thermal conductivity, k, is assumed independent of temperature. Material properties are provided in Table 5. The reflectance is assumed to be R = 0.5 [57, 58], and the beam area is A = 4.5 cm^2. By assuming no conduction during the initial rapid heating, and an in-depth laser penetration length of $l = V/A = 1/\alpha$ = 0.25 cm, the initial temperature rise is calculated to be dT/dt = 28 K/s, only slightly higher than observed. A steady-state temperature rise from room temperature to 613 K would require a conduction time scale of 16 s, consistent with the observed final decay rate. However, to match this decay with lateral conduction time scale, $\tau_l = (\rho c_p l^2)/6k$, a diffusion distance of l = 2.9 mm, or about 23 % of the sample thickness is required. Lateral diffusion must be augmented by additional losses, possibly from the sample holder.

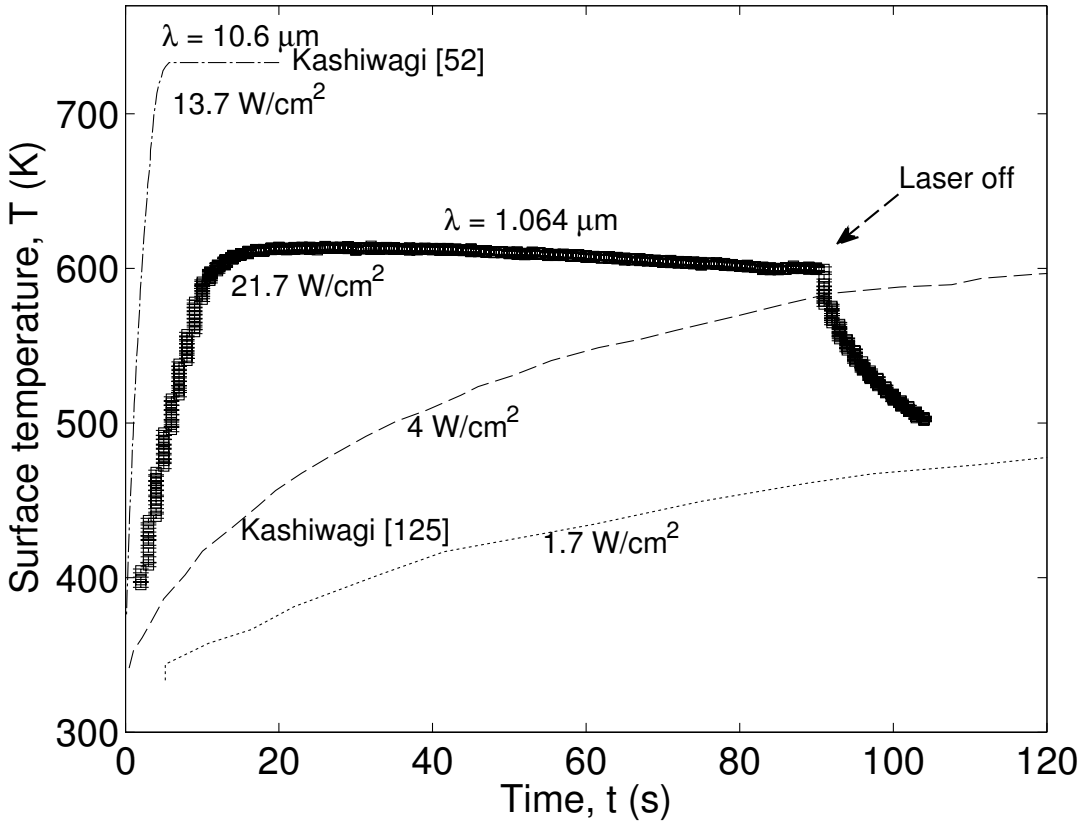

Figure 26. Temporal evolution of surface temperature irradiated with a 1.06 μm Nd:YAG laser at 21.7 W/cm^2 (□), compared against irradiated PMMA surfaces with a 10.6 μm CO_2 laser at 13.7 W/cm^2 (·-) from [52] and electrically heated at 4 W/cm^2 (--) and 1.7 W/cm^2 (··) from [125].

The surface temperature dynamics are compared with CO_2 laser and broadband MWIR radiant heating in Figure 26 [52, 125]. The rate of temperature rise at λ = 10.6 μm (CO_2 laser) is about three times greater despite the lower irradiance. The reflectance in the LWIR is less, $R \cong 0.05$ and the absorptivity is much higher, $\alpha \cong 100$ cm^{-1} [52, 56]. The stronger coupling and smaller in-depth heated volume is consistent with the higher heating rate. The prior results for broadband heating in the MWIR exhibit heating rates that are slow enough that a steady state condition is not achieved even after 100 s, and the initial heating rates are influenced by the conductive losses. The heating rates are influenced by the available oxygen in the gas boundary with lower surface steady state temperatures achieved at higher oxygen concentrations. The presence of higher oxygen concentration in the gas phase increases the mass flux. However, when surface reaction increases, the oxygen-mass flux effect is reduced due to the decrease of oxygen supply to the surface.

Plume Dynamics

The IFTS MWIR spectrum at each pixel has been analyzed as described in section 3.2 to obtain spatial maps for the temperature and MMA concentration in Figures 27-28. In the center of the plume, the signal-to-noise ratio is greater than 50:1. When the ratio drops to 2:1 at the edge of the plume, the fit results are not reported. At higher irradiances, the plume extends to 19 mm from the surface and the peak temperature is about 700 K. At lower irradiances, the plume size is reduced to 11 mm and peak temperatures are slightly higher, about 750 K. The slight upward curvature of the plume is due to buoyancy.

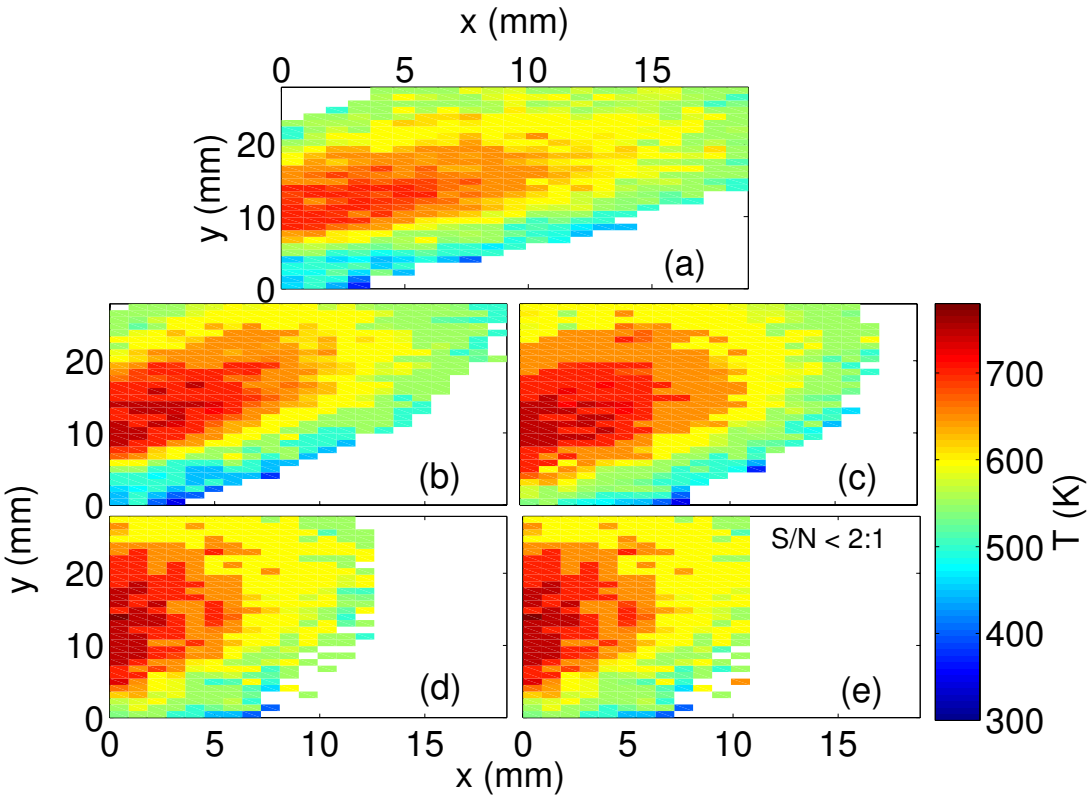

Figure 27. Time averaged spatial maps of gas-phase plume temperature for laser radiative fluxes of (a) 21.7 W/cm^2, (b) 17.4 W/cm^2, (c) 13.0 W/cm^2, (d) 8.7 W/cm^2 and (e) 4.3 W/cm^2.

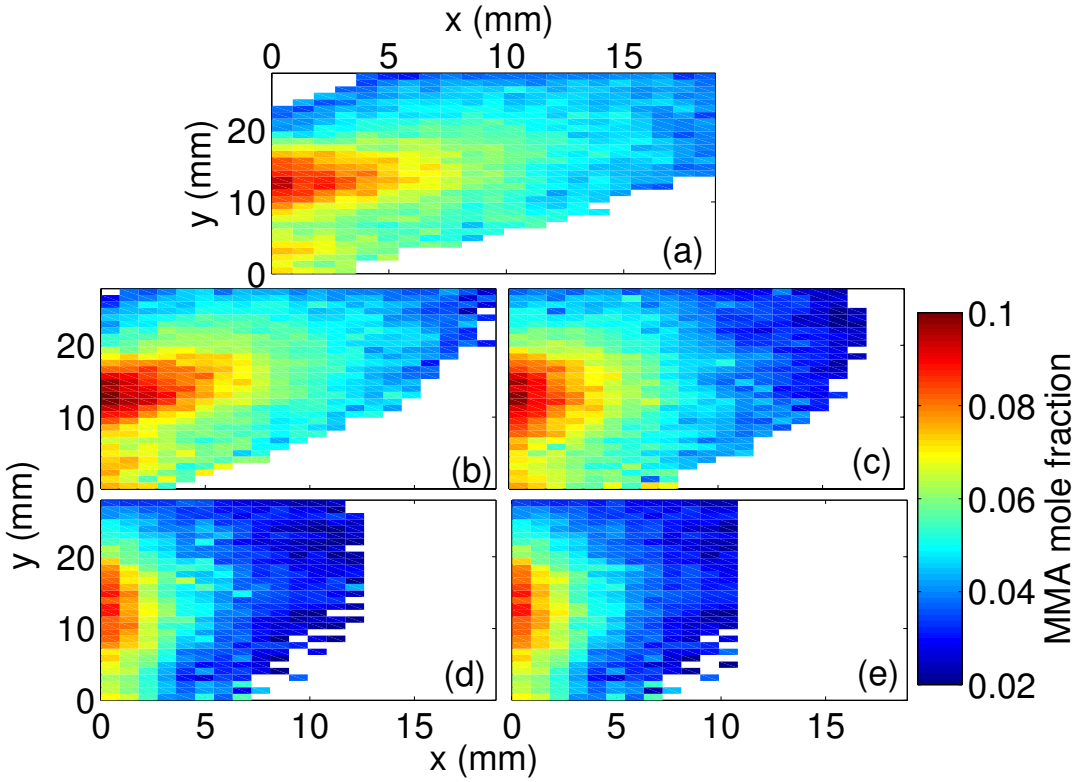

Figure 28. Time averaged spatial maps of MMA concentrations of the boundary-layer plume from laser irradiated PMMA at (a) 21.7 W/cm^2, (b) 17.4 W/cm^2, (c) 13.0 W/cm^2, (d) 8.7 W/cm^2 and (e) 4.3 W/cm^2.

The temporal evolution of the gas and surface temperatures are compared in Figure 29. The gas temperature is about 100 K higher than the surface and largely independent of time. This increase can be due primarily to plume absorption of the incident laser radiation. The plume temperature at the surface-boundary layer continues to rises above surface temperature steady value, consistent with Kashiwagi [52] observations. At the initial period when the surface is irradiated, convection of the hot

PMMA surface transfers energy, consequently heating the gas phase plume. This was observed by Kashiwagi [52] from simultaneous surface and plume temperature measurements with thermocouples. Gas temperature was lower than the surface at earlier times, rising above the steady surface temperature at later times with ΔT comparable to ours. With rising surface temperature, the rate of decomposition increases thus releasing more gaseous products into the boundary-layer. As the plume becomes thicker, absorption of laser radiation in the gas-phase causes the plume temperature to increase above the surface steady temperature. Previous experiments with fiberglass reinforced polymers showed similar trend, with steady gas-phase temperature being 1.6 times higher than equilibrium surface temperature prior to combustion [25]. Temperature fluctuations of ± 50 K arise from scene turbulence and interpolation of the MMA cross-section database. The MMA =CH emission band was first detected at 4 s when the surface temperature reached ~ 468 K. This surface temperature is in reasonable agreement with the reported temperature of polymer decomposition at ~ 493 K [64].

The MMA spatial concentration in Figure 28 is reported in mole fraction. The MMA concentration peaks at the surface for all irradiances and the extent of the plume is correlated with the temperature plots in Figure 27. However, the MMA concentration decays away from the surface faster than the temperature. Mutoh et al. [53] reported similar observations prior to combustion for CO_2 laser irradiated PMMA at 45 W/cm^2.

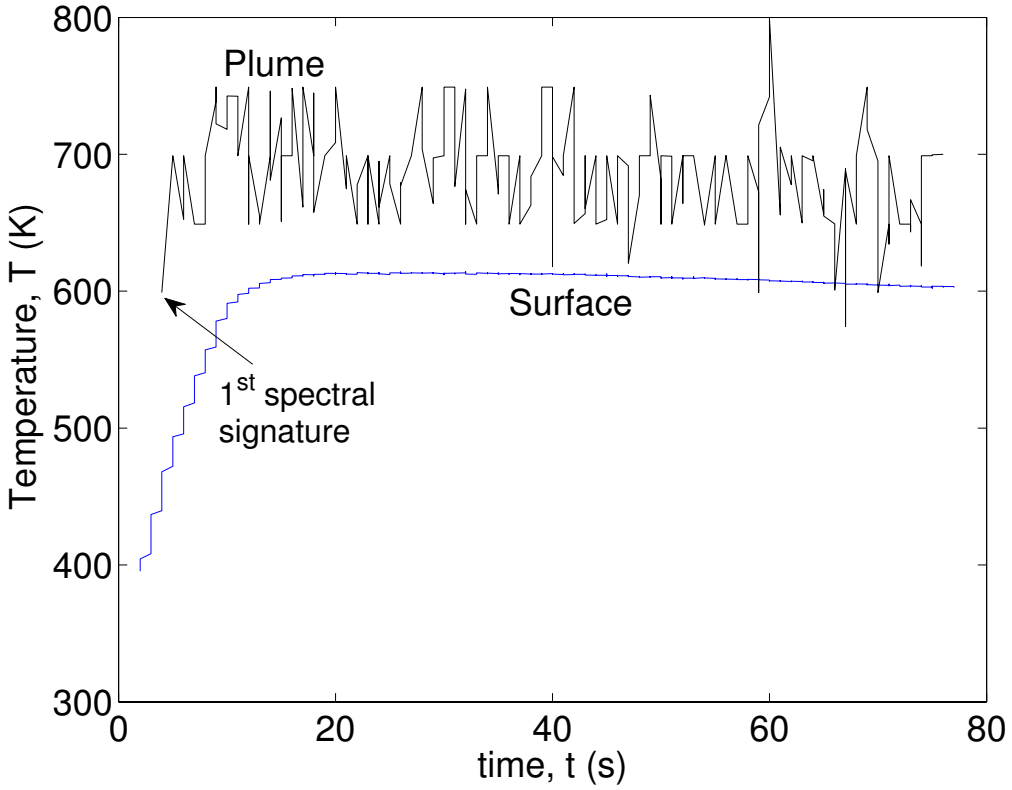

Figure 29. Temporal evolution of plume temperature at (x,y) = (0.9mm, 12.6 mm) and surface temperature at 21.7 W/cm^2.

Kinetics

To explore the gas phase kinetics in Fig. 30, the MMA column density is displayed as a function of time along the centerline of the plume spatial maps of Fig. 28 to investigate the decay rate. It is assumed that there exists an average gas velocity and temperature in the buoyancy-driven boundary layer. This assumption is not highly accurate, but is reasonable for an order of magnitude analysis by assuming the gas velocity is determined by buoyant flow as [52]:

$$v = \sqrt{gD} \cong 50 \text{ cm/s} \tag{27}$$

where g is the acceleration due to gravity and D is the laser beam diameter. As irradiance decreases the decay rates increases. At 21.7 W/cm^2, the decay rate is 21 s^{-1}, and at 17.4 W/cm^2 a 5 % increase occurs. For the lower irradiances from 13.0 to 4.3 W/cm^2, the rate increases, with values ranging from 40 – 55 s^{-1}, respectively. The spatially averaged MMA concentration at the surface increases by about a factor of two as the irradiance increases from 4.3 to 8.7 W/cm^2. This is consistent with an increase in vapor pressure at elevated surface temperatures.

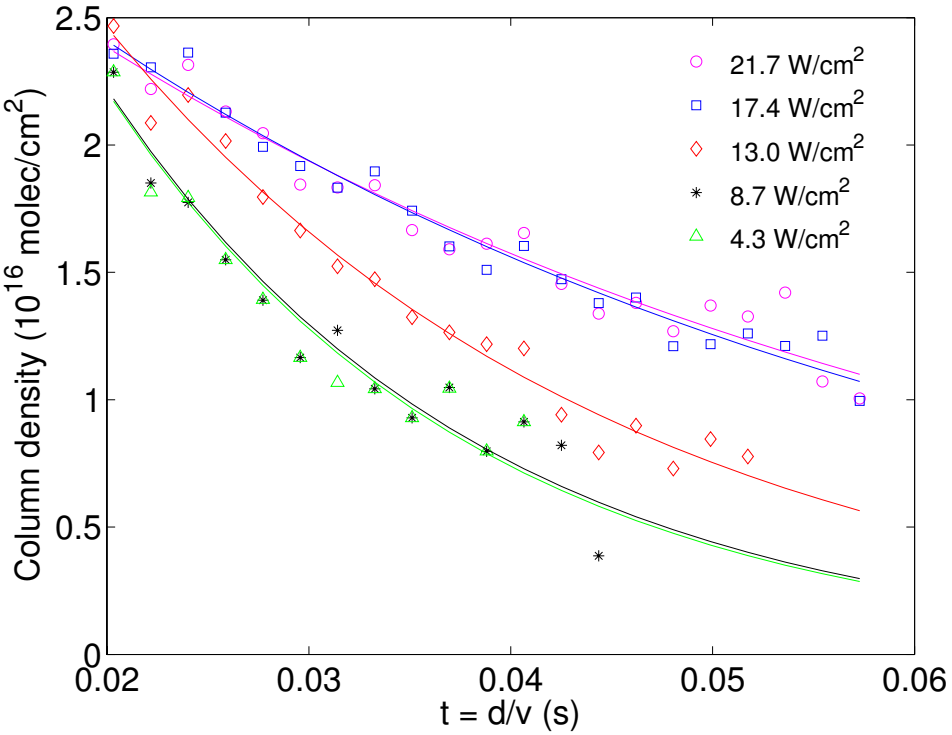

Figure 30. Time averaged MMA concentration along the center plume vector for irradiances between 21.7 - 4.3 W/cm^2. Time, *t*, is defined as the linear pixel dimension (distance) per the buoyant gas velocity of Equation (27).

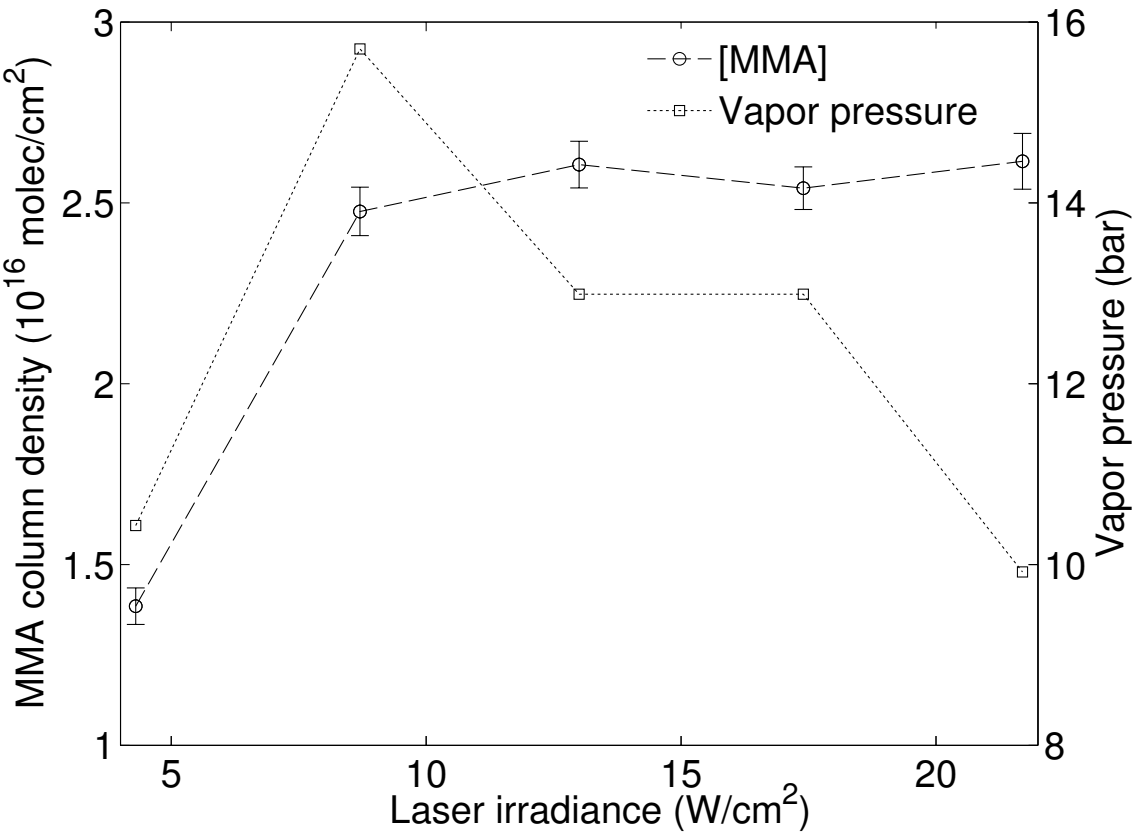

Figure 31. Spatially averaged MMA surface column density (O) and MMA vapor pressure (□) along the surface-boundary layer in the vertical direction (9 mm ≤ y ≤ 16.2 mm) for irradiances between 4.3 to 21.7 W/cm^2.

The MMA vapor pressure was calculated using Antoine equation as:

$$\ln(P) = A - \frac{B}{C + T_g} \tag{28}$$

where, T_g is the monomer gas temperature at the surface-boundary layer. The Antoine parameters for MMA between 312 – 362 K are defined as A = 5.37785, B = 1945.46, and C = -7.569, which were obtained from the NIST chemistry web book [126]. Figure 31

shows the calculated MMA vapor pressure using the monomer gas temperature, T_g at the surface-boundary layer. The rate of removal of the surface layer is reduced at lower irradiances. As power density increases from 8.7 to 21.7 W/cm^2, the MMA vapor pressure decreases due to an increase in surface layer degradation. A boiling process occurs at the PMMA in-depth that traps the vapor gas, thus making the MMA vapor not able to readily escape towards the gas phase boundary layer. At the higher irradiance of 21.7 W/cm^2, the plume intensity becomes weaker (Fig. 16). However, MMA molecules are able to escape more readily from PMMA at the lower irradiances since the rate of surface layer removal is minimal. Monomer MMA has a normal boiling point of 373 K, thus giving rise to higher vapor pressure at near-surface temperature. It appears that at lower irradiances, surface temperature matches the boiling temperature, which could possibly nucleate very few bubbles at the surface [127]. Brown and Kashiwagi [127] decomposed PMMA with an electrical graphite heater in the presence of O_2. Where at the lower flux (1.7 W/cm^2) concentration of MMA was higher at the surface than at 3 W/cm^2. Additionally, in a N_2 atmosphere, the MMA concentration remained the same for both irradiances. They postulated that gas phase O_2 enhances the generation rate of MMA, thus resulting in higher concentrations. Thus, concluding that irradiated surfaces at 3 W/cm^2 contained considerably less monomer as result of more evaporation from the hot surface at higher temperatures by a higher incident flux.

Thermal decomposition of PMMA involves a depolymerization and desorption of MMA towards the evolved gas-phase plume. The mechanism for PMMA surface

degradation according to Chaiken et al. [128] occurs in three stages with: (a) monomer forming near the surface, (b) diffusion of monomer to the surface, and (c) desorption of the monomer from the surface. Zeroth and first-order kinetics have been considered for the thermal decomposition of PMMA, effective activation energies for the desorption of MMA have been reported between 29 - 84 kJ/mol [69, 128, 129]. Chaiken et al. [128] reported activation energies for: desorption (E_{ds}) of MMA from the polymer, chain propagation (E_p), chain depropagation (E_d), and diffusion of monomer (E_D) in the polymer with respective values of 46, 23, 89 and 145 kJ/mole.

Figure 31 is an Arrhenius plot for MMA formation at the surface for a single pixel at (x,y) = (0 mm, 12.6 mm). After the initial surface temperature rise, the production of volatile decomposition products declines as surface reactivity is degraded once the surface reaches steady surface-temperature. For thermally decomposed PMMA in air at temperatures between 323 - 398 K, Martin et al. [119] observed a leveling off the monomer concentration with a rapid decrease, somewhat similar to our results. The authors concluded that the leveling off in MMA concentration begins at the same time as the zeroth-order scission rate process becomes dominant. Assuming that the concentration of the burning polymer remains constant at the initial heating rate, a zeroth-order rate process for the evolution of gaseous MMA is expected to occur at the surface-boundary layer. The obtained effective activation energy of 30.83 ± 8.29 kJ/mol is low to suggest monomer formation by chain rupture as the rate-controlling mechanism. The results are rather consistent with surface desorption of the monomer. Therefore, vaporization and desorption kinetics describe the rate of production of MMA towards the

plume from the bulk surface at the 21.7 W/cm^2. The intercept obtained from the Arrhenius plot is A_0 = 4.93 x 10^2 s^{-1}, and is consistent with the reported rate for desorption of A_d = 5.8 x 10^2 s^{-1} [130].

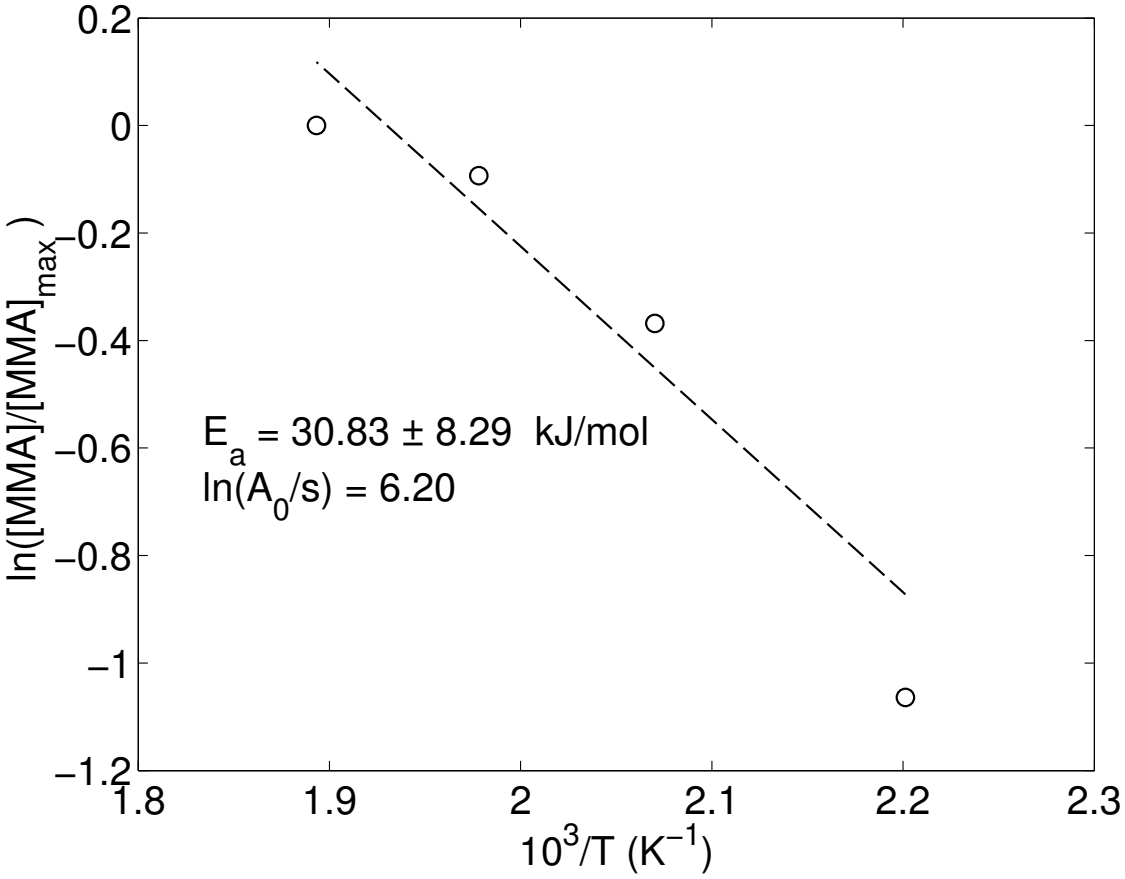

Figure 32. Arrhenius type plot of MMA formation for a single pixel at (x,y) = (0 mm, 12.6 mm) for irradiated PMMA surface at 21.7 W/cm^2.

Effective activation energies were computed away from the surface toward the plume into the gas boundary layer by implementing the same analysis of Fig. 31. By

using the plume temperature instead of the surface temperature, effective activation energies of 288 ± 47 kJ/mol to 390 ± 82 kJ/mol were obtained for individual pixels in the center plume from x = 0.9 – 2.7 mm, respectively. These effective activation energies in the plume correspond to degradation initiated by random scission [67, 69]. According to Song et al. [65], methyl pyruvate is formed as a result of main chain scission. The temporal dependence of the non-imaged FTIR spectra (Figure 8) suggests formation of other small gaseous specie such as methyl pyruvate, due to an exponential growth of the C-O stretching (ν_{12}) and OCH_3 rocking (ν_{11}) bands. Kashiwagi et al. [131] proposed that methyl pyruvate can be eliminated by trapped oxygen in the polymer chain, which was observed experimentally by Song et al. [65].

Conclusions

The thermal degradation of laser-irradiated black PMMA in air with a 1.06 μm Nd:YAG laser was investigated quantitatively using imaging FTIR spectroscopy. The first known two-dimensional spatial maps of temperature and MMA column density were developed for gaseous boundary-layer plumes. Based on the characteristic FTIR spectra in the gas phase plume, the primary decomposition product was MMA. Also, from non-imaging FTIR we were able to identify stretching bands in the LWIR that are typically associated with MMA and methyl pyruvate. The database for radiative transfer modeling of complex hydrocarbon spectra is rather limited and insufficient for our spectral fitting. Based on our semi-quantitative observations it is most likely that methyl pyruvate was present, since a minor contribution of the ν_{12} and ν_{11} bands overlapping with the MMA C-O stretching peak could make it appear much wider.

Moreover, the use of a homogeneous single-plume radiative transfer model to extract concentrations and temperature provided an adequate approximation. Imaging-FTIR also proved to be an efficient tool for investigating surface temperature distributions both temporally and spatially with low statistical errors. The spatial temperature distribution allowed visualization of the laser footprint, which is important for laser lethality experiments. A simplified thermal analysis elucidated the influence of 10.6 μm and 1.06 μm laser wavelengths on surface heating. The initial heating rate is dominated by absorption of the incident laser radiation, which is followed by a conduction-dominated process when surface reaches a steady-state temperature. The simplified analysis allowed to explain Kashiwagi [52] results with a CO_2 laser, where he was able to reach autoignition temperatures at much lower irradiances. At the longer 10.6 μm wavelength non-scattered radiation is absorbed at a few micrometers from the surface layer (skin depth). Gas phase temperature was higher than surface temperature, thus indicating that once decomposition begins, heating of the plume is largely due to absorption of the incident laser radiation.

For the thermal decomposition of PMMA to MMA at the surface, an effective activation energy of 30.83 ± 8.29 kJ/mol was obtained for a pixel at surface temperatures from 455 K to 600 K. This low activation energy is rather consistent with surface desorption of the monomer. Therefore at the 21.7 W/cm^2 irradiance, vaporization and desorption kinetics describe the rate of production of MMA at the surface. At the gas boundary-layer, effective activation energies in the plume correspond to degradation

initiated by random scission [67, 69]. It is more likely that a few MMA molecules decompose to methyl pyruvate based on the non-imaged FTIR spectra.

This work demonstrates the ability of IFTS to extract activation energies at discrete positions in space, enabling the produce spatial maps of activation energies. The combustion kinetics of PMMA and carbon based materials will be explore in future work to validate empirical results with reactive fluid dynamics modeling.

V. Boundary Layer Combustion Kinetics of Laser Irradiated Porous Graphite from Imaging Fourier Transform Spectroscopy

Preface

The combustion plumes arising from laser-irradiated graphite targets were investigated experimentally from hyperspectral imaging Fourier transform spectroscopy (IFTS). Porous graphite targets were irradiated using a 1.07 μm, 20-kW ytterbium fiber laser at irradiances of 0.3 – 4 kW/cm^2. Emissive plumes from the oxidation of graphite in air were monitored using a mid-wave infrared imaging Fourier-transform spectrometer with spatial resolution of 0.52 mm^2 per pixel. Strong spectral emission of CO and CO_2 were observed in the infrared between 1900 – 2400 cm^{-1} with an instrument spectral resolution of 2 cm^{-1}. A homogeneous single-layer plume line-by-line radiative transfer model (LBLRTM) and two band models (EM2C and RADCAL) were developed to estimate spatial maps of temperature and column densities of CO and CO_2 with a temporal resolution of 0.47 s per hyperspectral data cube. At 0.8 kW/cm^2 surface temperatures reach 2500 K. At 0.72 mm from the surface, steady-state values of gas temperatures of 2500 – 2900 K and column densities of 4.56 and 5.66 x 10^{17} $molec/cm^2$ were obtained for CO and CO_2 respectively. The spectral model was used to compute the absorption cross-sections of CO and CO_2 using spectral line parameters from HITEMP, the high temperature extension of the HITRAN database. Also, we validated the use of statistical narrow-band models (EM2C and RADCAL) with experimental combustion data at temperatures as high as 2900 K. Systematic errors associated with the spectral models between LBLRTM, RADCAL and EM2C are discussed. Temporal variations in

plume temperature and column densities were investigated up to 3 mm away from the surface into the boundary layer. At 0.72 mm from the surface, experimental results indicated a dominant production of CO_2 at surface temperatures from 2157 - 2530 K, thus corresponding to the global heterogeneous reaction of CO and CO_2 production at the surface. On the basis of CO/CO_2 primary product ratio, we obtained effective activation energies of 149 to 111 kJ/mol at distances between 0.72 mm to 3 mm away from the surface in the gas-phase boundary layer, respectively. The effective activation energies were comparable near the surface (0.72 mm) with the global heterogeneous reaction for production of CO and CO_2 at the surface, whereas in the boundary layer (2.16 mm) the global homogeneous reaction of CO oxidation to CO_2 dominates. Kinetics interplay between heterogeneous and homogeneous combustion kinetics are shown from experimental observations at high spatial resolutions. Overall the boundary layer profile at steady-state is consistent with CO being mainly produced at the surface-boundary layer by heterogeneous reactions followed by a rapid homogeneous combustion in the boundary layer towards buoyancy.

Introduction

Novel experimental techniques with high spatial resolution of ≤ 1 mm for laser spot sizes of 1 - 10 cm are of growing interest, particularly to investigate the combustion plume from laser irradiated materials at high temperatures. Two-dimensional imaging of combustion plumes above laser-irradiated samples would be particularly useful in developing profiles for molecular species concentrations and gas temperatures at the boundary layer, benchmarking reactive fluid dynamic calculations. Recently, the use of

imaging Fourier transform spectroscopy (IFTS) was established to examine the evolving combustion gas plume generated by irradiating composite surfaces with high power lasers [25, 132]. Through analysis of the characteristic spectra of emissive plumes in the mid-wave infrared (MWIR), the CO and CO_2 kinetics can be analyzed both spatially (≤ 1 mm^2 per pixel) and temporally from hyperspectral IFTS. The combustion mechanism of a graphite target will be explored experimentally, where well-established kinetic models exist for carbon by comparing empirical observations with global kinetics models.

The combustion mechanism of graphite has been extensively investigated in an attempt to elucidate the fundamental mechanism of reaction. Carbon oxidation kinetics can be simplified using global reaction mechanism. At the surface, the heterogeneous reaction (29) occurs first [90-93], followed by the homogeneous reaction (30) in the gas phase [94-96].

$$\frac{\alpha+\beta}{\alpha/2+\beta}C_{(s)}+O_2 \rightarrow \frac{\alpha}{\alpha/2+\beta}CO+\frac{\beta}{\alpha/2+\beta}CO_2 \tag{29}$$

$$CO+1/2O_2 \rightarrow CO_2 \tag{30}$$

However, there has been a debate about reaction (29) as to whether CO and CO_2 are the primary products of the heterogeneous reaction. The general consensus has been that for temperatures greater than 1200 K, the CO_2 production is small [74] but at lower temperatures both CO and CO_2 are present [75, 76]. Moreover, Mitchell et al. [78] argue that at temperatures around 2000 K, it is necessary to consider the formation of CO_2 at

the surface to accurately account for the heat release rate, and hence, the mass burning rate, and surface temperature. However, Adomeit et al. [79] found that the heterogeneous reaction rate corresponded to a predominant production of CO_2, rather than CO, contrary to the results reported elsewhere [74-76]. The CO/CO_2 ratio has been shown to increase exponentially with increasing temperature and can be expressed in the Arrhenius form of Equation (31) [72, 133].

$$[CO]/[CO_2] = A\exp(-B/T) \tag{31}$$

where, A and E_a are the pre-exponential and effective activation energy obtained from experiments.

The primary product ratio of CO/CO_2 has been measured experimentally by many investigators and expressed empirically for the relative rates at which CO and CO_2 are produced with the Arrhenius relation of Equation (31). According to Arthur [74], the CO/CO_2 ratio increases with temperature and the effective activation energy, $E_a = E_{CO2}$-E_{CO}, where it is estimated from the slope of Equation (31) from the least squares method. The resulting effective activation energy, E_a, is for the production of CO and CO_2 from the heterogeneous reaction at a measured temperature range. From the empirical relationship of Arthur [74] given by $[CO]/[CO_2] = 2500 \exp(-6240/T)$, $[CO] = [CO_2]$ at T = 800 K, and at T = 1700 K, CO is 64 times higher than CO_2. Hayhurst and Parmar [73] investigated the oxidation of graphite up to 1400 K, where they found that CO was formed at the surface and later being converted to CO_2 in the gas phase. Chelliah et al.

[88] concluded that there is a strong coupling between the homogeneous and heterogeneous kinetics that depends on temperature, flow rate, oxidizer, and pressure. Therefore, the overall oxidation of graphite depends on both the heterogeneous and homogeneous kinetics rate. The kinetics interplay between homogeneous and heterogeneous reaction can be complicated due to secondary reactions, since CO can be oxidized to CO_2, and CO_2 can be reduced by the carbon surface to CO.

With laser irradiances as low as 45 W/cm^2, a significant combustion plume was produced on fiberglass targets in previous experiments [25, 132]. On the contrary, solid graphite requires a much higher irradiance of 181 W/cm^2 in order for a sizeable combustion plume to occur [71]. The evolved combustion plume from laser irradiated graphite between 0.2 – 4 kW/cm^2 is shown from high-speed infrared and visible imagery qualitatively in the *plume dynamics* section. The primary focus of this work was to investigate quantitatively the combustion mechanism of laser-irradiated graphite at 777 W/cm^2. The evolution of combustion gases in the plume was monitored from specie characteristic ro-vibrational spectra in the MWIR. Plume temperature and concentrations of CO and CO_2 are then estimated from various radiative transfer models. Theses spectral models include line-by-line database and narrow band-models. The estimation of front surface temperatures are complicated by the coupling of evolving surface emissivity and intervening gas plume emissivity. By monitoring the gas plume perpendicular to the surface, much of the information necessary for separating surface temperature from gas emission becomes available. Effective activation energies of porous graphite targets are then determined by Eq. (31) from empirical observations at

the boundary layer. Without detailed fluid dynamics modeling, the experimental results are then compared with established graphite combustion kinetics by considering global heterogeneous and homogeneous reaction mechanisms.

Experimental Methods

Porous graphite targets from Graphtek LLC, of 7.62 x 7.62 cm and 1.27 or 0.64 cm thickness were mounted vertically in a flat surface perpendicular to floor and irradiated in air by a 20 kW IPG Photonics model YLR-2000 ytterbium fiber laser at 1.07 μm, as shown in Figure 33. Pyrolitic graphite and porous samples with particle diameters of 0.6 and 0.15 cm were mounted vertically in air at atmospheric pressure. The sample holder was a vise clamp insulated with ceramic between sample and the steel serrated jaws, holding the sample at the bottom edge. Buoyancy and a distant fume hood drive a slow vertical (+y direction) flow of ~ 8 m/s. Gaussian beams with a one sigma radius of 2.23 cm and irradiances of 0.2 – 4 kW/cm^2 were incident on the graphite sample at normal incidence for 120 s.

The primary optical diagnostic is a MWIR (1800 – 6667 cm^{-1}) imaging Fourier-transform spectrometer viewing the gas plume evolving from the surface. The IFTS was placed at a focal distance of 47 cm from the center of the plume and observes hot gas emission integrated along the line of sight (z-axis) with two-dimensional image away from surface horizontally (x-axis) and along the surface vertically (y-axis). The InSb focal plane array (FPA) was narrowed to 200 x 64 pixels with a spatial resolution of $0.52mm^2$/pixel. Interferograms were recorded on each pixel with a spectral resolution of 2 cm^{-1}. The Fourier-transform of the interferograms produces full hyperspectral data

cubes with a temporal resolution of 0.47 s. The IFTS is calibrated using two wide area blackbodies at 673 and 873 K by dividing the spectrum by the gain and subtracted by the offset to convert the spectra in absolute units of radiance (W/cm^2 sr cm^{-1}) [116]. A large cold blackbody is placed on the far side of the plume to provide uniform background. The 16-bit FPA using a 0.3 optical density neutral density (ND) filter saturates with 65,000 counts at 300 $\mu W/(cm^2$ sr $cm^{-1})$, with a background radiance of 6 $\mu W/(cm^2$ sr $cm^{-1})$. For gas plume temperatures near 1000 K, the DC component of the interferogram represents 28 % of the dynamic range, with the interferometer producing an 8 % modulation at zero optical path difference (ZPD) [25]. For the typical conditions encountered in our work with a 2.0 ND filter, the plume radiance at 2900 K is 1000 $\mu W/(cm^2$ sr $cm^{-1})$ where the ratio of the DC component to center burst is 72 %.

A Phantom v7 three-color, CMOS visible camera with 1024 x 1024 pixels provides full frame imagery at 350 Hz. At a distance of 72 cm, the individual pixel field of view is 0.14 mm/pixel. The visible imagery provides information on flow field, including ejected particle sizes and velocities. Surface temperature was monitored with a FAR associates SpectroPyrometer with spatial averaging over the central 0.75 cm radius of the irradiated spot, or the central 33 % of the Gaussian beam diameter.

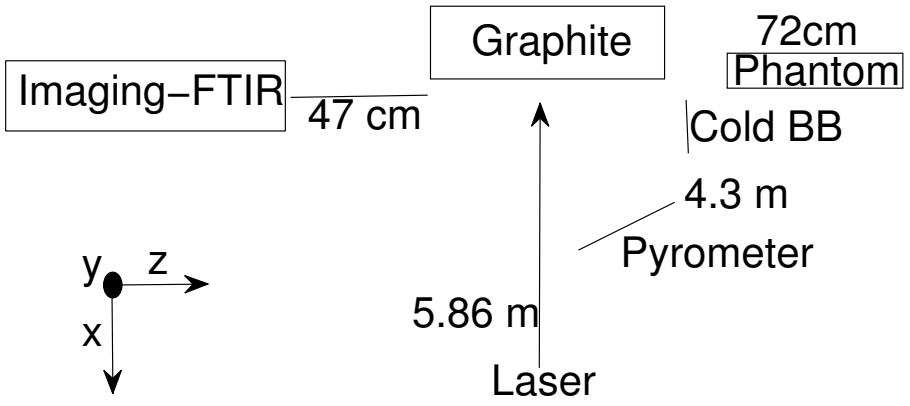

Figure 33. Schematic experimental set-up.

Results

Plume Dynamics

Broadband imagery without spectral resolution from both the mid infrared IFTS InSb array and the visible camera provide information about the structure and fluid dynamics of the combusting plumes. An interferogram cube from the IFTS is comprised of broadband imagery. The high-speed broadband infrared imagery (DC+AC) reveals plume dynamics such as turbulent motion. By averaging the temporal interferogram cubes for the entire laser on event, the noise associated with scene change artifacts are reduced [12, 109].

Images of the infrared emissive plumes at several irradiances levels for the coarser porosity samples for a single OPD are shown in Figure 34. A temporal average of 1.2 x 10^6 frames over 120 s produce steady images that define the spatial extent and structure of the combustion products. Blackbody emission from the hot 1.27 cm graphite sample

located in the bottom right corner of each images was masked to eliminate saturated pixels. The laser beam is centered on the sample at y = 33.12 mm and the Gaussian width extends from y = 10.08 – 54.72 mm. Combustion is weak at I = 251 W/cm^2, where the surface temperature is T_s = 1800 K and the heterogeneous oxidation is relatively slow. As the laser irradiance is increased from 485 W/cm^2 to 1 kW/cm^2 the surface temperature increases from 2200 K to 2900 K. Under these conditions, the spatial extent of the IR plume expands to 4 – 12 mm away from the surface (x-direction) and continues for ~ 4 cm above the sample. As the plume expands in the vertical, y-direction it conforms to the top edge of the graphite and rises primary due to buoyancy. The sample is sufficiently hot over the full extent to saturate the InSb array and heterogeneous reaction at the top edge contributes to the emission above y = 60 mm.

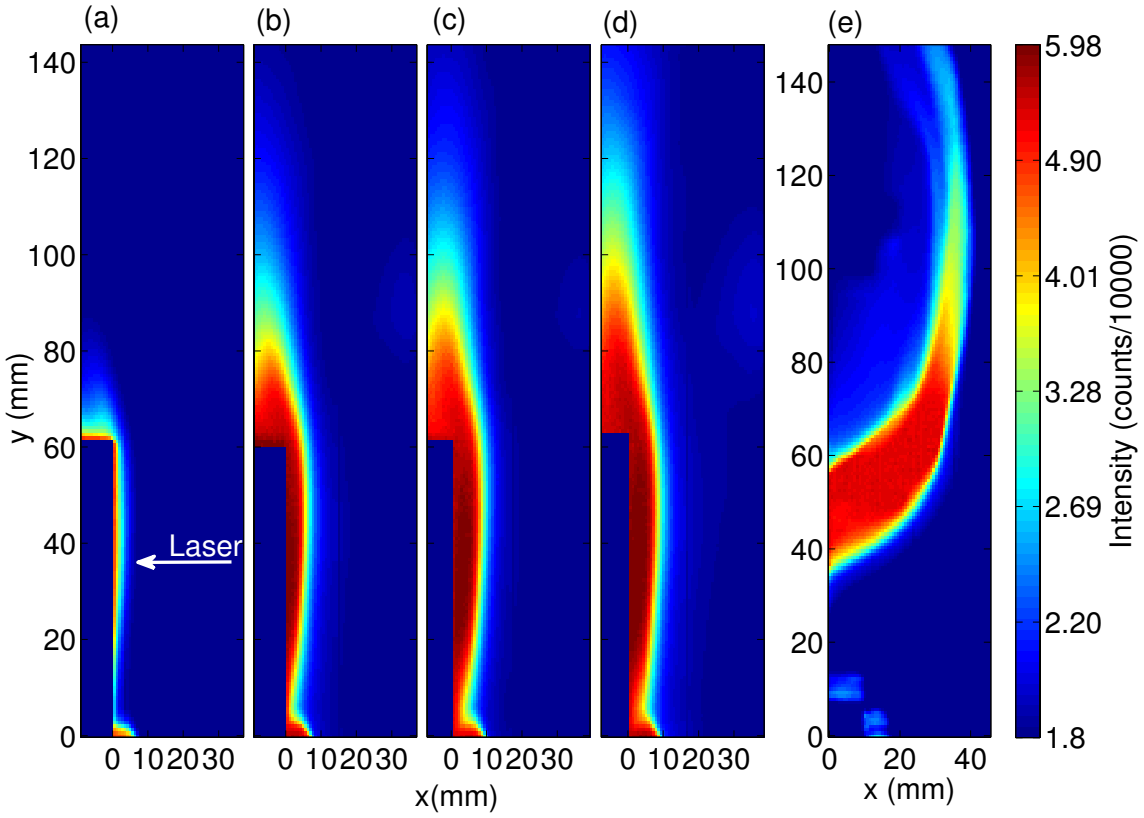

Figure 34. Time averaged infrared combustion plume imagery of laser irradiated porous graphite (0.6 cm particle size) at (a) 0.25 kW/cm^2, (b) 0.49 kW/cm^2, (c) 0.78 kW/cm^2, (d) 1 kW/cm^2 and (e) 4 kW/cm^2.

At 4 kW/cm^2 the plume changed radically due to a large flux of CO, CO_2 and carbon particulates emanating from the surface, as seen in Figure 34e. From optical pyrometry measurements, the surface temperature exceeded the carbon sublimation temperature of 4000 K [134-136]. The flux from the surface appears comparable or larger than the buoyant atmospheric flow and a jet extends to 4 cm from the surface and several beam diameters in the vertical direction. It is likely that surface sublimation of

carbon now dominates the plume dynamics. Indeed, after termination of the laser irradiation, a formation of deposited carbon fills an area of 6 mm^2 and extends into the plume to x = 19 mm, just above the jet at y = 60 mm, as seen from Figure 35. Structural and morphological changes have been reported for laser irradiated graphite samples, resulting in visible craters and irregular shapes near the irradiated surface [137]. After 10 s of irradiation, graphite has been removed from the sample to a depth of 3.18 mm across 27 % of the beam.

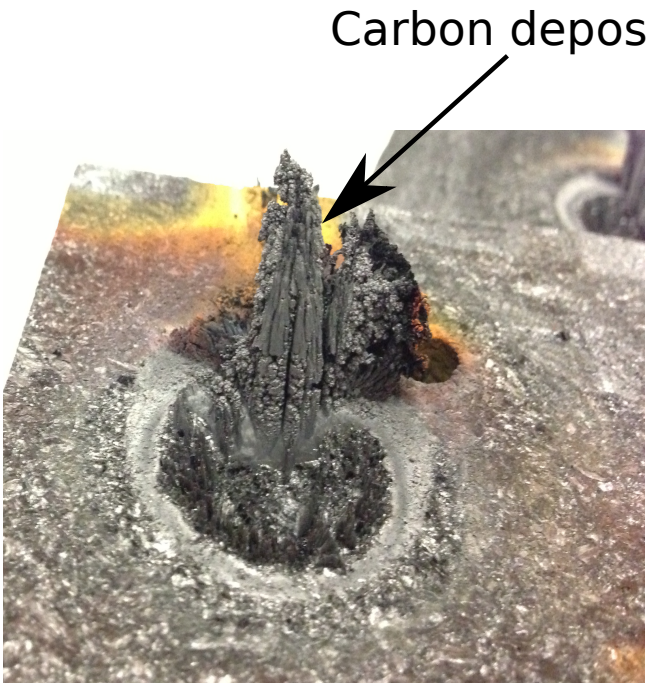

Figure 35. Post-irradiated porous graphite target at 4 kW/cm^2 showing structural changes with formation of deposited carbon.

The porosity of the graphite also affected the plume dynamics presumably due to the surface area available for oxidation, as shown in Figure 36. For the coarser graphite, 0.6 cm particle sizes, the plume is significantly thicker, longer and brighter. The extent of the plume for the pyrolitic graphite is similar to the less coarse material, but the intensity of the plume near the surface is significant higher.

The MWIR imagery is complemented by the high speed visible imagery sampled in Figure 37 and Figure 38. The plume first becomes evident in Figure 37a after about 16 s of irradiation at 0.8 kW/cm^2. The surface temperature at this point is 2290 K and the intensity in the MWIR is about 44 % of the steady value. The temporal evolution of the visible plume during the next 40 ms is illustrated in Figure 37. Bright emission is observed at the surface along most of the extent of the laser irradiated spot. A sudden expulsion of gaseous and particulate matter occurs near the center of the beam, growing in intensity and flowing vertically upward near the surface. The plume expands to 2.12 mm from the surface (x-direction) and 18 mm (y-direction) from the center of the sample to near top edge in 40 ms. Several particulates of diameter ~ 0.1 – 1.0 mm can be identified in the imagery. The initial plume velocity is of ~ 50 cm/s, and expands to 2.1 mm from the surface lasting 0.19 s. After this jet disappears, a very thin flame evolves from the surface and becomes steady at about 26.3 s after the beginning of laser irradiation.

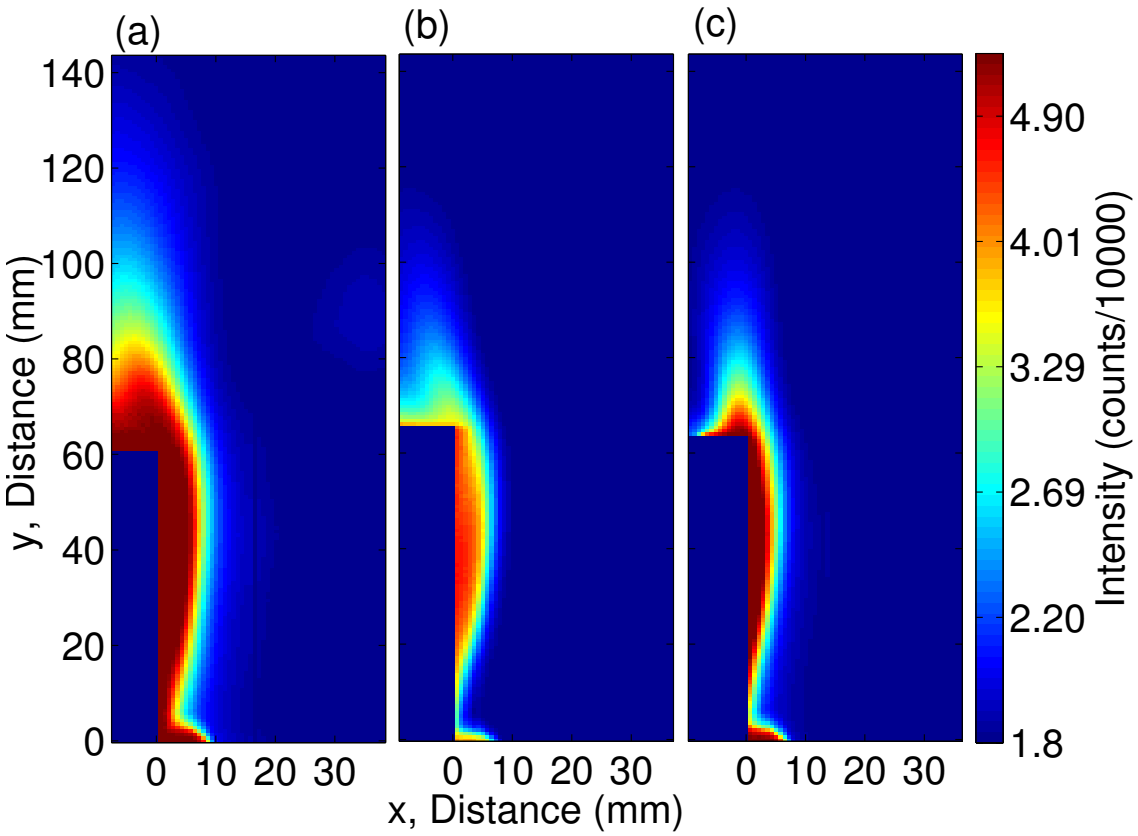

Figure 36. Time averaged infrared combustion plume imagery of laser irradiated porous graphite at 485 W/cm^2 with particle size of (a) 0.6 cm and (b) 0.4 cm. (c) Pyrolitic graphite.

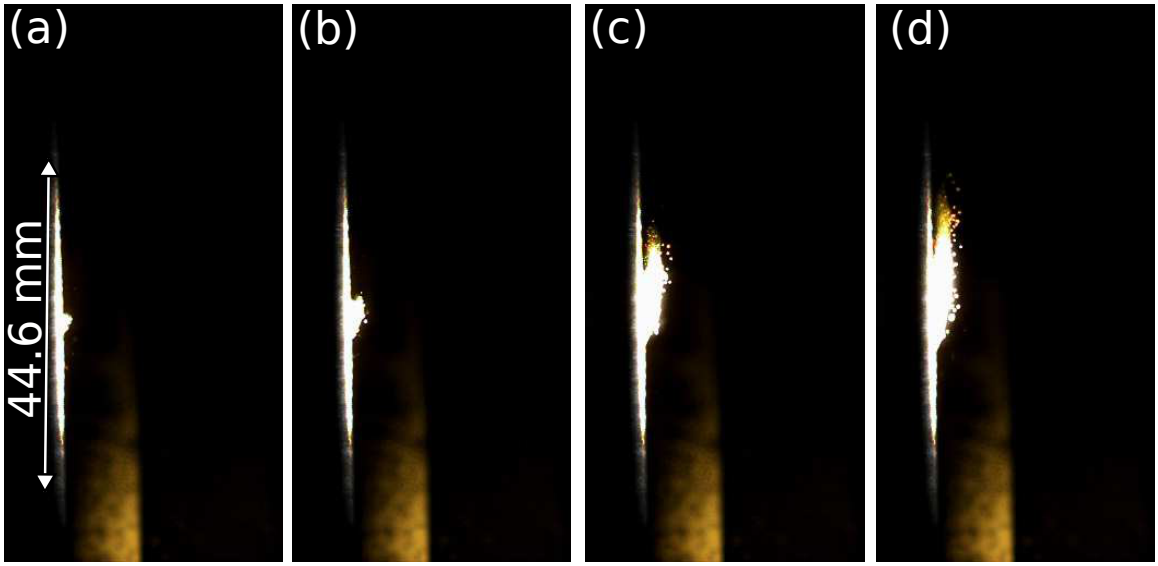

Figure 37. High-speed visible imagery for irradiated graphite at 777 W/cm^2 at single frames for time of (a) 16.28 s, (b) 16.29 s, (c) 16.31 s and (d) 16.32 s. Spatial resolution is 0.14 mm/pixel.

A second sudden ejection occurs at about 54 s, as shown in Figure 38. Both the steady, diffuse plume and the trajectory of individual particulates have been monitored in the video from which the individual images in Figure 38 were derived. The sustained combustion flame extends 5.6 – 6.5 mm from the surface. The trajectory of a 1 mm particulate is observed detached from the surface by about 2 mm with an estimated velocity of 31 cm/s. Apparently, micro-cracks in the porous graphite occasionally develop, ejecting burning particulates into the gas plume. The intensity and frequency of these events is greater at higher irradiance levels. During the quiescent periods, the combustion mechanism may be evaluated by heterogeneous oxidation of the surface to produce CO (and maybe some CO_2) followed by homogeneous, gas phase conversion of

CO to CO_2. During the micro eruptions, reactions at the surface of the ejected particulates may dominate.

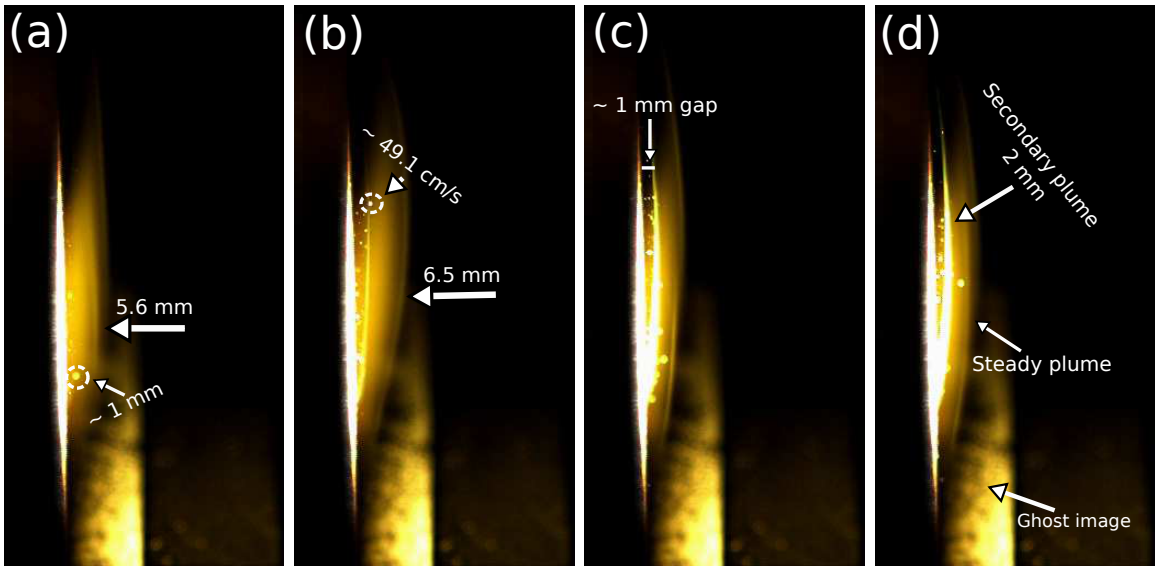

Figure 38. High-speed visible imagery of steady-state diffuse plume and secondary plume of laser irradiated graphite at 777 W/cm^2 at (a) 54.48 s, (b) 54.53 s, (c) 54.58 s and (d) 55.60 s with a 0.14 mm/pixel spatial resolution. The ghost image is due to an out-of-focus image of a bright source in the field-of-view of the camera.

Spectral Analysis

A portion of the MWIR spectrum between 1900 - 2500 cm^{-1}, highlighting the CO_2 antisymmetric stretching band and CO fundamental band emission is shown in Figure 39a. The spectrum is for a single pixel located 1.4 mm from the surface, near the center of the beam at (x,y) = (1.4 mm, 35.3 mm), and averaged temporally from 41 – 120 s. The CO_2 emission dominates over the weaker CO emission lying on the red wings of the CO_2

absorption by the colder CO_2 in the atmospheric path to the IFTS instrument. The signal to noise at the peak of the spectrum is 87:1. The imaginary portion of the Fourier transform is not shown, but less than 22 μW /(cm^2 sr cm^{-1}) with little spectral structure. Also shown in Figure 39b are the spectral basis functions for CO_2 and CO at 2995 K. The instrument spectral resolution of 2 cm^{-1} coincides with the CO rotational spacing, giving rise to the odd structure for CO rotational lines obtained in Figure 37b from convolving the CO monochromatic spectral emissivity with the instrument line shape.

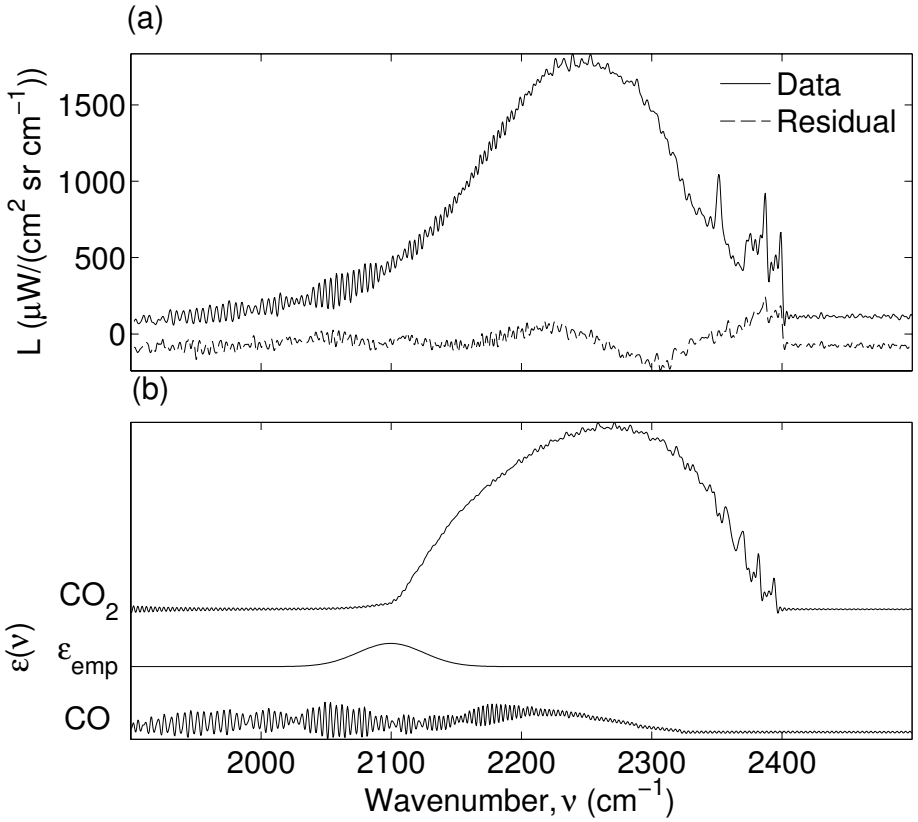

Figure 39. (a) Time averaged (41 s ≤ t ≤ 120 s) spectral radiance for (x,y) = (1.4 mm, 35.3 mm). (b) Spectral basis functions from LBLRTM and optional empirical emissivity, without atmospheric attenuation.

To extract emitter column densities and plume temperature from the observed spectra, a line-by-line radiative transfer model (LBLRTM) [26] and two statistical narrow band models [30, 31] were employed. First consider the line-by-line model, a simplified single-layer LBLRTM [26] was developed to extract temperature and effluent concentrations from emissive plumes. By ignoring scattering and assuming that the plume is in local thermodynamic equilibrium (LTE), the spectral radiance, L, is expressed as:

$$L(\tilde{\nu}) = \int \tau_{atm}(\tilde{\nu}')\varepsilon(\tilde{\nu}')B_p(\tilde{\nu}',T)ILS(\tilde{\nu}-\tilde{\nu}')d\tilde{\nu}' \tag{32}$$

where τ_{atm} is the atmospheric transmittance along a 47 cm path between the imaging spectrometer and the plume, ε represents the plume's spectral emissivity, B_p is Planck's distribution for blackbody radiation at temperature T, and ILS is the instrument spectral lineshape. The instrument line shape (ILS) function is controlled by the interferogram length and symmetry as well any apodization function [100]. For our model no apodization function was applied, and the line shape is the canonical FTS function $ILS(v) = 2a\ \mathrm{sinc}(2\pi av)$, where $a = 0.3$ cm is the instrument maximum optical path difference (MOPD). The spectral emissivity is defined by Equation (33) as:

$$\varepsilon(\tilde{\nu}) = 1 - \exp\left(-\sum_i l\xi_i N\sigma_i(\tilde{\nu},T)\right)\tau_p\tau_{emp} \tag{33}$$

where, ξ_i is the i^{th} species volume mixing fraction, and l is the path length through the plume which is assumed constant and taken approximately as the laser beam diameter of 4.46 cm. N is the total gas density defined by the ideal gas law. The absorption cross-section σ_i for the i^{th} molecule is computed using the HITEMP [101] extension to the

HITRAN [102] spectral database and includes the temperature dependent partition function. Also, particulate (soot) transmittance, τ_p, is assumed to be independent of frequency (i.e., a gray body). Other soot models include a logarithmic polynomial that is frequency-dependent [103]. In previous fiberglass studies [25], the particulate transmittance τ_p was ~ *1,* consistent with a small soot volume mixing fraction. The sensitivity of the fit parameters to the soot model was rather weak. The emission intensity at 2400 – 2500 cm^{-1} is low and largely due to soot. With a soot volume fraction constrained at 0.2 %, the modeled intensity in this spectral region was more than four times larger than observed. Even at this high soot fraction, the choice of soot model influences temperature extraction by less than 7 K and column densities by less than 5% [25]. A gray body particulate transmittance is used in our model for simplicity.

An optional empirical transmittance, $\tau_{emp} = exp\ (-A)$, where A is a Gaussian function to improve the quality of the fit at T > 2500 K using LBLRTM. The Gaussian function is defined as:

$$A(\nu) = c_1 \exp\left[-\frac{(\nu - c_2)^2}{c_3}\right] \tag{34}$$

The evaluation of high gas temperatures (T > 2000 K) remains a challenge for radiative transfer modeling, particularly for the 4.3 μm CO_2 band where spectral databases are rather limited. The HITEMP databank contains line-by-line parameters for a few molecules (H_2O, CO_2, CO, NO, and OH) that are of particular interest in combustion. The latest version, HITEMP-2010 [101] includes a previous version of the carbon dioxide spectroscopic databank (CDSD) [138]. The latest CDSD version, CDSD-

4000 [108] was designed for the temperature range between 2500 - 5000 K, and was developed based on the effective Hamiltonian and effective dipole moment operators. The parameters of these operators were adjusted to fit experimentally observed line position and intensities [139, 140]. However, there's a lack of extensive experimental infrared data for combustion gases at very high temperatures, particularly for the 4.3 μm CO_2 band. In the work from Modest and Bharadwaj [107] and Bharadwaj and Modest [141], the CDSD and HITEMP databases were validated up to 1550 K against experimentally measured CO_2 transmissivities for the 4.3 μm band. At the wings of the optically thick 4.3 μm band, HITEMP overestimates the absorption band wing at T > 1300 K, whereas CDSD is in close agreement, perhaps indicating that HITEMP may suffer from incorrectly extrapolated high-temperature lines [142]. Recently, the CO_2 spectral radiance in the infrared was investigated experimentally by Depraz et al. [106, 142] at very high temperatures of up to 5000 K and compared against currently available spectral databases. It was shown that the theoretical simulations overestimated the experimental results, except at the band wing where the CDSD was in close agreement at these elevated temperatures.

Best estimates for the plume concentrations and temperature are obtained from nonlinear fit of Equation (32) to the observed spectra, using a Levenberg-Marquardt algorithm. The average fit residual for Figure 37a is 100 μW /(cm^2 sr cm^{-1}) and is 10 % larger than the instrument noise. The best estimate for the effective gas temperature is 2999 ± 395 K, with column densities of 7.06 ± 0.06 10^{17} CO_2 molec/cm^2 and 7.44 ± 0.06 10^{17} CO molec/cm^2, for Figure 39a. The statistical error bounds represent the 95 %

confidence intervals and do not include systematic error bounds associated with the spectral model or non-uniformity of the plume along the instrument line-of-sight. In particular, the quality of the fit in Figure 39a requires the inclusion of the empirical emissivity of Equation (34) with a peak emissivity value of $c_1 = 0.03$, centered at $c_2 = 2100$ cm^{-1} and of width $c_3 = 35$ cm^{-1}. This optional empirical emissivity, ε_{emp} was necessary to improve the quality of the fit at T > 2500 K, where HITEMP underestimates the intensity in the band wings, as discussed in detail below [106-108, 141].

To interpret and validate the addition of this empirical emissivity at high temperatures, we have selected from the literature [143] an observed spectrum of the 4.3 μm CO_2 band at 2850 K and simulated the experimental high-temperature CO_2 spectral emissivity. The simulated spectral emissivities from HITEMP with and without the optional empirical emissivity as well a prediction from the CDSD-4000 database are shown in Figure 40. To simulate the experimental data, a triangular apodization function was assumed with an interferogram length of 0.15 cm for a qualitatively agreement for simulating the observed spectra. These prior observations [143], were at a pressure of 2 atm, a temperature of 2850 K, and a path length of 2.34 cm. The experimental data from reference [143], contained a considerably high water concentration (24% CO_2, 35% H_2O and 18% CO) when compared with the current work.

The CO_2 absorption cross sections in HITEMP-2010 are derived from the CDSD-1000 database and lead to lower emission than observed in the wing of the CO_2 band. Depraz et al. [106] performed a similar comparison of the CDSD-4000 and HITELOR databases against experimental emission of CO and CO_2 at high temperatures in a

sapphire tube. At 3200 K, the observed spectral radiance was overestimated by these two databases. The radiative transfer modeling of the CO_2 4.3 μm band at elevated temperatures remains a challenge.

The addition of an optional empirical emissivity parameter produces comparable qualitatively results to CDSD-4000. The HITEMP database with the optional empirical emissivity was chosen for simplicity. The empirical emissivity parameters in Figure 38 are $c_1 = 0.1$, centered at $c_2 = 2079$ cm^{-1} and of width $c_3 = 150$ cm^{-1}, centered around the same position as ε_{emp} with a small peak emissivity contribution as seen previously in Figure 39b.

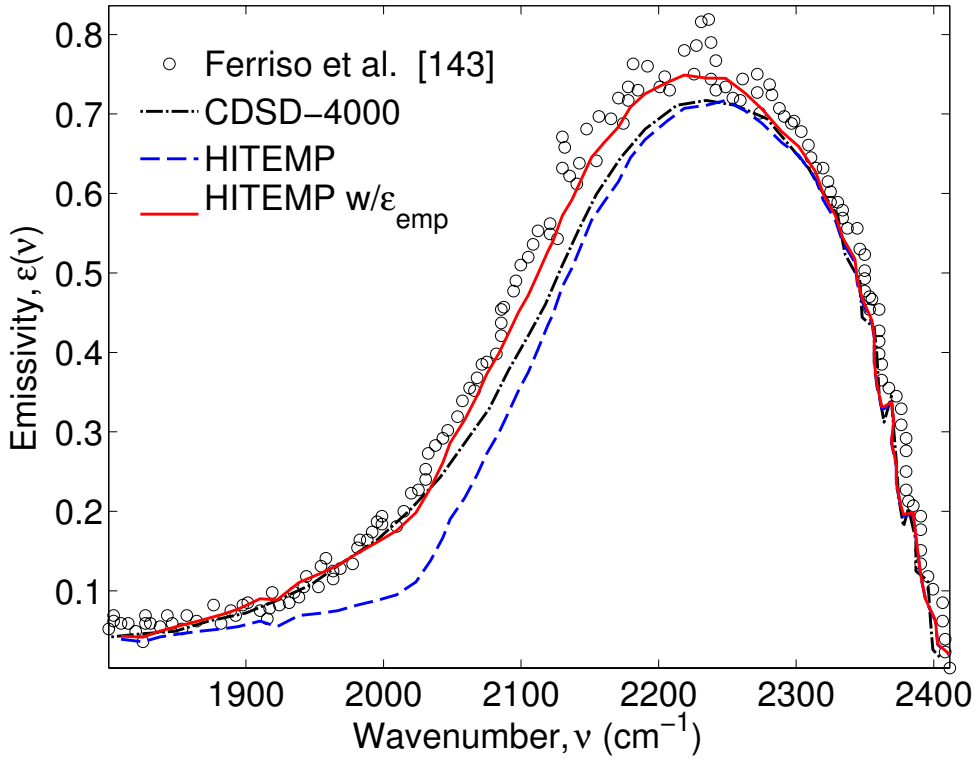

Figure 40. Experimental [143] and simulated emissivity of CO_2, H_2O and CO at 2850 K in the 4.3 μm region.

To further evaluate the systematic error associated with this approach, the LBLRTM is compared with two statistical narrow band models. In contrast to line-by-line calculations, narrow band models average the spectral absorptivity over a narrow spectral bandwidth (~ 25 cm^{-1}) producing a smoother absorption coefficient. RADCAL [31] and EM2C [30] narrow band models have been widely used in numerous heat transfer calculations to interpret combustion plumes. EM2C contains statistical narrow band parameters based on HITRAN and proprietary French high-temperature extensions [30]. RADCAL gas mixture transmissivities are based on experimental data. A FORTRAN code provided with both narrow band models, allows calculation of the spectral transmissivities of combustion gases such as CO, CO_2, H_2O, CH_4, and soot. These two narrow band models are less accurate for temperatures above 2500 K. Modest and Bharadwaj [107] compared experimental CO_2 transmissivities with RADCAL and EM2C, which agreed very well with the measured spectra at temperatures above 1300 K for the 4.3 μm band. Demonstrating that the narrow band models accurately predicted measured CO_2 spectral transmissivity up to 1550 K measurably better than HITEMP. However, these spectral models have not been validated with experimental data on combustion gases at elevated temperatures (> 2000 K).

The narrow-band models were combined with the LBLRTM to predict the CO_2 spectral transmissivity. The spectral emissivity of CO was computed using the line-by-line parameter of the HITEMP database as defined in Equation (33) due to the highly structured ro-vibrational band at the 2 cm^{-1} instrument spectral resolution. The modeled plume spectral emissivity in Equation (32) was modified to include the transmittance of

CO_2 derived from EM2C and RADCAL. The quality of the fit along with the acquired statistical results for each model are then compared to obtain systematic error associated with the different spectral models.

In order to compare the fit quality from the different spectral models at different temperatures, single data cubes at t = 9, 23 and 100 s are compared. These hyperspectral data cubes were spatially averaged in the vertical direction (y-direction) from 9.36 - 54.0 mm at x = 0.72 mm, approximately equal to the laser beam diameter (44.6 mm). Figure 41a shows a single unprocessed broadband image at t = 9 s with a rectangular box indicating where the spatial averaging was done. The corresponding spatially averaged spectral radiance is provided with its corresponding spectral model derived from LBLRTM, RADCAL and EM2C in Figures 41b-c, respectively. The optional empirical emissivity parameter was not employed to improve the quality of the fit in Figure 41b. Best estimates of plume temperature and column densities of CO and CO_2 in the gas-phase were obtained from these spectral models. At t = 9 s the LBLRTM yielded an effective gas temperature of 1954 ± 18 K, whereas RADCAL and EM2C gave temperatures of 1937 ± 90 K and 1906 ± 10 K, respectively. The HITEMP database appears to be in reasonable agreement with the experimental data at ~ 1900 K in Figure 39a. As seen from Figures 41b-c the fit residuals seem adequate at this temperature for all spectral models. From the experimental data in Figure 41, no spectral features of the P- and R- branch emission lines that arise from the fundamental CO band between 2000 to 2220 cm^{-1} were detected from IFTS. However, strong emission of the CO_2 anti-symmetric band is observed. Effective CO_2 column densities of 3.46 ± 0.05 molec/cm^2,

2.83 ± 0.03 molec/cm^2, and 3.60 ± 0.02 molec/cm^2 from LBLRTM, RADCAL and EM2C were obtained respectively.

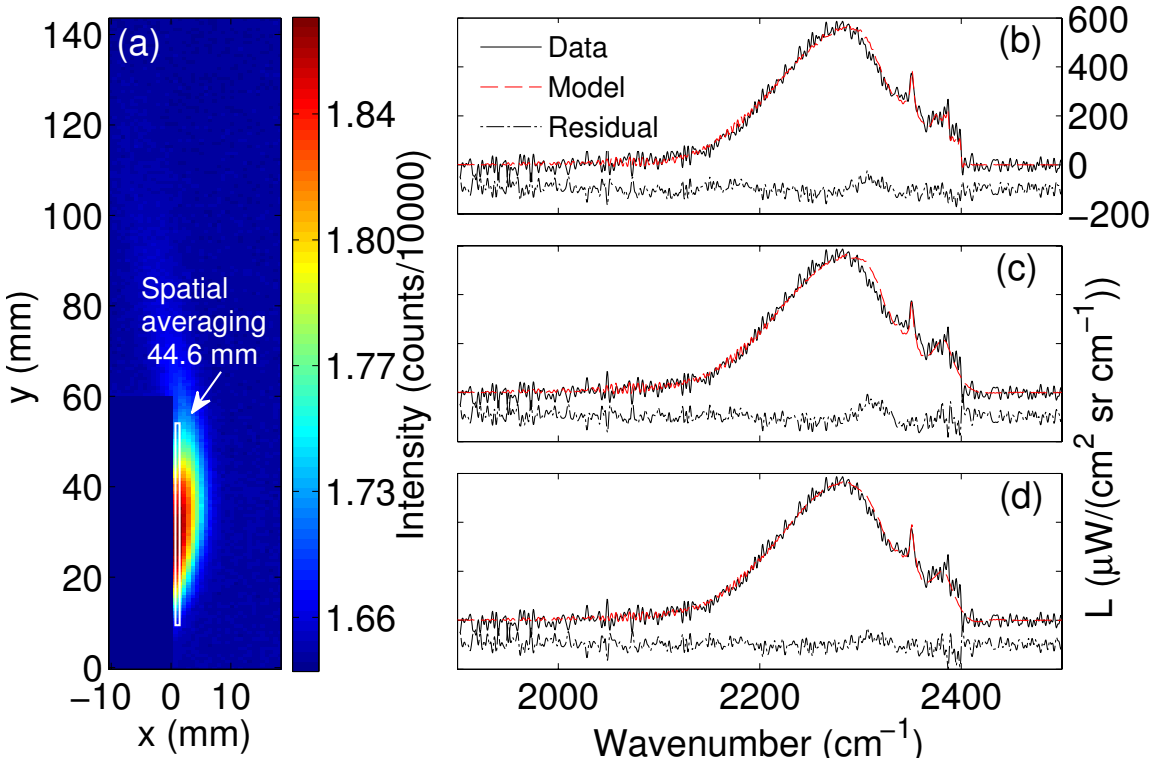

Figure 41. (a) Un-processed broadband image at 9.2 s with rectangular box indicating spatial averaging (9.36 mm ≤ y ≤ 54.0 mm) for observed data at x = 0.72 mm and modeled by (b) LBLRTM, (c) RADCAL and (d) EM2C.

The observed spectral radiance with their spectral fits are shown in Figures 42a-c for t = 23 s and Figures 42d-f for t = 100s. Table 6 summarizes the statistical results from the nonlinear fit at t = 9, 23 and 100 s. The reported statistical uncertainty for each of the result is defined as the half-width of the 95% confidence interval and does not

include systematic errors associated with the assumption of a homogeneous plume or the effects of turbulence. Note that the optional empirical emissivity parameter was only used at t = 100 s or T ≅ 2900 K. Overall the three spectral models yielded low statistical errors of $\Delta T \leq 90$ K as well with 1 and 13 % in CO_2 and CO column densities respectively. The systematic errors associated with different spectral models are on the order of $\Delta T \pm 15$ K for plume temperature up to 2500 K, and ± 18 % for column densities. However, at gas temperatures above 2500 K, spectral modeling of the observed combustion gases becomes challenging due to underestimation of the band wing (high J) of the 4.3 μm fundamental asymmetric CO_2 band and/or overestimation in the core band (low J) from the currently available spectral databases [106-108, 141]. Based on the quality of the fit, LBLRTM and RADCAL had the smallest residuals. The evolved boundary layer plume of laser irradiated porous graphite at 777 W/cm^2 was further investigated by modeling the observed spectral radiance with the LBLRTM. In summary, it was preferred the line-by-line radiative transfer model with the optional empirical emissivity compensating for the CO_2 4.3 μm band wing and the use of a gray-body, soot emissivity for simplicity. The spatial and temporal descriptions of the plume developed below are based on this version of the model. The effective temperatures represent a nonlinear weighting along the IFTS line of site.

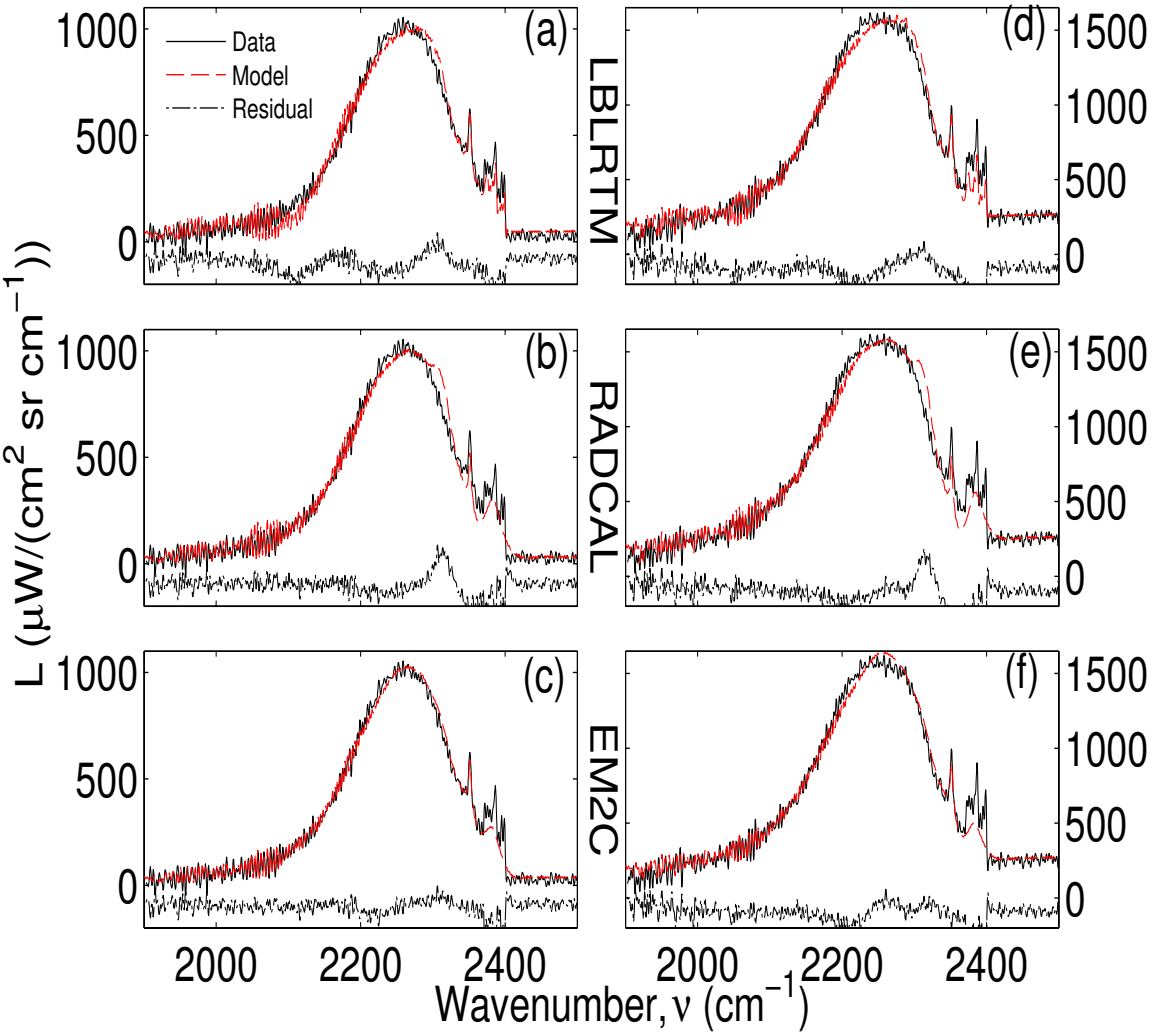

Figure 42. Comparison of radiative transfer models with observed spectral radiance at x = 0.72 mm for (a)-(c) t = 23 s and (d)-(f) t= 100 s.

Table 6. Summary of statistical results obtained from LBLRTM, RADCAL and EM2C at 9, 23 and 100 s. [a]Gas temperature, (K). [b]Column density, (10^{17} molec/cm^2). *Denotes undetectable spectral signature

	t = 9 s			t = 23 s			t = 100 s		
	[a]T	[b]CO	[b]CO_2	[a]T	[b]CO	[b]CO_2	[a]T	[b]CO	[b]CO_2
LBLRTM	1954 ± 18	*	3.46 ± 0.05	2497 ± 23	4.53 ± 0.40	4.44 ± 0.05	2901 ± 36	5.29 ± 0.54	5.91 ± 0.06
RADCAL	1937 ± 90	*	2.83 ± 0.03	2406 ± 72	4.45 ± 0.43	3.60 ± 0.04	2640 ± 19.42	5.58 ± 0.78	4.71 ± 0.02
EM2C	1906 ± 10	*	3.46 ± 0.05	2512 ± 16	3.37 ± 0.34	3.78 ± 0.05	2900 ± 69	4.08 ± 0.58	4.36 ± 0.003

Profiles of Temperature and Column Densities

Temporal variations in plume temperature and column densities were investigated by spatially averaging column pixels along the y-direction between 9.36 – 54.0 mm, a distance equal to the laser beam diameter of ~ 44.6 mm, as seen from Figure 41a. The observed spectral radiance was modeled using LBLRTM for the plume boundary layer in the first 3 millimeters from the surface (x-direction). Figure 43 shows the best estimate of temporal gas-phase temperature from radiative transfer modeling and the measured graphite surface temperature from high and low temperature optical pyrometers. The surface temperature systematic errors associated from both optical pyrometers are larger at lower temperatures with $\Delta T \cong 300$ K and at steady state are of $\Delta T = 142$ K. At 3 mm from the surface, the gas temperature in the boundary layer appears uniform with almost no variation in temperature. Plume temperature rises from 1500 K to steady value of ~ 2900 K while surface temperature reaches a steady value of ~ 2500 K. Initially, the

plume temperature is lower than the surface temperature, but rises above surface temperature at 20 s. At 40 s, the difference between surface and gas temperatures, is ~ 478 K. The rise in gas temperature may be partially attributed to the plume absorption of incident radiation by the plume as it becomes thicker. Similar observations have been reported from the evolved combustion plume of laser irradiated carbon-black pigmented PMMA [52]. For the initial heating period, the process is driven by the growth of buoyancy boundary layer plume near the hot graphite surface, convection from the graphite surface transfer to the plume heating the gas at earlier time. As surface temperature increases, the rate of decomposition products increases at the boundary layer. As the plume becomes thicker, the absorption of laser radiation increases, resulting in attenuation of the incident radiative flux reaching the surface, seen in Figure 43. However, there is a contribution to the increase in plume temperature due to exothermic reactions of decomposition products with air. The laser energy is deposited in the gas phase rather than at the surface due to particulates being ablated towards the boundary layer plume, as seen from visible imagery in Figure 38. The hot particulates absorb the incident laser radiation, acting like blackbody absorbers and consequently increasing the plume temperature. Alternatively, the plume could be hotter because particulates are burning in the flow.

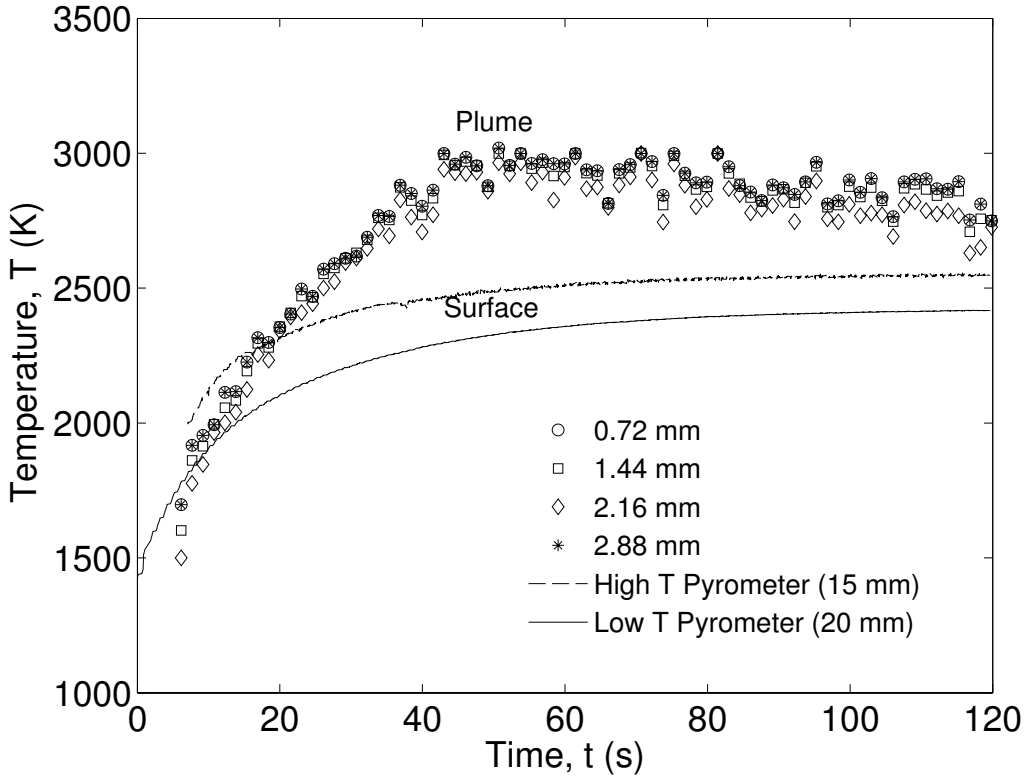

Figure 43. Surface and plume temperature at 0.72 – 2.88 mm.

Although the gas phase plume temperature remained the same from 0.72 to 2.88 mm away from the surface, variations in CO and CO_2 column densities were observed in the plume. Figure 44 illustrates the temporal evolution of CO and CO_2 column densities at various distances from the surface. At 0.72 mm, from the surface-boundary layer, CO_2 concentration is predominant at earlier time. However, the CO fundamental ro-vibrational band was not detected from IFTS. As time progressed, CO concentration increased rapidly until at 25 s it overlapped with CO_2. For the gas-phase temperature range of 1500-2440 K ($t < 25$ s), the CO_2 concentration was higher than CO. At the

surface-boundary layer (0.72 mm) the results suggest that both CO and CO_2 may be produce from the heterogeneous oxidation of carbon at the surface [73, 77].

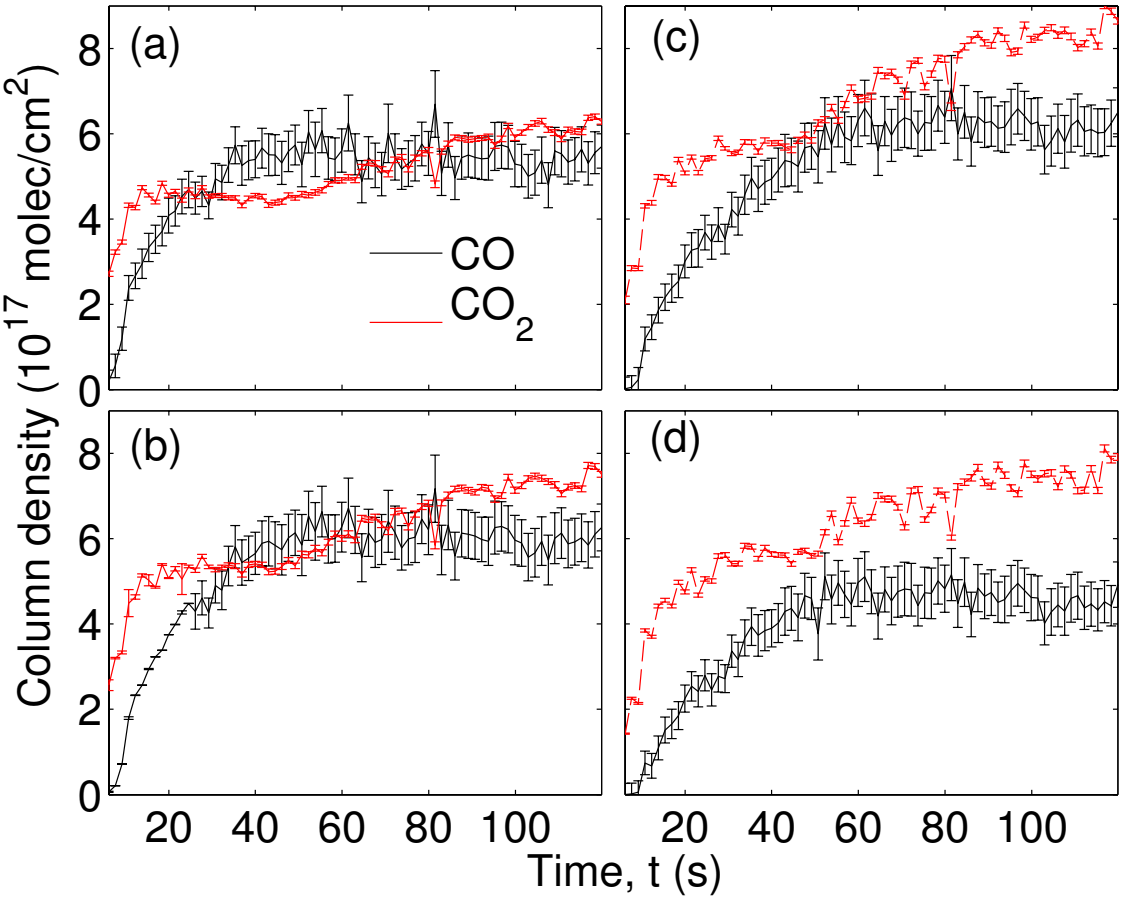

Figure 44. Temporal evolution of CO and CO_2 column densities at (a) 0.72 mm, (b) 1.44 mm, (c) 2.16 mm, and (d) 2.88 mm away from the surface in the boundary layer.

The CO concentration increases above CO_2 at t = 32 s where it continues to rise reaching steady state at 63 s in Figure 44. At later times CO_2 rises further, crossing again with CO where it continues to slightly go up above CO. This rise appears to be associated to the conversion of CO to CO_2 in the gas phase. As distance increases away from the surface towards the boundary layer (Figures 44a to 44d), the rate of CO_2 production grows much rapid farther away from the surface relative to CO.

The spatial distribution of gas-phase plume and molecular species were developed from LBLRTM at steady state in Figure 45. The spatial distributions are for steady-state values at 41 s ≤ t ≤ 120 s. Figure 45a and Figure 45b shows the respective spatial distributions of column densities for CO and CO_2 derived from LBLRTM calculations. Statistical fit uncertainties are small, typically < 7 %. The column densities are significant, ~ 10^{17} molec/cm^2 and comparable to those observed in laminar flames with good combustion efficiency [18]. The molecular species travel upward driven by buoyancy as previously seen from the visible imagery in Figure 38. Also, the overall CO column density expands up to ~ 5 mm away from the surface and up to ~ 80 mm in the vertical direction. On the other hand, the CO_2 column density extends much farther away to x ≅ 6.5 mm and y ≅ 89 mm. At y = 30 mm it can be seen that the CO column density is greater at the surface-boundary layer of x = 0.72 mm than CO_2 and that CO_2 is maximum much farther away in the plume at x = 2.88 mm.

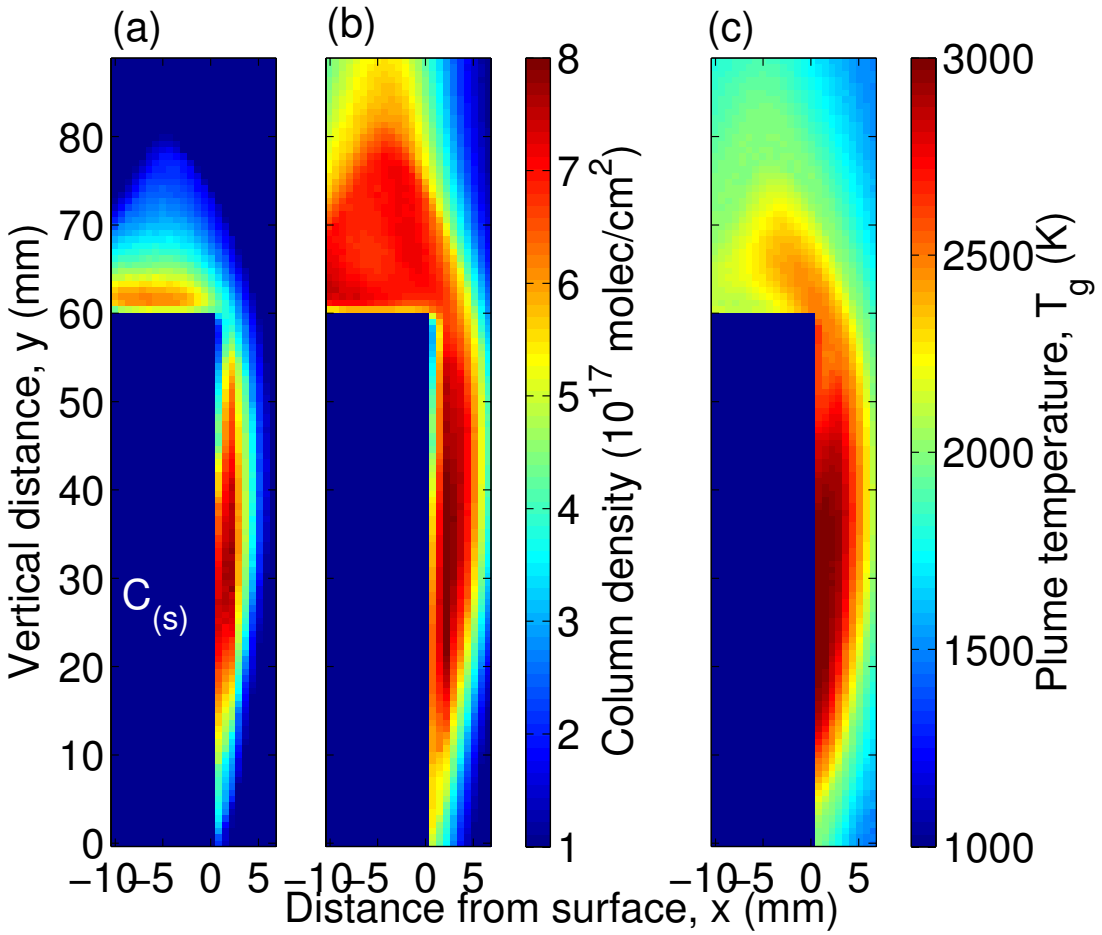

Figure 45. Spatial maps at steady state (41 s ≤ t ≤ 120 s) of (a) CO, (b) CO_2 and (c) plume temperature.

Figure 45c shows the time averaged gas temperature at steady state from LBLRTM. The temperature distribution between y = 17.2 - 51.2 mm is uniform and highest with T_g ~ 3000 K extending up to x = 3 mm. This was previously seen in Figure 43, where temporal temperature distribution is uniform in the plume boundary layer in the first 3 mm away from the surface. The temperature declines as the plume expands

away from the surface and hot gases rise, driven by buoyancy and fume hood flow rate. The statistical fit uncertainty in temperatures are generally small ΔT < 37 K, however in the region where T_g is ~ 3000 K, the statistical error bounds are larger with $\Delta T \sim 250$ K. The larger error bounds are expected at temperatures close to 3000 K due to limitation on the total internal partition sum (TIPS) up to 3000 K [144, 145]. As the plume rises driven by buoyancy it bends at the edge of the graphite target at y = 60 mm where it continues in the free stream towards the fume hood where temperature decreases. The interplay between heterogeneous and homogeneous combustion kinetics reactions are further discussed below.

Discussion

Heterogeneous and Homogeneous Kinetics

The simplified global heterogeneous and homogeneous reactions of carbon oxidation considered in this work are summarized in Table 3. Based on the results in Figure 44a, significant CO_2 concentration was observed at the surface boundary layer interface, it is possible that CO and CO_2 are made at the surface as primary products of the carbon-oxygen global heterogeneous reaction (29) [90-93, 146]. However, general consensus has been that for temperatures greater than 1200 K, the CO_2 production is small [74]. At lower temperatures both CO and CO_2 are present [75, 76]. From experimental results at much higher temperatures, CO_2 at the surface-boundary layer (0.72 mm) is significant. These results agree with Mitchell et al. [78] predictions on surface production of CO_2 for temperatures as high as 1700 K. Moreover, at T < 1573 K, carbon is consumed in a kinetically first order reaction with the stoichiometric equation of $4C + 3O_2 = 2CO_2 + 2CO$, whereas at T > 1770 K, a zeroth-order reaction sets,

corresponding to $3C + 2O_2 = CO_2 + 2\ CO$ [147]. The overall temporal distributions of column densities in Figure 44 are consistent with the global combustion mechanism of producing CO at the surface followed by conversion of CO to CO_2 in the gas phase.

With the assumption that both CO and CO_2 are primary products from the $C_{(s)}$-O_2 reaction, then the primary product ratio, α/β, has the form of Equation (31). The $[CO]/[CO_2]$ product ratio at 0.72 mm is provided in Figure 46, where the product ratio increases with increasing surface temperature ($2157\ K \leq T_s \leq 2530\ K$). This increase indicates the heterogeneous reaction, whereas maximum in the $[CO]/[CO_2]$ ratio must indicates a homogeneous reaction [146]. This inflection is observed with the decrease of the product ratio at $T \sim 2506$ K. An effective activation energy, E_a, of 149.40 ± 10.31 kJ/mol was obtained by fitting the product ratio with Equation (31).

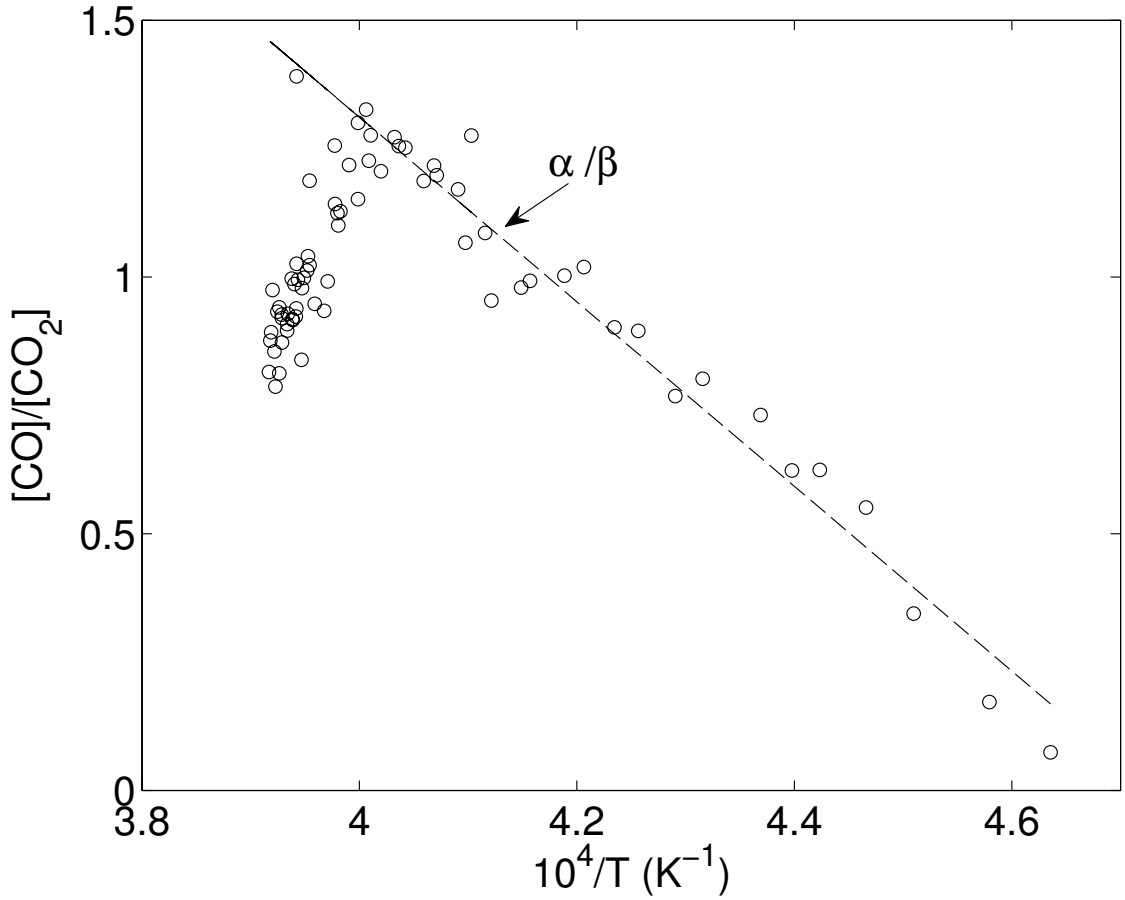

Figure 46. CO/CO_2 ratio as a function of inverse surface temperature at the surface-boundary layer interface (0.72 mm), with $\alpha/\beta = 4910 \exp(-17{,}970/T)$.

The corresponding reaction rate for the surface production of CO and CO_2 in Equation (29) is defined as [90-93]:

$$\begin{aligned} R_{29} &= k_{29}[O_2] \\ k_{29} &= (3.01x10^5\, m/s)\exp(-17{,}966/T) \end{aligned} \tag{35}$$

where, $[O_2]$ is the bulk oxygen concentration (20 % in air), k_{29} is the rate constant for reaction (29) and T is the surface temperature. The activation energy for the global

heterogeneous reaction (29) is E_a = 149.37 kJ/mol [90-93]. For laser irradiated graphite at 777 W/cm^2, the obtained effective activation energy from Figure 46 is in agreement with the activation energy of reaction (29), suggesting production of CO and CO_2 at the surface-boundary layer of 0.72 mm for the higher surface temperatures of 2157 - 2530 K.

By following the same analysis in Figure 46, effective activations energies for the [CO]/[CO_2] ratio were computed for the temporal data obtained earlier in Figures 44(b-d). Figure 47 shows the effective activation energies obtained from Eq. (16) for the boundary layer plume from 0.72 to 2.88 mm. As distance increases, the effective activation energy decreased. At 0.72 and 1.44 mm, the corresponding effective activation energies were 149.40 ± 10.31 kJ/mol and 140.17 ± 9.39 kJ/mol respectively. These results, up to 1.44 mm away from the surface, agree with the heterogeneous reaction activation energy for the formation of CO and CO_2. Moreover in the boundary layer at 2.16 mm, an effective activation energy of 128.70 ± 8.69 kJ/mol appears to agree with the Howard et al. [96] value of 125.52 kJ/mol for homogeneous reaction (30) in the gas phase.

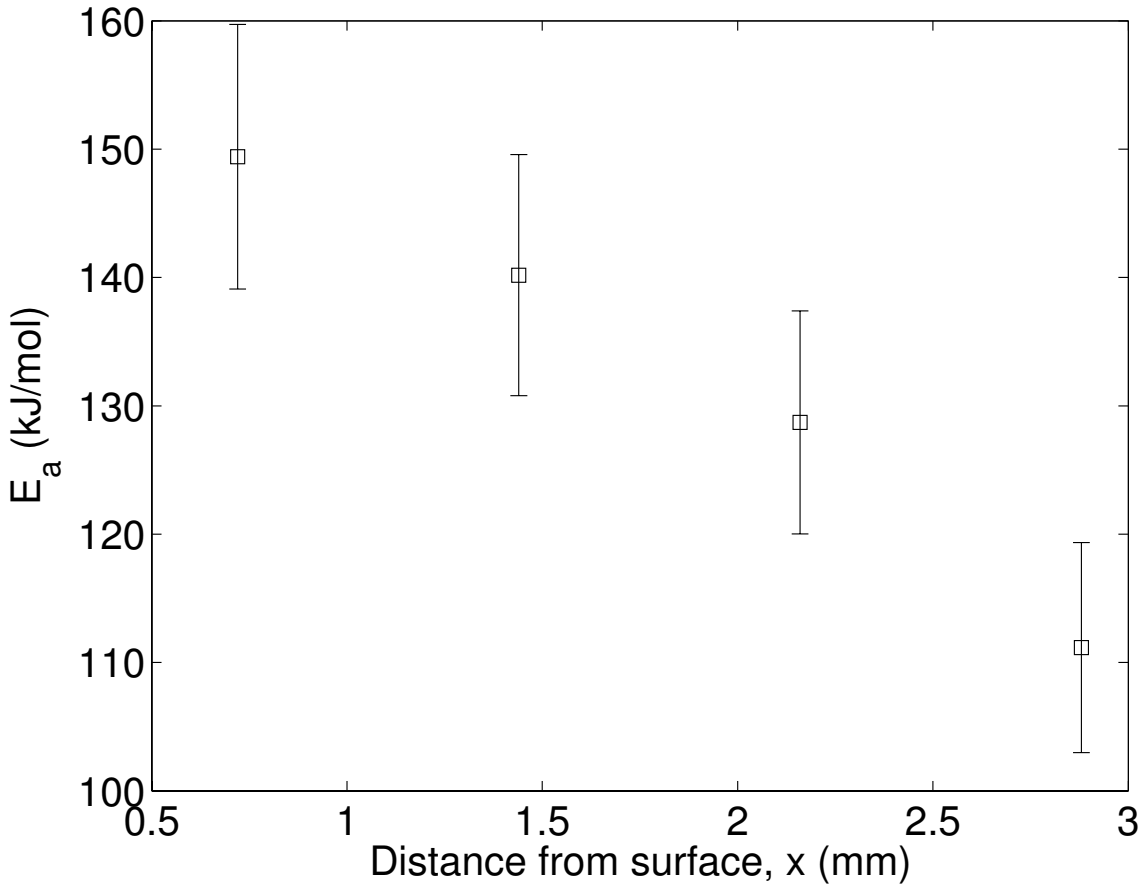

Figure 47. Effective activation energies as a function of distance from the surface towards the boundary layer.

The corresponding reaction rate for the homogeneous reaction (30), R_{30}, is defined as [96]:

$$R_{30} = k_{30}[CO]$$
$$k_{30} = (1.3x10^{11} m^3 / kmol \cdot s)[H_2O]^{1/2}[O_2]^{1/2} \exp(-15{,}098/T) \quad (36)$$

where, k_{30}, is the rate constant for reaction (30), $[CO]$ and $[H_2O]$ are the carbon monoxide and water vapor concentrations, respectively. It has been reported that small

amounts of water vapor in the free stream acts as a catalyst on the CO oxidation in the gas phase [79, 148].

Linjewile et al. [146] derived an analytical solution for the concentrations profiles of CO and CO_2 by considering the global oxidation reactions in Table 3 with the addition of the endothermic heterogeneous reaction (37) and its corresponding reaction rate defined as [90-93]:

$$C + CO_2 \xrightarrow{k_{37}} 2CO \tag{37}$$

$$\begin{aligned} R_{37} &= k_{37}[O_2] \\ k_{37} &= (6x10^7\, m/s)\exp(-29{,}790/T) \end{aligned} \tag{38}$$

The CO/CO_2 product ratio can be predicted from Linjewile et al. [146] analytical solution defined as:

$$\begin{aligned} \frac{[CO]}{[CO_2]} &= \frac{\psi + 2\zeta}{(1+\eta)(1+\zeta)\exp\{-\eta(1-2r/d_a)\} - \psi - 2\zeta}, \\ \psi &= \frac{\alpha/\beta}{\alpha/\beta + 1} \\ \zeta &= \frac{k_{37}(0.5\alpha/\beta + 1)}{k_{29}(\alpha/\beta + 1)} \\ \eta &= \sqrt{k_{30}\phi} \end{aligned} \tag{39}$$

where, $2r/d_a$ is the dimensionless radial position, $\phi = d_a/2D_{eff}$, d_a is the particle diameter and D_{eff} is the effective diffusivity. Since this model was developed for the combustion of a spherical graphite particle, ϕ is taken as an adjustable empirical parameter to predict the experimental data of Figure 46.

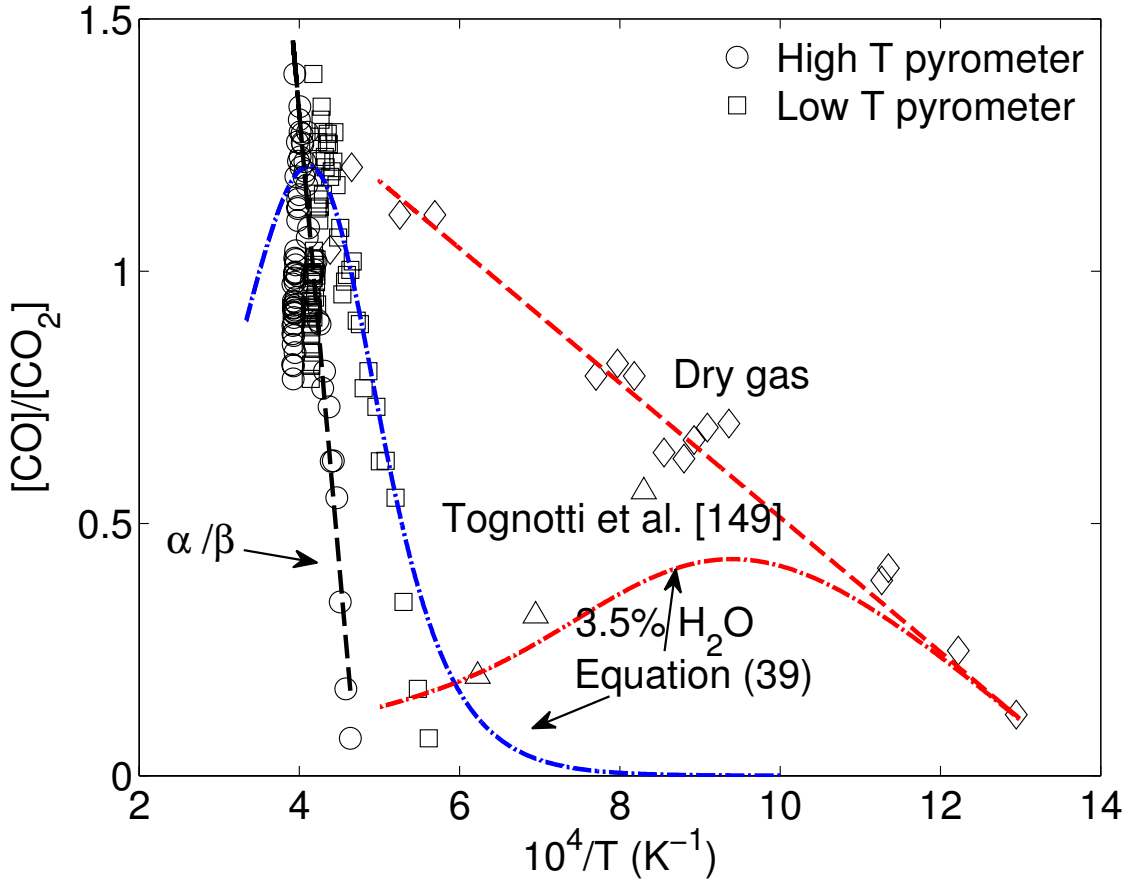

Figure 48. Comparison between the CO/CO_2 product ratio predicted by Equation (39) with experimental data (1.2 % relative humidity) at x = 0.72 mm and Tognotti et al. [149] data with 20 % oxygen in dry gas and 3.5 % relative humidity.

The obtained CO/CO_2 ratio at x = 0.72 mm, is compared with the prediction of Equation (39) in Figure 48. The data is shown as a function of the inverse surface temperature from both optical pyrometers. At lower temperatures, Equation (39) agrees with the low temperature optical pyrometer measurements. However at the higher temperatures (T > 2500 K) where the $[CO]/[CO_2]$ ratio decreases (rollover), the model

overestimates the data by 3 %. When comparing with Tognotti et al. [149] experimental data with 3.5 % water vapor in a 20 % oxygen atmosphere, their results rolls much quicker at lower temperatures. This increase indicates heterogeneous reaction, whereas the rollover in the $[CO]/[CO_2]$ ratio must reflect homogeneous reaction [146]. From our experiments with a much lower water vapor concentration of 1.17 %, the $[CO]/[CO_2]$ inflection occurs at much higher temperature, somewhere in between the dry and humid data points of Tognotti et al. [149]. Since water vapor act as a catalyst in the homogeneous reaction, the rollover will occur much rapidly at higher water vapor concentrations as seen from Figure 48 [79, 146, 148]. Table 7, compares Linjewile et al. [146] simulation parameters and the empirical parameters used to predict the results of Figure 46. For model calculations using Equation (39), ϕ was taken as an adjustable empirical parameter to account for the effective diffusivity and surface length, the bulk oxygen water concentrations were taken as 20 and 1.17 % respectively. This adjustable empirical parameter ϕ was much lower than Linjewile et al. [146] reported value, suggesting that the assumed effective diffusivity from their model is inadequate to model our data. The dimensionless radial position, $2r/d_a$, was assumed as 1.6. The activation energy for reaction (37), $B = E_a/R$, was modified to 33,790 K to improve the model prediction with our results, which is within 10 % of other reported values in the literature [75, 150]. Equation (39) does not account for bulk graphite targets, surface porosity, sub-surface reactions within the pores and particulates being ejected into the combusting gas plume. Hayhurst and Parmar [73] tabulated the measured α/β ratio from the literature, where the empirical effective activation energies varied depending on the type of carbon.

Also, the results in Figure 46, requires a large activation energy in the α/β ratio, consistent with Mitchell [151] combustion of coal char particles. Overall, Equation (39) requires an empirical modification to model the present laser irradiated porous graphite data. However, this empirical modification is inadequate to account for particulates being ejected into the plume and sub-surface reactions, seen from Figures 37-38.

Table 7. Comparison of simulation parameters for Equation (39).

Simulation parameters	Linjewile et al. [146]	Current work
H_2O	3.5 %	1.17 %
O_2	20 %	20 %
α/β	70 exp(-3,070/T)	4910 exp(-17,970/T)
k_{37}	6×10^7 exp(-29,790/T)	6×10^7 exp(-33,790/T)
ϕ	1.20×10^{-5}	0.20×10^{-7}

The heterogeneous and homogeneous kinetics interplay has been shown primarily from numerical simulations for porous graphite in steady state [87, 88, 150]. With the ability to investigate the evolved combustion plume at high spatial resolutions of 0.52 mm^2 per pixel, the gas temperature with the CO and CO_2 column densities profiles in the buoyant flow direction at steady-state surface temperature (~ 2500 K) is shown in Figure 49. The inset in Figure 49 shows the path along the buoyant flow where plume temperature and effluent concentrations were plotted as a function of time, *t*, represented as $t = d/v$, where the vertical y-distance is *d,* and an estimated macroscopic plume velocity from the visible imagery (Figure 38) is taken as $v \sim 491$ mm/s.

The results in Figure 45 are consistent with the global heterogeneous and homogeneous reactions where CO is being made close to the surface and later oxidizing

to CO_2 in the gas boundary layer. A secondary plume that evolves from the surface was seen in the visible imagery (Figure 38d) at ~ 2 mm from the surface. This was correlated with observations in the time averaged CO column density map in Figure 45a with a similar shape of a bright plume jet at ~ 2 mm away from the surface, where CO concentration is highest. From Figure 49, CO column density is greater than CO_2 at the surface-boundary layer of 0.72 mm (t = 0.05 s), as time increases CO_2 column density continues to increase along the boundary layer while CO declines rapidly. When comparing Figure 49 with Chelliah et al. [88] numerical simulations of porous graphite at surface temperatures of 2000 K, these results are qualitatively consistent with the kinetics interplay between heterogeneous and homogeneous reactions, where surface reactions increases the surface flux of CO thus oxidizing along the boundary layer to produce CO_2, similar to a double film structure [75]. Also, Chelliah et al. [88] showed a monotonic variation in the CO_2 column density in moist air. As surface temperature increases, the distance to the peak gas-phase CO_2 column density becomes greater, where at T_s = 2000 K, the flame location is ~ 1.0 mm [88]. At higher surface temperature of ~ 2500 K, we observed that CO_2 peaked at ~ 2.0 mm, qualitatively consistent with their simulations of increasing distance.

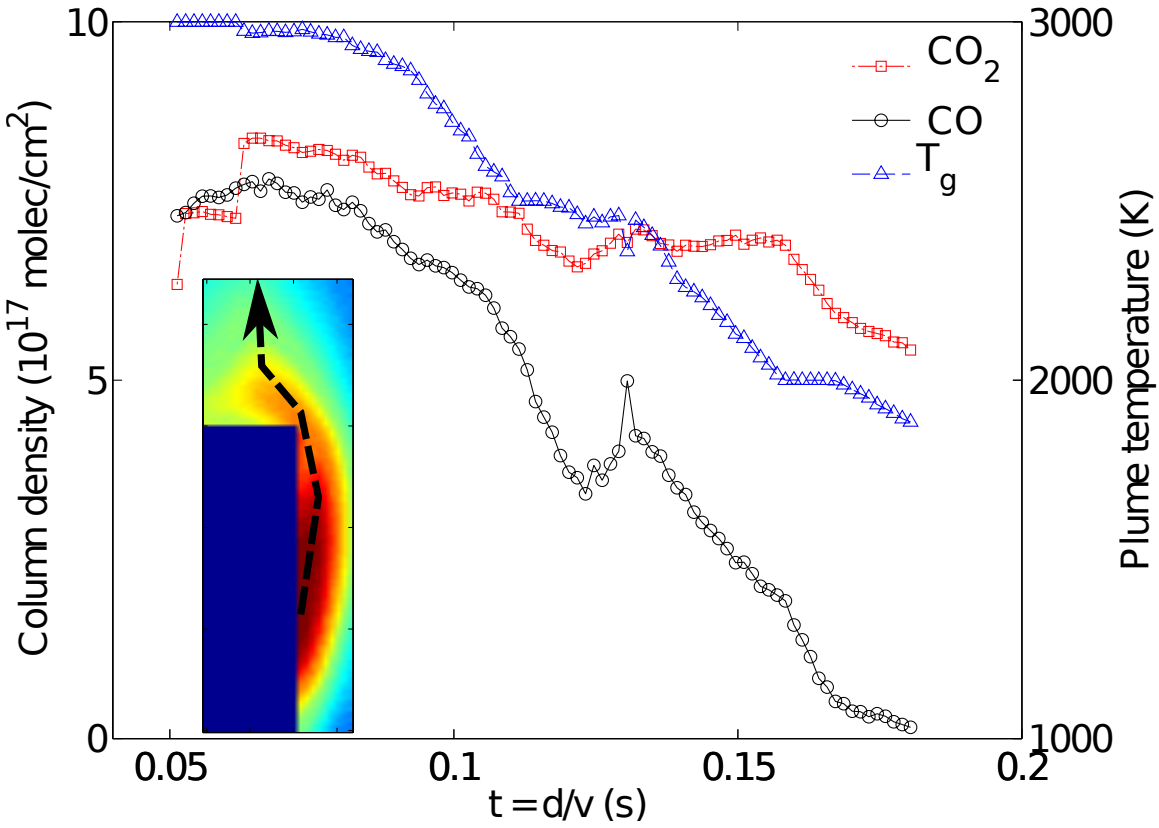

Figure 49. Profiles of gas-phase species column density and plume temperature along the buoyant driven boundary layer, with surface temperature at ~ 2500 K as a function of t = d/v. *Inset:* spatial plume temperature map with vector showing the path parallel to the surface along the boundary layer driven by the buoyant flow of the shown profiles.

Conclusions

The combustion plume characteristics from porous graphite targets irradiated in the range between 0.2 – 4 kW/cm^2 were shown from high-speed imagery. As laser irradiance increases, the evolved combustion plume extends farther away from the surface and bends towards buoyancy. This effect is more dramatic at 4 kW/cm^2, where

the plume fluid dynamics change radically due to a large flux of CO, CO_2 and carbon particulates emanating from the surface. A detail fluid dynamics analysis to understand this effect will be explored in future work. Emissive plumes from laser irradiated graphite at 0.8 kW/cm^2 were quantified from hyperspectral imaging-FTIR. A simplified homogeneous, single-layer, radiative transfer model was developed to model temporal and spatial distributions of plume temperature and column densities. At surface temperatures as high as 2500 K, the heterogeneous reaction corresponded to the primary combustion products of CO and CO_2, as observed at the surface-boundary layer interface (0.72 mm). Further from the surface towards the boundary layer, CO conversion to CO_2 was observed, agreeing with the global homogeneous reaction of Howard et al. [96]. The $[CO]/[CO_2]$ ratio at x = 0.72 mm, was compared with Linjewile et al. [146] analytical solution. At lower temperatures, the analytical solution predicted the results. However at the higher temperatures (T > 2500 K) where the $[CO]/[CO_2]$ ratio decreases (rollover), the model overestimates the data by 3%. This increase indicates heterogeneous reaction, whereas the rollover in the $[CO]/[CO_2]$ ratio must reflect homogeneous reaction [146]. Since water vapor act as a catalyst in the homogeneous reaction, the rollover will occur much rapidly at higher water vapor concentrations [79, 146, 148]. Overall, with Linjewile et al. [146] analytical solution required an empirical modification to model the present laser irradiated porous graphite data. However, this empirical modification was inadequate to account for particulates being ejected into the plume and sub-surface reactions. The steady-state CO, CO_2 and plume temperature profiles along the buoyant driven boundary layer plume, were consistent with Chelliah et al. [88] numerical

simulations of porous graphite, where surface reactions increases the surface flux of CO thus oxidizing along the boundary layer to produce CO_2, similar to a double film structure [75]. We intend to explore the combustion kinetics of graphite targets in laminar flows of M = 0.2 – 0.9 at high spatial resolutions to benchmark experiments with detailed reactive fluid dynamics simulations.

VI. Conclusions

Hyperspectral imaging FTIR was first developed to investigate the evolved emissive plumes of laser irradiated FRP, PMMA and graphite targets at close focal distances. The first two-dimensional boundary layer spatial maps of plume temperature and effluent concentrations were reported for irradiated targets at high spatial resolutions (0.52 to 0.81 mm^2/pixel). The use of a simplified homogeneous single layer line-by-line radiative transfer model proved to be adequate to retrieve species concentrations and plume temperature both spatially and temporally with low statistical errors. Statistical narrow-band models (EM2C and RADCAL) were validated with experimental combustion data at temperatures as high as 2900 K. Imaging FTIR also proved to be an efficient tool for investigating the laser beam profile and surface temperature distributions both temporally and spatially. A simplified analysis on the heating process allowed understanding the influence of laser wavelength (λ = 10.6 μm and λ = 1.06 μm) on surface heating rates. Effective activation energies were obtained from the temporal evolution of molecular species at the surface-gas boundary layer. These were correlated with established kinetics models, demonstrating the applicability of IFTS for kinetics interpretation at high spatial resolutions.

The spectral analysis at gas temperatures of 1000 K yielded statistical errors of ± 6 K, however systematic errors associated with the radiative transfer model was greater than 100 K. At plume temperatures as high as 2900 K, the LBLRTM and statistical narrow band models (EM2C and RADCAL) were employed to fit the data. Comparisons were made with the different spectral models to determine their statistical and systematic

errors. Overall, the three spectral models yielded low statistical errors of $\Delta T \leq 90$ K and less than 13% in molecular species column densities. The systematic errors associated with different spectral models are on the order of $\Delta T \pm 15$ K up to plume temperatures of 2500 K and approximately ~ 18 % in species concentration. However, at gas temperatures above 2500 K, spectral modeling of the observed combustion gases became challenging due to underestimation of the band wings of the 4.3 μm fundamental asymmetric CO_2 band or overestimation of the central CO_2 spectral radiance derived from the currently available spectral databases [106-108, 141]. In the region where the gas temperature was ~ 3000 K, the statistical error bounds are larger with $\Delta T \pm 250$ K. The large error bounds at these elevated temperatures were due to limitation on the total internal partition sum (TIPS) up to 3000 K that is used in the LBLRTM [144, 145].

The instrument signal-to-noise ratio (SNR) at the peak of the spectrum exceeded 87:1 for plume temperatures above 2900 K with a 2.0 ND filter, whereas SNR exceeded 60:1 using a 0.3 ND filter at ~ 1300 K. The imaging-FTIR spectrometer 16-tap FPA saturates at 65,000 counts, by using a 0.3 optical density neutral density (ND) filter the detector saturates at 300 $\mu W/(cm^2\ sr\ cm^{-1})$. For plume temperatures around 1000 K, the DC component of the interferogram represents 28 % of the dynamic range, with the interferometer producing an 8 % modulation at ZPD. With a 2.0 ND filter, the plume radiance at 2900 K is 1000 $\mu W/(cm^2\ sr\ cm^{-1})$ where the ratio of the DC component to center burst is 72 %.

High-speed visible, infrared broadband imagery and non-imaging FTIR spectroscopy augmented the results obtained from IFTS. Broadband imagery without

spectral resolution from both the MWIR IFTS InSb array and the visible camera provided information on the structure and fluid dynamics of the evolved plumes. Temporal averaging of 1.2 x 10^6 frames over 120 s produced steady images that defined the spatial extent and structure of the combustion products. From high-speed visible imagery, the plume velocity was estimated at framing rates of 350 Hz. The temporal dependence of the non-imaged FTIR spectrometer allowed identifying the LWIR bands of molecular species at high spectral resolutions of 0.25 cm^{-1}. Thus allowing identifying complex molecular species in the plume from laser irradiated polymeric materials.

The use of near-IR fiber lasers are of growing interest on laser lethality, where only a few experiments have been dedicated to investigate laser-materials interaction at a wavelength of 1.07 μm. Polymer targets have characteristically poor absorption in this region. Because of this, pigments are commonly added to acrylic thermoplastics (i.e. PMMA) for absorption in the near-IR. Laser lethality experiments were scaled at the near-IR laser radiation for polymer and graphite targets where experiments have been conducted with a 10.6 μm CW CO_2 laser [52, 71]. The oxidation kinetics is of particular interest with high energy lasers and elevated irradiances. Particularly, the temporal and spatial CO/CO_2 kinetics was studied for laser irradiated FRP, PMMA, and graphite targets. For laser heated graphite targets irradiated at 0.8 kW/cm^2, the results were consistent with the kinetics interplay between heterogeneous and homogeneous reactions, where surface reactions increases the surface flux of CO thus oxidizing along the boundary layer to produce CO_2, similar to a double film structure [75]. Moreover, at 4 kW/cm^2, the shear flow is radically changed due to a large flux of CO, CO_2 and carbon

particulates from the surface. From optical pyrometry, surface temperature was exceeded above the carbon sublimation temperature of 4000 K [134-136]. It is likely that surface sublimation of carbon dominates the plume dynamics above 4000 K.

As part of an effort to develop IFTS for laser lethality application, we began with this study of buoyant flow above FRP, PMMA, and porous graphite surfaces. Thus setting the foundation to understand the fundamentals mechanism of laser irradiated targets, primarily from spectral observations. These results allowed setting the foundation for future experiments aimed to close the gap between the empirical lethality databases and fundamental modeling. The kinetics of combustion above graphite samples in M = 0.1 - 0.9 laminar flows is of particular interest to both the combustion and laser communities, where well established kinetics models exists. Future work will be focused on investigating the combustion kinetics in laminar flows to merge experiments with detailed reactive fluid dynamics simulations.

Key Results

This research effort has demonstrated the ability to monitor the boundary layer plume of laser irradiated targets from imaging FTIR at spatial resolutions as high as 0.52 mm^2 per pixel. We reported the first spatial maps of plume temperature and column densities profiles at the surface-boundary layer from laser irradiated fiberglass reinforced polymer, PMMA, and porous graphite targets. These were extracted from fitting the observed spectra using a simplified radiative transfer model. Overall the use of a single-

layer plume model to retrieve species column densities proved to be an adequate approximation.

Fiberglass Reinforced Polymers

A first quantitative analysis of emissive plumes from laser-irradiated fiberglass composite surfaces was developed from fast framing hyperspectral observations. We identified H_2O, CO, CO_2, and hydrocarbon species in the gas phase from their characteristic FTIR spectral signatures. Time dependent, spatial maps of gas temperature and column densities were developed from a simplified radiative transfer model. The temporal evolution of temperature and column density demonstrated the feasibility of using IFTS to study the combustion kinetics interplay between CO and CO_2 spatially throughout laser irradiation. Our observations were consistent with prior FTIR fiberglass study [24] where initial larger concentrations CO_2 were somewhat larger than CO. A detailed evaluation of pyrolysis kinetics is complicated due to the chemical structure of the epoxy fiberglass composite. The mechanisms controlling the gas plume from these laser irradiated surfaces are unclear and require further analysis.

Poly(Methyl Methacrylate)

The thermal degradation of carbon black pigmented PMMA irradiated in air with a 1.06 μm Nd:YAG laser was investigated quantitatively from imaging and non-imaging FTIR spectroscopy. With the use of IFTS, we developed the first two-dimensional spatial maps of temperature and MMA concentrations from emissive plumes in the boundary layer. Based on the characteristic FTIR spectra in the gas phase plume, the primary decomposition product was MMA. Moreover, the non-imaged LWIR FTIR

spectrum of the plume was analyzed semi-quantitatively to identify the presence of other molecular species in the plume. However, the band-integrated radiance for the C-O stretching at 1159 and 1202 cm^{-1} shows considerable exponential growth. By plotting the other spectral bands as a function of the 811 cm^{-1} integrated radiance, the C-O stretching at 1159 and 1202 cm^{-1} seem to have an additional kinetic influence as oppose to the other features which are linear. The linear bands indicate the same emitter, whereas a nonlinear feature reflects another emitter contributing to the signal. Based on our observations, it appears that methyl pyruvate is present as a product of thermal decomposition of PMMA in air. This is consistent with prior studies reporting the presence of methyl pyruvate when PMMA is thermally decomposed in air [70, 117, 119]. However, the currently available spectral databases are rather limited and insufficient for our spectral fitting to model complex hydrocarbon molecular species.

Imaging FTIR also proved to be an efficient tool to investigate surface temperature distributions both temporally and spatially with low statistical errors. The spatial temperature distribution allowed visualizing the laser footprint that is important for laser lethality experiments. A simplified analysis on the laser heating process permitted understanding the difference between the surface heating rates for irradiated PMMA with a 10.6 μm and 1.06 μm laser. The predictions agreed with the experimental data where the initial heating rate is dominated by absorption of incident radiation, and then when the surface temperature reaches a steady state, conduction within the solid occurred [52]. The use of near-IR fiber lasers are of growing interest within the laser

lethality community, where only a few experiments have been dedicated to investigate polymer degradation at this wavelength.

An effective activation energy of 30.83 ± 8.29 kJ/mol was obtained for a pixel at the surface at surface temperatures between 455 - 600 K. This low activation energy is rather consistent with surface desorption of the monomer. Therefore at the 21.7 W/cm^2 irradiance, vaporization and desorption kinetics describe the rate of production of MMA at the surface.

Graphite

Plume characteristics from high-speed infrared and visible imagery as a function of laser irradiance (0.2 - 4 kW/cm^2) were documented for porous graphite targets. The degree of bending was correlated with broadband infrared imagery, where at higher irradiances the plume extended farther away from the surface in the x-direction and later bending in the y-direction by buoyancy. The lower the irradiance, the faster the plume bends closer to the surface. Furthermore, for laser irradiated graphite at 4 kW/cm^2, the plume fluid dynamics was remarkable since surface temperature exceeded the carbon sublimation temperature of 4000 K [134-136]. The moment flux from the surface appears comparable or larger than the than the buoyant atmospheric flow. It is likely that surface sublimation of carbon dominates the plume dynamics.

At irradiances of 0.8 kW/cm^2, the combustion plume characteristics in a buoyant flow were documented using high-speed visible imagery. A steady diffuse combustion plume was observed at steady-state 6mm away from the surface, also a secondary jet flame was also seen at 2 mm from the surface. Apparently, micro-cracks in the porous

graphite occasionally develop, ejecting burning particulates into the gas plume. The ability to monitor the evolved combustion plume from high-speed imagery allowed to elucidate the plume dynamics, however detailed reactive fluid dynamics interpretation as a function of laser irradiances was outside the scope of this work and will be subject to future experiment.

Furthermore a quantitative analysis was made from hyperspectral imaging FTIR for porous irradiated graphite at 0.8 kW/cm^2. At surface temperatures as high as 2500 K, the heterogeneous reaction corresponded to the primary combustion products of CO and CO_2, at the surface-boundary layer (x = 0.72 mm). The CO, CO_2 and plume temperature profiles along the boundary layer driven by buoyancy were consistent with Chelliah et al. [88] numerical simulations of porous graphite, where surface reactions increases the surface flux of CO thus oxidizing along the boundary layer to produce CO_2, similar to a porous graphite double film structure [75].

Summary

Preliminary results (Appendix A) served as proof of concept to show the ability to monitor the evolving, spatial distribution of the state of the surface-gas-boundary layer interface from laser irradiated targets. For the first time, a qualitatively analysis of gas phase combustion plumes above the surface of laser irradiated fiberglass composites was shown, from fast framing hyperspectral imagery observations. Painted and unpainted fiberglass reinforced polymers were irradiated with a 1.06 μm Nd:YAG laser. Spectral emission of CO, CO_2, and HC species were identified in the gas phase. High-speed

imagery was obtained using a low-pass filter for the interferograms, illustrating significant turbulent behavior during laser irradiation. Spatial brightness temperature maps exceeded 600 K, showing variation in the ratio of $[CO_2]/[CO]$ thus indicating interplay between heterogeneous and homogeneous kinetics. Based on these observations a quantitative analysis of unpainted fiberglass was done to develop spatial molecular concentration and temperature maps.

A first quantitative analysis of emissive plumes from laser irradiated fiberglass composite surfaces was developed from fast framing hyperspectral observations in chapter III. A single-layer radiative transfer model was developed for the spectral region from 2000 to 2400 cm^{-1} to estimate spatial maps of temperature and column densities of CO and CO_2 from the hyperspectral imagery. The spectral model was used to compute the absorption cross sections of CO and CO_2 using spectral line parameters from the high temperature extension of the HITRAN. An empirical emissivity was included in the model near 2100 cm^{-1} where it was tentatively attributed to a triple carbon bond hydrocarbon emission. This hydrocarbon spectral feature is not included in the HITRAN database and appears to be the most likely contribution to a minor CO P- branch asymmetry. Without the addition of this empirical modification, the fit RMSE is 1.35 greater than with the empirical emissivity. Spatial maps of gas temperature and CO and CO_2 column densities were developed for a single hyperspectral cube (t = 24 s) with low statistical error bounds. Also, the temporal evolution of temperature and column densities for a single pixel partially illustrates the evolving plume. The dynamic range of the IFTS instrument is limited by the DC component and modulation depth, so both pre-

combustion and post combustion images could not be obtained with the same instrument settings. Our observations were consistent with a prior FTIR fiberglass study [24] where initial larger concentrations CO_2 are somewhat larger than CO.

The thermal degradation of laser-irradiated black PMMA in air irradiated with a 1.06 μm Nd:YAG laser was investigated quantitatively from infrared spectroscopy in chapter IV. With the use of IFTS, the first two-dimensional spatial maps of temperature and MMA column density from emissive plumes in the boundary layer were developed. Based on the characteristic FTIR spectra in the gas phase plume, the primary decomposition product was the monomer MMA. A simplified radiative transfer model was used to extract spatial maps of temperature and MMA column density. However the spectral database for radiative transfer modeling of complex hydrocarbon spectra is rather limited and insufficient for our spectral fitting. The experimental absorption coefficient of MMA used in our model was measured by Wakatsuki [121] at atmospheric pressure with an MCT FTIR spectrometer at 1 cm^{-1} spectral resolution. This database is a combination of experimentally measured, interpolated and extrapolated spectra for the temperature range of 300 - 1400 K in increments of 50 K. Moreover, the use of a homogeneous plume radiative transfer model to extract column densities and temperature provided to be an adequate approximation. Imaging-FTIR also proved to be an efficient tool to investigate surface temperature distributions both temporally and spatially with low statistical errors. An effective activation energy of 30.83 ± 8.29 kJ/mol was obtained for a pixel at the surface at surface temperatures between 455 - 600 K. This low activation energy is rather consistent with surface desorption of the monomer. Therefore

at the 21.7 W/cm^2 irradiance, vaporization and desorption kinetics describe the rate of production of MMA at the surface. Effective activation energies in the plume correspond to degradation initiated by random scission [67, 69], which suggested formation of methyl pyruvate, from the reaction of MMA molecules with air. This demonstrates the ability of IFTS to extract activation energies at discrete positions in space.

The combustion mechanisms for laser irradiated graphite targets were investigated experimentally from hyperspectral imaging Fourier transform spectroscopy (IFTS) in chapter V. Porous graphite targets were irradiated using a 1.06 μm 20-kW ytterbium fiber laser. Plume dynamics are shown from high-speed imagery for power densities of 0.3 to 4 kW/cm^2. Emissive plumes from the oxidation of graphite in air at 0.8 kW/cm^2 were monitored using a mid-wave infrared imaging Fourier-transform spectrometer with high spatial resolution of 0.52 mm^2 per pixel. The evaluation of high gas temperatures (T > 2000 K) remains a challenge for radiative transfer modeling, particularly for CO_2, where spectral databases are rather limited. The HITEMP databank contains line-by-line parameters for a few molecules (H_2O, CO_2, CO, NO, and OH) that are of particular interest in combustion. An addition to an empirical emissivity to compensating for the CO_2 4.3 μm band was necessary for the HITEMP database at T > 2500 K. In order to validate the addition of this empirical emissivity at high temperatures for the LBLRTM, we have selected from the literature [143] an observed spectrum of the 4.3 μm CO_2 band at 2850 K and simulated the experimental high-temperature CO_2 spectral emissivity. In summary HITEMP underestimated the observed spectra, however the addition of an empirical emissivity improved the quality of the fit.

The use of statistical narrow-band models (EM2C and RADCAL) was validated with experimental combustion data at temperatures as high as 2900 K. Systematic errors associated with the spectral models between LBLRTM, RADCAL and EM2C were discussed. Based on the quality of the fit, LBLRTM and RADCAL had the best residuals.

At surface temperatures as high as 2500 K the heterogeneous reaction corresponded to the primary combustion products of CO and CO_2, as observed at the surface-boundary layer (0.72 mm). Towards the boundary layer CO conversion to CO_2 was observed thus agreeing with the global homogeneous reaction of Howard et al. [96]. Overall, the obtained results were consistent with the kinetics interplay between heterogeneous and homogeneous reactions, where surface reactions increases the surface flux of CO thus oxidizing along the boundary layer to produce CO_2

Recommendations for Future Work

Although a simplify, single-layer plume radiative transfer model resulted to be an adequate approximation a temperature gradient is known to exist along the instrument line of sight. A multi-layer plume model would be computational intensive, but is expected to result in much better approximation. Spatial information obtained from side-view experiments supplemented with front view experiments will help define the multi-layer framework.

Accuracy of radiative transfer modeling depends on the available spectral databases. Evaluation of combustion species at elevated gas temperatures of T > 2500 K

remains challenging, particularly for CO_2, where spectral databases are rather limited. Also, there is a lack of adequate experimental infrared measurements for these combustion gases at very high temperatures, mainly for CO_2. An optional empirical emissivity was necessary to improve the quality of the fit at T > 2500 K, where HITEMP underestimates the band wings of the 4.3 μm fundamental asymmetric CO_2 band [106-108, 141]. There is a need for more accurate spectral databases for the combustion community. Implementation of the CDSD-4000 database was not studied in our work, and it will be recommended to use this database in future combustion work. Current LBLRTM is limited to model combustion data up to 3000 K due to limitation on the total internal partition sum (TIPS) [144, 145]. This is an important consideration at high irradiances, where plume temperature may reach temperatures as high as 4000 K.

Thermal degradation of polymers gives rise to hydrocarbon species, where spectral databases are also limited. We overcome this limitation by the addition of an empirical emissivity. However, in order to account accurately for this hydrocarbon species, there is a need to have a database of hydrocarbon species at high temperatures. With laser irradiated PMMA experiments we were able to incorporate MMA experimental, interpolated and extrapolated absorption coefficient database in our radiative transfer model, previously developed by Wakatsuki [121].

The next set of experiments will be focused on the combustion kinetics of laser irradiated graphite in a laminar flow, where well established fluid dynamics models exist [78, 79, 87-89]. From preliminary testing in a wind tunnel, Appendix B summarizes some of the lessons learned, aimed to improve the next set of experiments. A minimum

spectral resolution of 2 cm^{-1} is required to detect the CO ro-vibrational band from the TELOPS, based on buoyant flow experiments. On preliminary experiments, strong spectral emission of CO_2 was observed. However, spectral emission of CO was not evident at the 8 cm^{-1} spectral resolution. We encounter difficulty focusing the instrument with the wind tunnel set-up at a distance of 37 cm. Further investigation on the instrument point spread function and a method on focusing the instrument will be important in the next set of experiments. Another consideration is the design of the sample holder, preferable this will be made of ceramic or a material that can resist temperatures as high as 4000 K. The boundary layer plume in a wind tunnel set-up is much thinner than the one obtained in the buoyant flow experiments, which could limit the spatial resolution that is required for fluid dynamics modeling, those are much smaller than the obtained instrument spatial resolutions of ~ 0.52 mm^2 per pixel. Appendix B summarizes the wind tunnel experiments of laser irradiated graphite and a brief qualitatively discussion on some preliminary results.

Appendix A. Mid Infrared Imaging Fourier Transform Spectromtery for High Power Fiber Laser Irradiated Fiberglass Composites (Invited Paper)

Preface

New measurement techniques to study continuous wave (cw) laser-material interactions are emerging with the ability to monitor the evolving, spatial distribution of the state of the surface-gas boundary layer. A qualitative analysis of gas phase combustion plumes above the surface of laser irradiated fiberglass composites is developed from fast framing hyperspectral imagery observations. An imaging Fourier Transform Spectrometer (IFTS) operating in the mid-infrared (MWIR) with high framing rate has recently been developed at the Air Force Institute of Technology (AFIT) in collaboration with Telops Inc. A 320 x 256 indium antimonide (InSb) focal plane array with spectral response from 1.5 – 5.5 μm is mated with a Michelson interferometer to achieve spectral resolutions as high as 0.25 cm^{-1}. The very fast 16-tap InSb array frames at 1.9 kHz for the full 320 x 256 frame size. The single pixel field of view of 0.3 mrad provides a spatial resolution of 1 mm at the minimum focal distance of 3 m. Painted and unpainted fiberglass composites are irradiated with a 1064 nm cw Nd:YAG laser for 60 s at 100 W in air at atmospheric pressure. Selective emission in the region of 2100 - 3200 cm^{-1} is readily evident and is used to develop a time-dependent spatial map of both temperature and plume constituents. The time evolution of gas phase combustion products such as CO and CO_2 molecules are monitored, with a spectral resolution of 2 cm^{-1}. High-speed imagery is obtained using a low-pass filter for the interferograms, illustrating significant turbulent behavior during laser irradiation. Spatial brightness

temperature maps exceed 600 K. Spatial variation in the ratio of $[CO_2]/[CO]$ indicates an interplay between heterogeneous and homogeneous kinetics.

Introduction

Laser ablation of materials in an oxidizing environment and under the influence of air flow is a complex process defined by the interplay of a number of processes, such as oxidation, vaporization, melting, expulsion of molten material, and breakdown/removal of oxide layer [1-3]. There has been relatively limited computational efforts aimed at investigation of the enhancement of material removal by external gas flow, the effect of the oxidation of metal targets on the efficiency of laser cutting, and the characteristics of the material recession under conditions of laser-induced charring of polymer composites and carbon-rich targets. Often the fundamental analyses must be limited to a few key processes and global, predictive modeling is difficult.

Fewer studies have been performed on the combustion products of composite materials, such as fiberglass reinforced polymers (FRP) [24, 40]. Fiberglass is primarily composed approximately of 50% by weight of silica (SiO_2) with other inorganic and trace components as shown in Table 1 [41]. Fiberglass composite materials may contain sizings, binders or flame retardants as well to organics components [42]. FRP have a complex chemical structure as discussed by Kinsella et al. [24], and Ishida et al. [43] Moreover this type of composite material is generally composed of adhesive joints with many components [43] and multiple interfaces, typically epoxy or polyester based polymers [24, 40].

The combustion characteristic of polyester-based fiberglass composite materials has been described by Landrock [44] as burning with a smoky flame, accompanied by melting, dripping and some char formation. Combustion products of polyester-based materials have been reviewed elsewhere [45-47], containing organic components such as C_6H_6 (benzene), $(C_6H_5)_2$ (biphenyl), $C_6H_5CH_2CH_3$ (ethyl benzene), C_5H_8 (pentadiene), $C_6H_5CH{=}CH_2$ (styrene), and CH_3 (toluene). It has been reported that these composite materials have a flash-ignition temperature of approximately 648 K (375 ^oC) and a self-ignition temperature of approximately 758 K (485 ^oC) [40, 44].

The US Environmental Protection Agency (EPA) investigated the combustion products of commercial boating and building fiberglass samples [40]. Elemental analysis of these samples before combustion showed that the ratio of carbon (C) composition is approximately 47 percent for the building/boating fiberglass samples, with less than 2 percent of trace elements such as aluminum (Al), cadmium (Cd), chromium (Cr), and magnesium (Mg) [40]. During experiments, the EPA reported an average of 129 and 284 ppm of CO for the boating and building industry fiberglass respectively. A propane burner contributes a sizeable and somewhat variable CO_2 emission, however its concentration was reported to be an averaged of 2650 and 4300 ppm for both the boating and building fiberglass, respectively [40].

Kinsella et al. [24] applied a radiant flux to study the combustion of silicone-, melamine-, and epoxy-fiberglass composites by focusing a 600 W tungsten-halogen lamp over a 25 mm diameter area. These materials are used in the construction of aircrafts, boats, and military vehicles. Some visible physical observation on the surface of these

fiberglass composites during irradiation are bubbling, charring, out-gassing, laminate separation, and spontaneous ignition. The combustion of these three fiberglass samples was monitored by non-imaging Fourier transform infrared spectroscopy (FTS) and the products evolving above the surface in the gas phase were identified with its corresponding spectra. Despite the different chemical composition between each sample, the evolution of gaseous CO, CO_2, H_2O and CH_2O (formaldehyde) were consistent as combustion byproducts with dissimilar HC effluents. Most of the FRP combustion products are classified as toxic effluents consequently its spectral identification plays an important role for several applications as its early detection [24, 40, 49, 50].

Imaging FTS (IFTS) has the potential to measure both spatial and temporal variations in brightness temperature, chemical species concentrations, and spectral identification of effluents at high resolutions and fast framing rates [4, 5]. Combustion events are often turbulent systems with stochastic temperature fluctuations in the plume. Some of the benefits of hyperspectral imagery for examining combustion events are: (1) turbulence in plume dynamics can be studied from high-speed broadband imagery contained in the interferogram cubes, (2) narrow instantaneous field-of-view (IFOV) simplifying spatial averaging as well the spectral interpretation for large variations in the temperature and density of combustion plumes, and (3) construction of two-dimensional dynamics of the evolve species in the gas phase to predict the chemical kinetics interplay in a dynamic flow revealing plume symmetry [12].

Gross et al. have demonstrated that IFTS have been used to study the plume of hot exhaust from jet engines [13], detonation fireballs [8, 9], and industrial smokestack [16]. For the jet engine experiments the obtained resulted was averaged to reduce scene-change artifacts for interpreting CO, and CO_2 spectral emission [13]. These scene fluctuations can be further analyzed by taking advantage of the DC-coupled interferograms to extract turbulence flow information [12] which is an advantage to non-imaging FTS. IFTS achieved high resolution spectra of industrial smokestack at standoff distances with 1 to 8 percent error between *in situ* and remotely estimated SO_2 and CO_2 volume mixing fractions [16]. With previous work illustrating some of the capabilities of this instrument, there is significant potential for studying combustion of composite materials during laser irradiation.

In this work, we present the first qualitative midwave (3-5.5 μm) IFTS measurement of laser induced combustion plume from fiberglass composite materials. After identifying gas phase emitters from their spectral signatures, spatial brightness temperatures map of CO and CO_2 are developed to illustrate combustion kinetics of painted and unpainted FRP.

Experimental

Instrument Description

The IFTS uses a 320 x 256 pixel Stirling-cooled InSb focal plane array (FPA) with spectral response ranging from 1800 to 6667 cm^{-1} (1.5-5.5 μm). The individual

pixel field of view is 0.326 mrad, yielding spatial resolution of ~ 1 mm at the minimum focal length of 3 m. A series of modulated intensity images corresponding to optical path differences are collected on the FPA, forming an interferogram at each pixel. Fourier transformation of each pixel's interferogram produces a raw ultra-spectral image. The raw spectrum is then calibrated at each pixel with two internal wide-area blackbody sources at 313 and 293 K (40 and 20 ^{o}C) [19]. The maximum optical path difference (MOPD) describes the unapodized spectral resolution. For the present study, the integration time for each frame is 20 μs and the spectral resolution was 2 cm^{-1}. A hyper-spectral data cube is comprised of a three-dimensional (3D) image of 32 pixels x 32 pixels x 9480 frames. Additional instrument details can be found in the literature [4, 5].

Experimental Set-Up

A schematic diagram illustrating the experimental set-up is shown in Figure 50. Unpainted and painted fiberglass composites samples (2.54 cm x 2.54 cm) were irradiated with a 1064 nm CW Nd:YAG laser at 100 W for 60 s in air at atmospheric pressure. The IFTS monitored the continuous plume emission above the surface of the fiberglass sample, at a focal distance of approximately 3.1 m (Figure 50a). Test samples were positioned normal to the incident laser energy with an irradiance of 45 W/cm^2. A cold blackbody plate was located at the instrument FOV perpendicular to the combustion plume for emission measurements (Figure 50b).

Painted (Figure 51a) and unpainted (Figure 51b) fiberglass composites samples are shown before and after the 60 s laser radiation for visual comparison. Figure 51c illustrates the physical responses of the tested fiberglass material to the laser energy throughout an assortment of time intervals during experimentation.

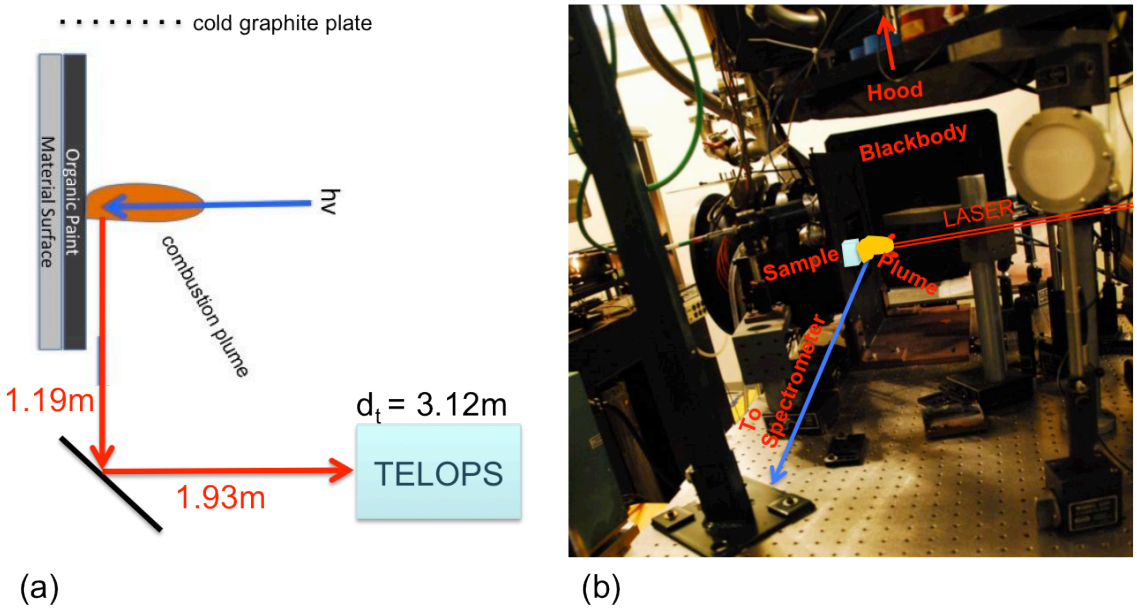

Figure 50. (a) Top view for schematic diagram of the experiment set-up with the IFTS perpendicular to the combustion plume for the laser irradiation event. (b) Photo of the actual testing set-up with the sample normal to the laser energy and a cold blackbody plate positioned at the instrument FOV perpendicular to the combustion plume.

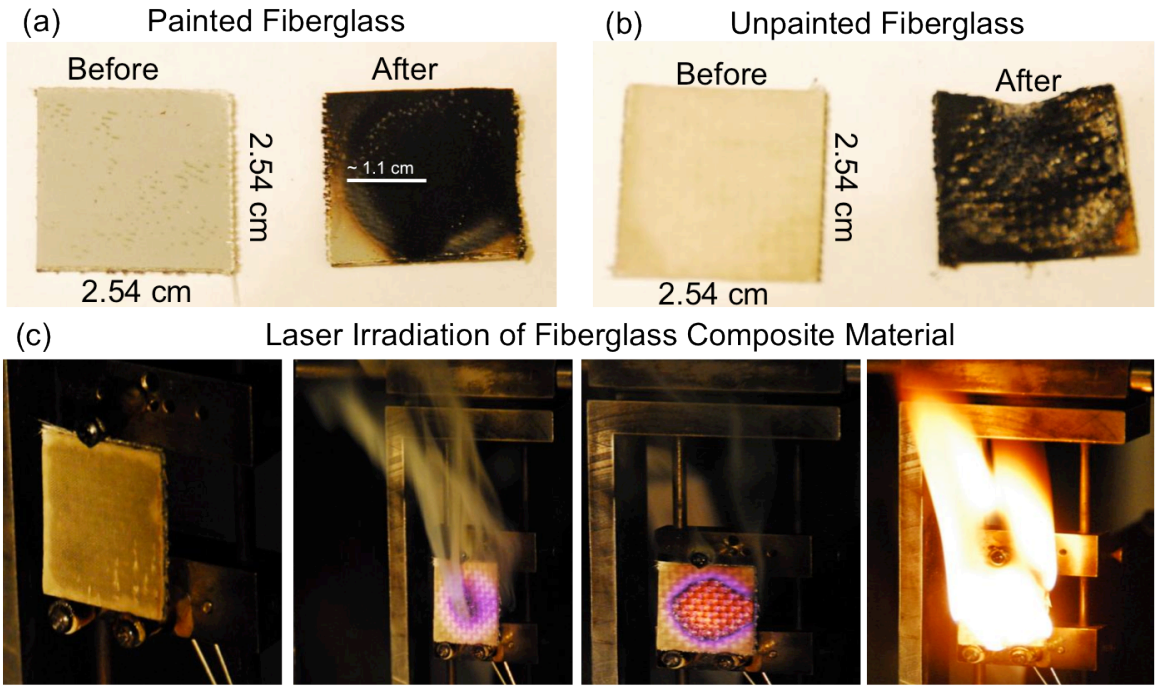

Figure 51. (a) Painted and (b) unpainted fiberglass composite samples before and after 60 s laser radiation. (c) From left to right, still photos of distinctive material response to the laser radiation throughout different time intervals during experimentation.

Results and Discussion

Painted and unpainted fiberglass composite samples exhibited visual differences on its surface with char formation following experimentation. From Figure 51a it appears that the exposed charred fibers were not as prominent as in irradiated unpainted fiberglass sample (Figure 51b). Char formation during polymer degradation with heat, directly affects the degree of flame retardancy of the polymeric material. Van Krevelen [152] observed that the intrinsic flammability of any polymer reduces as it char-forming tendency increases, since char always formed at the expense of volatile fuel. According

to Kandola et al. [153] the correlation between increased char formation and flame resistance is threefold. First, char formation occurs through cross linking reactions, reducing the quantity of volatile pyrolysis fragments; second, char acts as insulator, that separates the virgin polymer from the heat of the flame; and third, a charred surface impedes the outward flow of combustible gases produced from the degradation of the underlying unburnt material. Considering these factors, the addition of a surface-active intumescent system will act as an insulator for the underlying material structure. These are usually in the form of paints on the surface of polymers or metal structures. Difference between painted and unpainted fiberglass samples after irradiation can be elucidated from the above mentioned factors that the paint at the surface acted as an insulator for the underlying fiberglass material. Moreover the intumescent or paint will fill inter-fiber spacing as it chars, and when in contact with the charring fiberglass, it will interact with the adjacent fibers if compatible liquified phases are present during the initial pyrolysis or combustion [153].

Several material responses were observed during the 60 s laser irradiation of both unpainted and painted fiberglass composite surfaces. Throughout experimentation the FRPs burned with a smoky flame, accompanied by visible changes in colors until it self-ignited, followed by a steady combustion flame and char formation at the surface as shown in Figure 51c. These are the typical combustion characteristic of polyester-based fiberglass materials [44].

The top left panel of Figure 52 presents the raw hyperspectral image (32 x 32 pixels) for a single frame of the unpainted fiberglass composite material, accompanied by

the raw Fourier transform infrared (FTIR) spectrum (top right panel) of pixel (15,26). The plume direction is caused by the flow of the fume hood (Figure 50b) and its structure is clearly evident from the raw hyperspectral image of the unpainted (top left) and painted (bottom left) fiberglass composites during laser irradiation. The difference between painted and unpainted fiberglass plume structure is clearly evident. The painted surface heated much rapidly consequently outgassing very quickly with turbulent behavior in the MWIR, not evident in the unpainted material. The rapid heat on the painted sample can be explained from Kandola et al. [153] observations that melted paint will combined with the interfiber void as it chars, then combining with adjacent fibers, giving rise to unique fibrous char-reinforced intumescent structure with enhanced mechanical properties. Self-ignition for the fiberglass composites proceeded at different rates with the painted material combusting ahead. The spectral imagery reveals information related to fluid dynamics, and a detailed examination of this will be subject to future work.

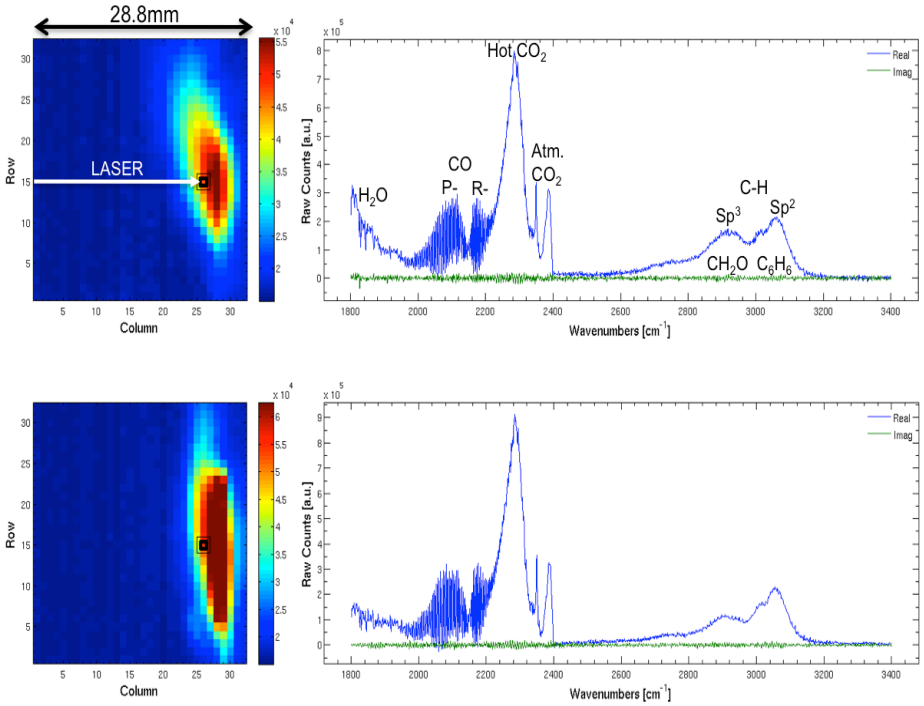

Figure 52. Top panel: Unpainted fiberglass composite raw hyperspectral image (32 x 32 pixels) of a single frame (left). (Right) Corresponding raw FTIR spectrum of pixel (15,26) from the top left image. Bottom Panel: Painted fiberglass composite raw hyperspectral (32 x 32 pixels) image of a single frame (left). (Right) Corresponding raw FTIR spectrum of pixel (15,26) from the bottom left image. The raw FTIR spectrum is for a single pixel (row, column) of a hyperspectral data cube. The brightest pixels are saturated in this image.

Unpainted and painted fiberglass raw FTIR spectrum reveals several diatomic, and polyatomic specie. These molecules can be readily identified by their corresponding ro-vibrational spectra for pixel (15,26). The imaginary component of the spectrum, shown in green, provides an estimate of the noise level of the instrument. The signal contained in the real part and noise is equitable distributed among the real and imaginary parts. From the real part of the spectrum is readily evident the spectral signature of gaseous H_2O, CO, CO_2, CH_2O and C_6H_6 molecules as combustion products of the fiberglass composite material. The absorption features of atmospheric H_2O ($1800 < \nu < 2000$ cm^{-1}) and CO_2 ($2320 < \nu < 2400$ cm^{-1}) are present. Perhaps the most easily recognizable spectral features are the P- and R- branch emission lines between 2000 cm^{-1} and 2220 cm^{-1} arising from the fundamental CO ro-vibrational transitions. Lines P(1) – P(41) beginning at 2143 cm^{-1} and decreasing with frequency at nearly equally spaced intervals are observed. Similarly, lines R(0) – R(26) beginning at 2152 cm^{-1} and increasing nearly uniformly spaced intervals are also observed. Much of the CO lines in the R- branch can be seen riding on the CO_2 continuum in the 2160 to 2240 cm^{-1} region. The R- branch of the CO fundamental band, which lies closet to the CO_2 $\nu 3$ band, is strongly overlapped by the hot CO_2 spectrum, but the P- branch suffers little CO_2 interference [98].

The most prominent spectral features arise from the rotational structure associated with transitions between various CO_2 levels. The narrow emission line at 2386 cm^{-1} arises from the asymmetric stretching mode, however most emission lines associated to this rotational structure are subsequently absorbed by atmospheric CO_2 along the line-of-

sight. Combustion plume temperatures are relatively high and increase the population of higher energy rotational levels, consequently causing emission outside this opaque region. Likewise, emission is observed on the low wavenumber edge of this opaque region for the same reason, as well with various thermally accessible ro-vibrational states, becoming available at elevated plume temperatures. The pattern of strong CO_2 emission on each side of the same atmospheric CO_2 absorption spectra is found on many combustion plumes [24, 40, 98]. This large emission features are often referred as the red (longer wavelength) and blue (shorter wavelength) spike or hot CO_2 bands [99] at 2285 and 2288 cm^{-1} respectively.

The presence of hydrocarbon (HC) is also recognized in the fiberglass composite plume spectrum, and their respective emission bands are identified between 2800 to 3200 cm^{-1}. For alkenes the C-H emission features of stretching modes occurs for sp^2 and sp^3 orbital above and below 3000 cm^{-1} respectively. According to Kinsella et al. [24] CH_2O spectral emission appear as a HC combustion product of melamine-, epoxy-, and silicone-fiberglass between 2750 - 3000 cm^{-1}. Poljansek et al. [154] reported that the C-H stretch and C-H bend overtone for CH_2O appeared respectively at 2980 and 2914 cm^{-1}. Furthermore C_6H_6 emission was only evident with the silicone-fiberglass between 3000 – 3200 cm^{-1}. Benzene has been associated as a combustion product of polyester-based fiberglass [44], silicone is typically used as a polyester resin, which explains its emission on combusting silicone-fiberglass. Furthermore, the isomeric benzene structures were identified by Anderson et al. [155] and assigned its corresponding FTIR spectra. Most

benzene isomers have emission peaks above 3000 cm^{-1} corresponding to sp^2 C-H stretching.

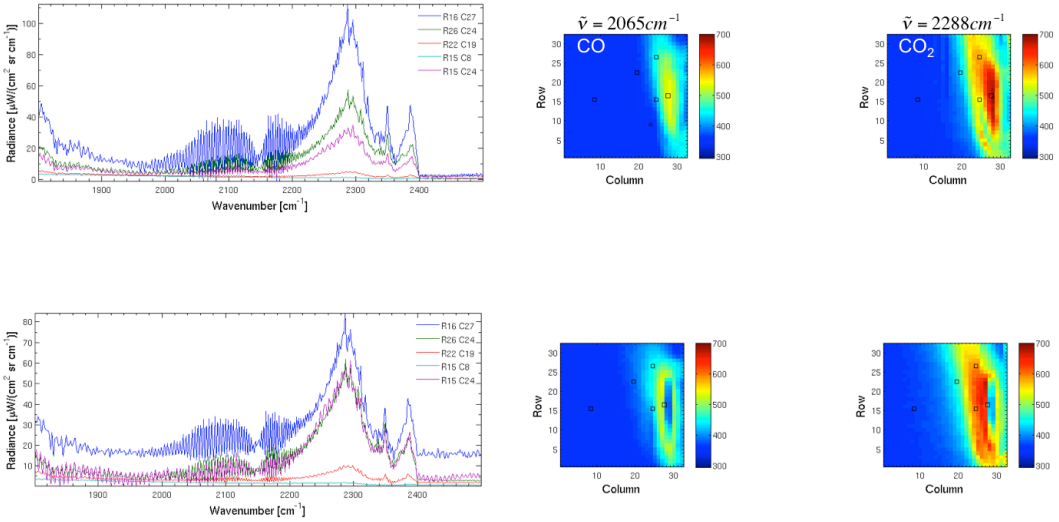

Figure 53. Average calibrated FTIR CO and CO_2 spectra of unpainted (top left panel) and painted fiberglass (bottom left panel) for a choice of pixels. Time average brightness temperatures maps of CO at 2065 cm^{-1} and CO_2 at 2288 cm^{-1} for unpainted (top right panel) and painted (bottom right panel) fiberglass.

Radiometric calibration was accomplished using two on-board blackbodies set at 313 and 293 K (40 and 20 ^{o}C). Calibrated to radiance units [$\mu W/(cm^2\ sr\ cm^{-1})$], the CO and CO_2 FTIR spectra of unpainted and painted fiberglass are plotted for pixels: (16,27), (26,24), (22,19), (15,8), (15,24) in Figure 53 top and bottom left panels. Spatial brightness temperature maps of CO at ν=2065 cm^{-1} and CO_2 at ν=2288 cm^{-1} are shown in Figure 53 for unpainted and painted material. These brightness temperature maps represent the temperature a perfect blackbody in thermal equilibrium would have to be with its surrounding to duplicate the observed intensity at a specific wavenumber. The brightness temperature maps are time averages for the entire 60 s event. Temperatures exceeding 600 K are evident spatially for CO_2 and evidently hotter than CO, the painted material exhibit cold temperatures throughout combinations of pixel rows 11-22 and columns 28-29. These regions are saturation in the detector and subsequently gave rising to unphysical brightness temperature measurements.

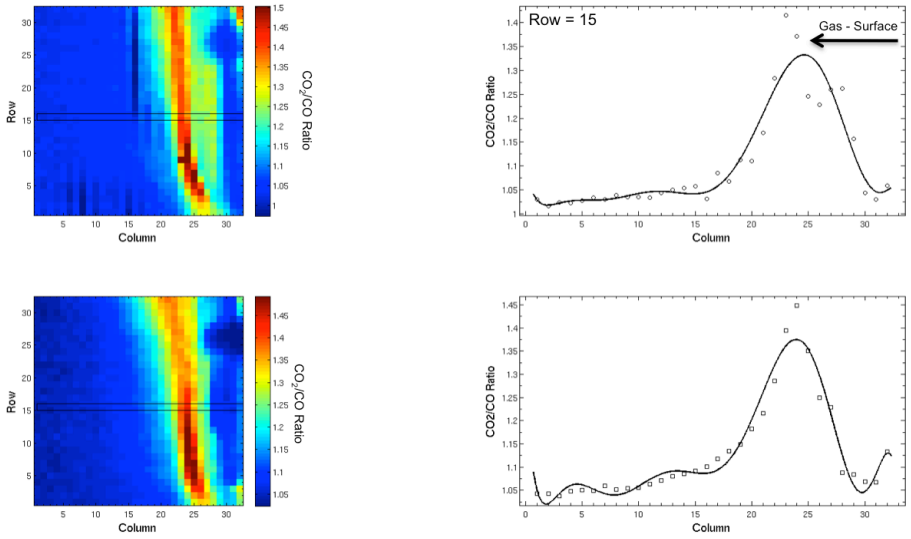

Figure 54. Ratio of CO_2/CO spatial brightness temperature maps for unpainted (top left panel) and painted (bottom left panel) fiberglass composite. Plot of the CO_2/CO ratio along all columns of row 15 for unpainted (top right panel) and painted (bottom right panel) fiberglass.

Spatial brightness temperature map are proportional to species concentration. As an initial step we investigate the combustion kinetics of CO and CO_2 from their brightness temperature ratios. From Figure 54 the concentration of CO_2 is higher at the combustion plume above the surface, spatially the material surface is above column 31 with decreasing column numbers shifting away from surface boundary to the gas phase plume. Once the fiberglass composite self-ignited, its combustion flame was so intense that saturated most pixels closed to the surface, approximately around columns 30-32.

However we can still study the species kinetics above the surface and the relationship between them. These first qualitative observations will lead to the development of radiative transfer models for species quantification, detail interpretation of plume emissivity and temperatures in future work.

Conclusions

A qualitative analysis of gas phase combustion plumes above the surface of laser irradiated fiberglass composites were developed from fast framing hyperspectral imagery observations. The painted and unpainted fiberglass composites studied exhibited variations in response to the 45 W cm^{-2} laser irradiance. The FRPs burned with a smoky flame, accompanied by visible changes in colors until it self-ignited, followed by a steady combustion flame and char formation, which are the combustion characteristic of polyester-fiberglass. Based on characteristic FTIR spectra of effluents in the plume, we readily identified H_2O, CO, CO_2, CH_2O, and C_6H_6 as combustion products of the fiberglass composites. Based on literature survey on the FTIR emission spectrum of these HC, we can confidently associate the FTIR emission spectra between 2840 – 3000 cm^{-1} to CH_2O and 3000 – 3200 cm^{-1} to C_6H_6 as combusting products of the painted and unpainted fiberglass composites. Spatial brightness temperatures exceeding 600 K showing variation in the ratio of $[CO_2]/[CO]$ indicated interplay between heterogeneous and homogeneous kinetics. Based on these observations spatial concentration and temperature maps is feasible for future work.

Appendix B. Preliminary Experiments of Laser Irradiated Graphite in an Oxidizer Flow of M = 0.2

Introduction

As part of an effort to develop IFTS for laser lethality application, we began with previous experiments in a buoyant flow above FRP, PMMA, and porous graphite surfaces. Allowing setting the foundation for future experiments aimed to close the gap between the empirical lethality databases and fundamental modeling with predictive capabilities. The kinetics of combustion above graphite samples in M = 0.1 - 0.9 laminar flows is of particular interest to both the combustion and laser communities, where well established kinetics models exists [87, 88, 150]. Preliminary results in an oxidizer flow of M = 0.2 are discussed below, to investigate the instrument performance and allow for better planning of a robust set of experiments. Future work focus on investigating the combustion kinetics in laminar flows to merge experiments with detailed reactive fluid dynamics simulations.

Preliminary Results

Figure 55 shows a schematic diagram for the experimental set-up. The imaging FTIR (TELOPS) was focused 37 cm from the sample edge and perpendicular to the surface. A mirror was placed above the graphite target surface, since the laser beam was coming in an angle above the TELOPS, to irradiated the graphite surface. Also, other instruments were used to complement the data acquisition from the imaging FTIR. A

non imaging FTIR (BOMEM) was focused at 3.13 m. High speed infrared (FLIR) and visible cameras (Phantom), were also used as seen from Figure 55.

For this testing, we looked at three different porous graphite with particle sizes of 0.6 cm, 0.15 cm, and 0.001 cm. The graphite targets were square samples with a size of 58.06 cm^2 and 1.27 cm thickness. The laser beam diameter was ~ 4.44 cm and the targets were irradiated for 120 s with peak irradiances between 0.22 and 2.1 kW/cm^2. The imaging FTIR FPA was narrowed to a window size of 256 x 50 pixels. Integration time was set to 50 μs per frame and a spectral resolution of 8 cm^{-1}. The oxidizer was air with a flow of M = 0.2, for a duration of 120 s. Table 8 summarizes the test matrix for the wind tunnel experiments.

Table 8. Test matrix for wind tunnel experiments

Porosity	Peak Irradiance	TELOPS ND filter
0.6 cm	0.2 – 1.1 kW/cm^2	0.3, 1.0
0.125 cm	0.8 – 2.1 kW/cm^2	1.0, 1.45
0.001 cm	0.8 kW/cm^2	0.3, 0.6, 1.0

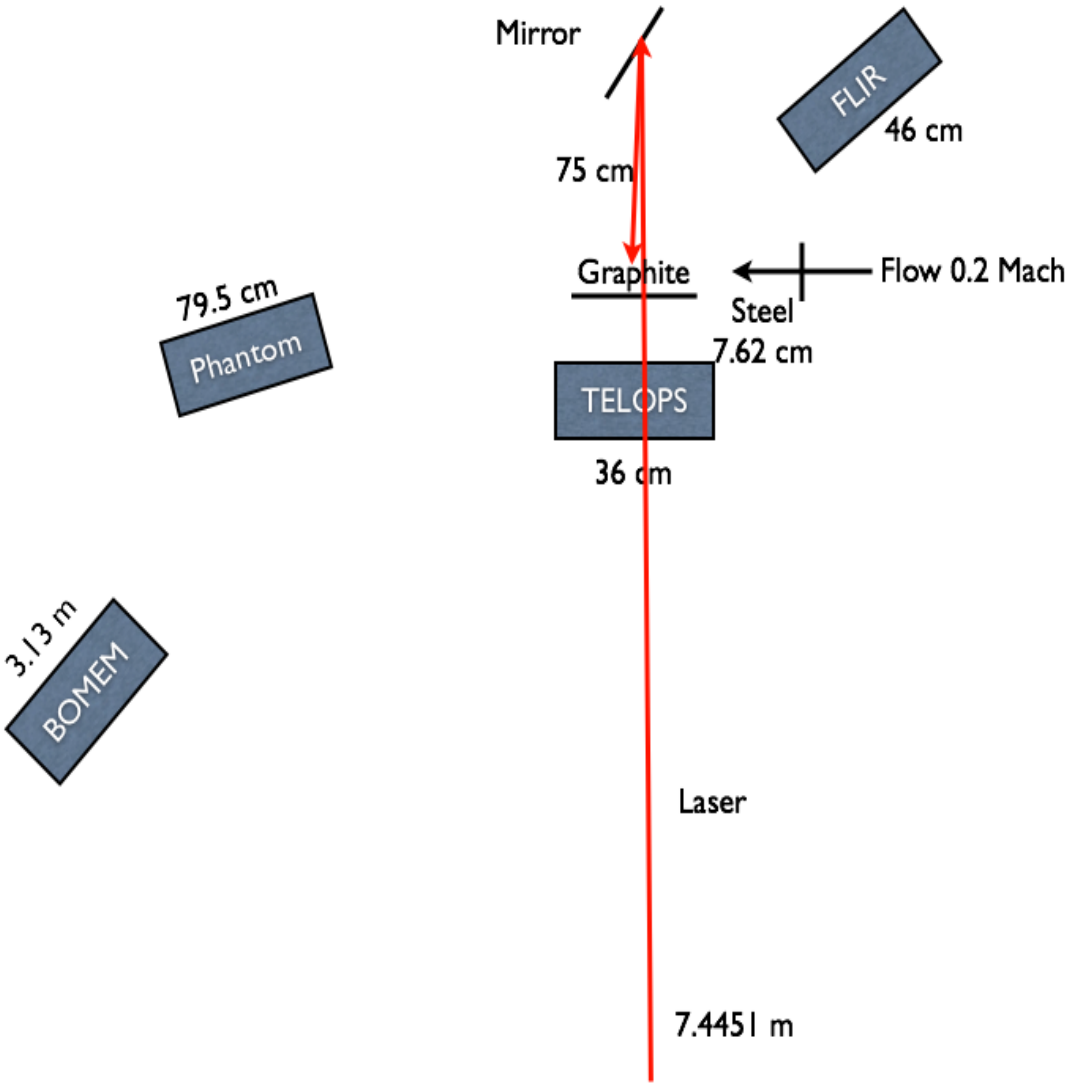

Figure 55. Experimental set-up schematic diagram

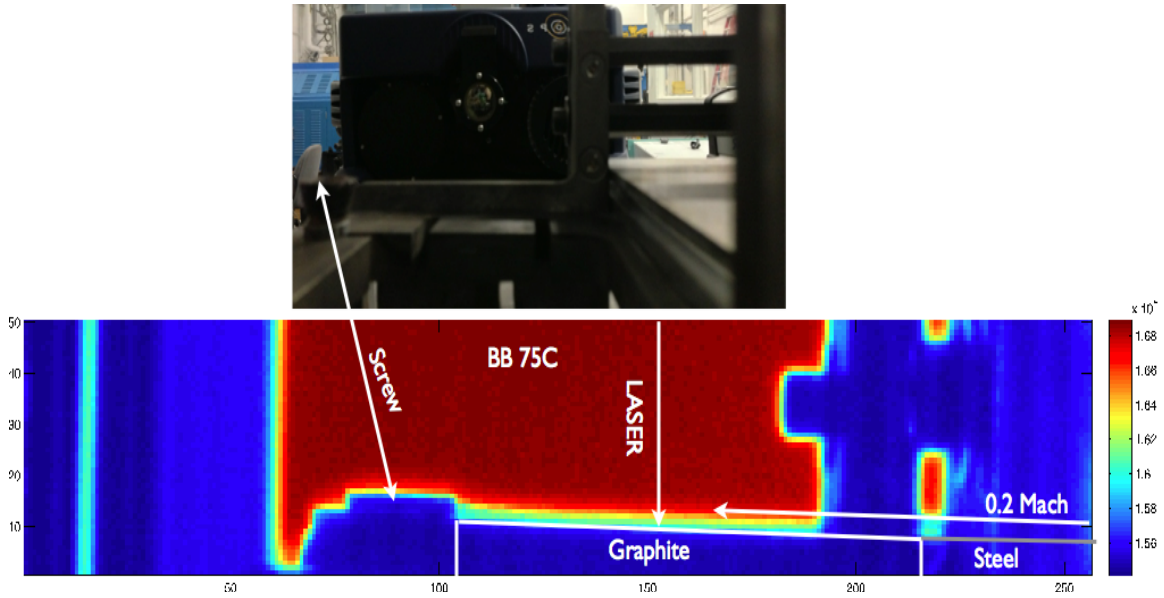

Figure 56. Broadband imagery with hot black body in background

Figure 56 is the infrared broadband image with a warm black body in background to point out the experimental set-up from the TELOPS camera view. The sample holder was made of steel, a set of screws were at the end of the graphite target to hold the sample in place while the wind tunnel was on. To further understand the intensity variation from the broadband imagery, Figure 57 look at the change of intensity as a function of rows for three different columns.

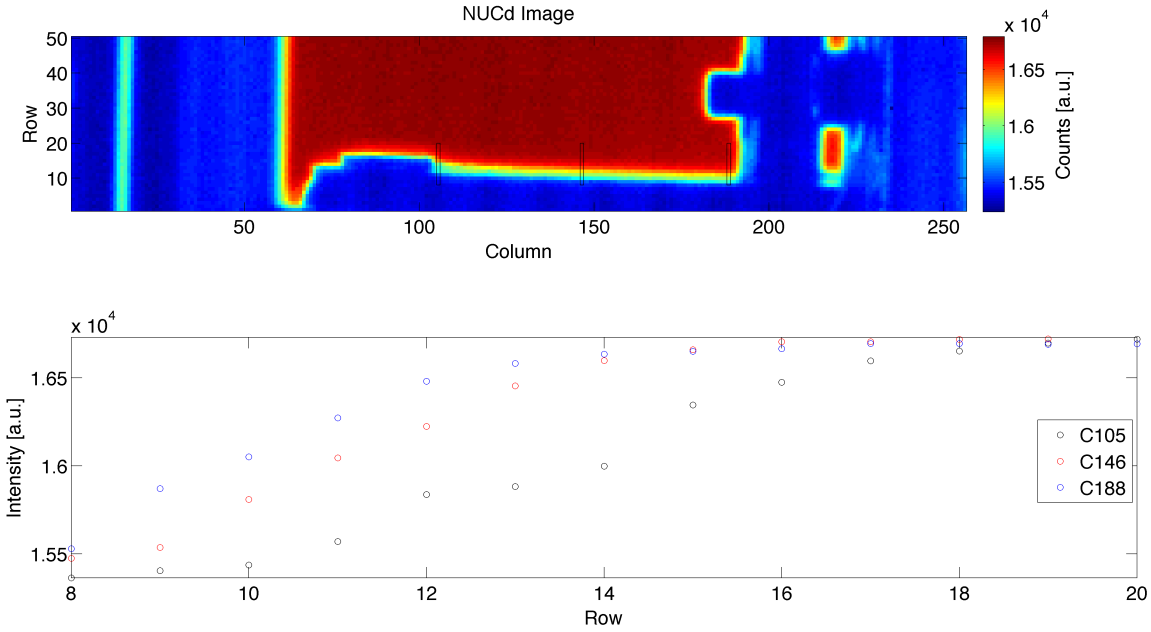

Figure 57. Non-uniformity corrected (NUCd) intensity variation of an un-processed hyperspectral image at a frame for three different columns (C).

For columns (C) 105, 146 and 188, the intensity variation for a hyperspectral image at a single frame is plotted as a function of rows in Figure 57. At C105, the intensity rise much slower that at columns 146 and 188 respectively. Columns 146 and 188 reaches the same intensity value at row 14, where for column 105 it takes 10 pixels to reach same values. This intensity variation tells us that there exists a slight tilt with the instrument camera. Also, a rough idea of the instrument point spread function (PSF) can be obtained from the qualitatively analysis. By shifting column 105 intensity by 2 rows (adding two rows) and column 146 by 1 row, it is seen from Figure 58 that the PSF is approximately 2 row pixels (y-direction).

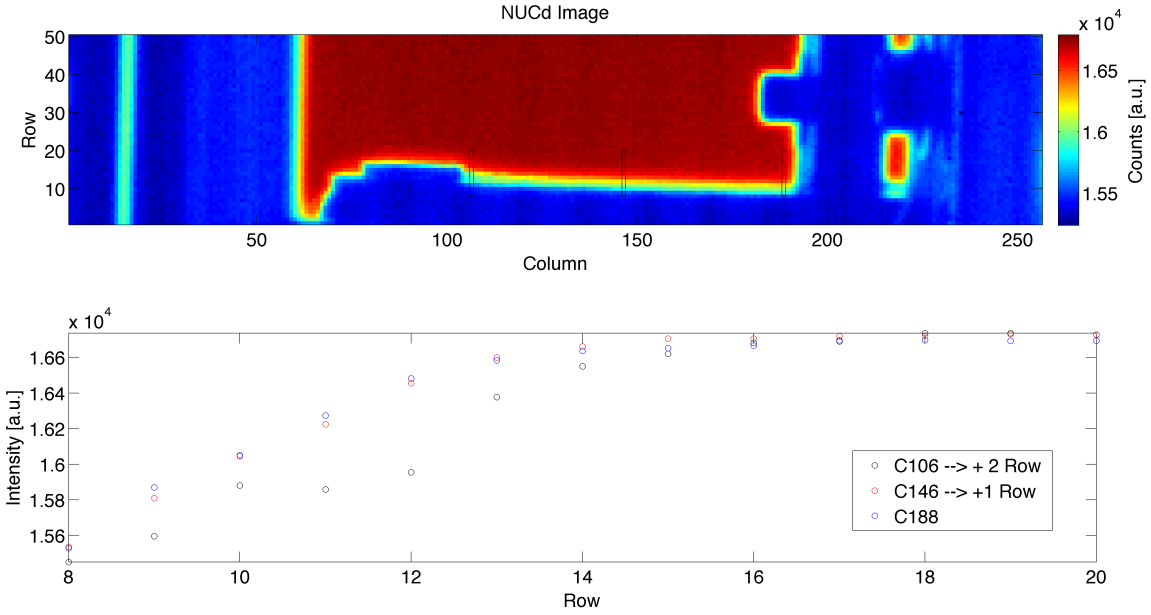

Figure 58. Intensity variation by shifting columns 105 and 146 by 2 and 1 rows respectively.

By looking at the intensity variation as a function of columns for rows 29, 34 and 39 in Figure 59, the PSF along the x-driection (columns) can be roughly estimated. As seen from Figure 59 the intensity variation along the columns is less dramatic than for the rows (Figure 57).

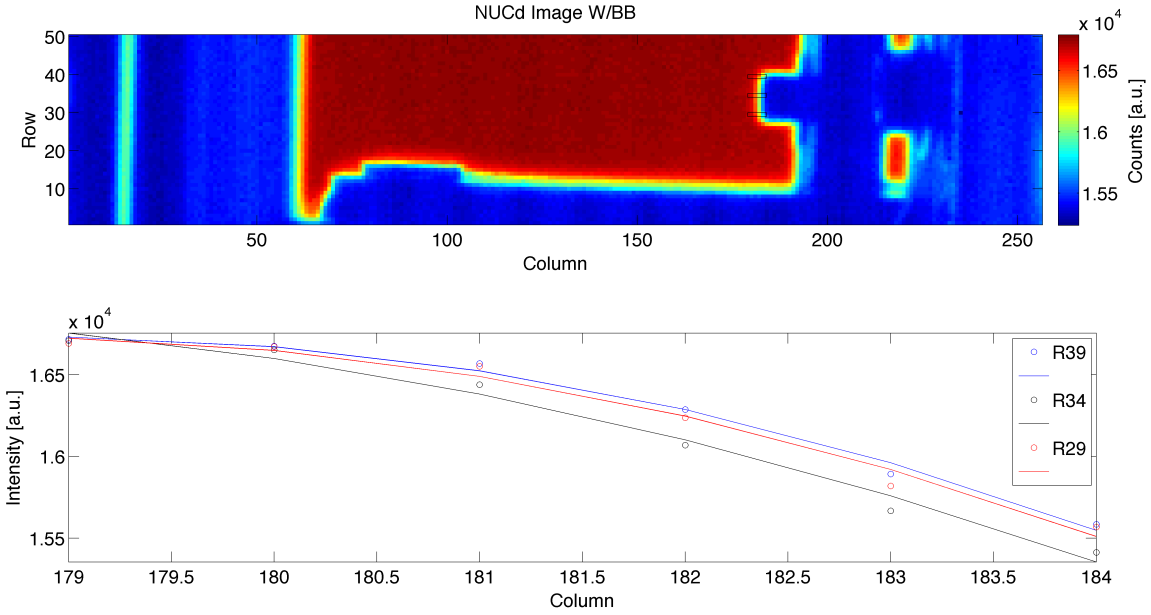

Figure 59. Intensity variation for broadband imagery as a function of columns for rows 29, 34 and 39.

Spectral Signal

The time averaged spectral data (excluding saturated data) for columns 105, 146 and 188 (top to bottom) for laser irradiated porous graphite (0.15 cm particle size) at 0.8 kW/cm^2 is shown in Figure 60. At the spectral resolution of 8 cm^{-1}, strong emission of CO_2 is evident from the spectral signature. However, the CO P- and R- branches are not evident at this spectral resolution. The spectral signature is strongest at column 105, where at columns close to the nozzle (146 and 188) the CO_2 emission becomes weaker. From the imagery, the boundary layer plume appears much thinner and closer to the surface than the one evolved in a buoyant flow (Figure 38).

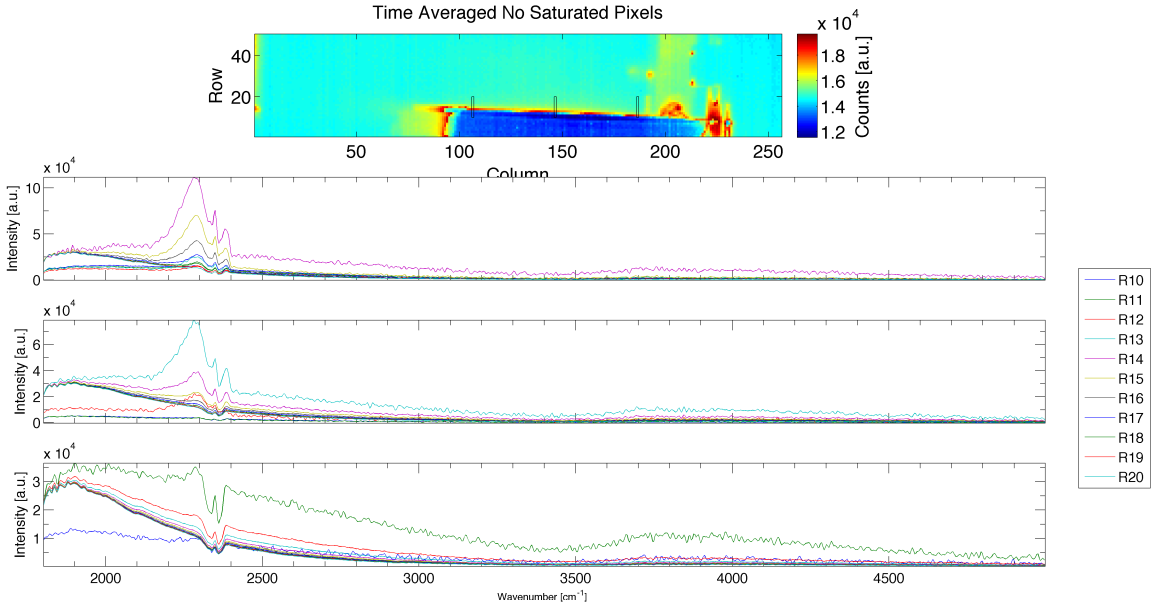

Figure 60. Time averaged broadband image and spectral signature for rows along columns 105, 146 and 188 for laser irradiated graphite (0.12 cm particle size) at 0.8 kW/cm^2.

The spatially averaged spectrum for the end of the sample (rectangular box) is shown in Figure 61. Strong spectral emission of CO_2 was obtained at the end of the boundary layer towards the oxidizing stream. Also no CO spectral signature was evident. These time and spatially averaging increases the signal to noise. However, when plotting the un-calibrated spectra for an individual data cube at t = 39 s for rows along column 106, the spectral appears in Figure 62 very noisy and with oscillations along the wings of the spectra. These oscillations could be due to turbulence at the boundary layer plume.

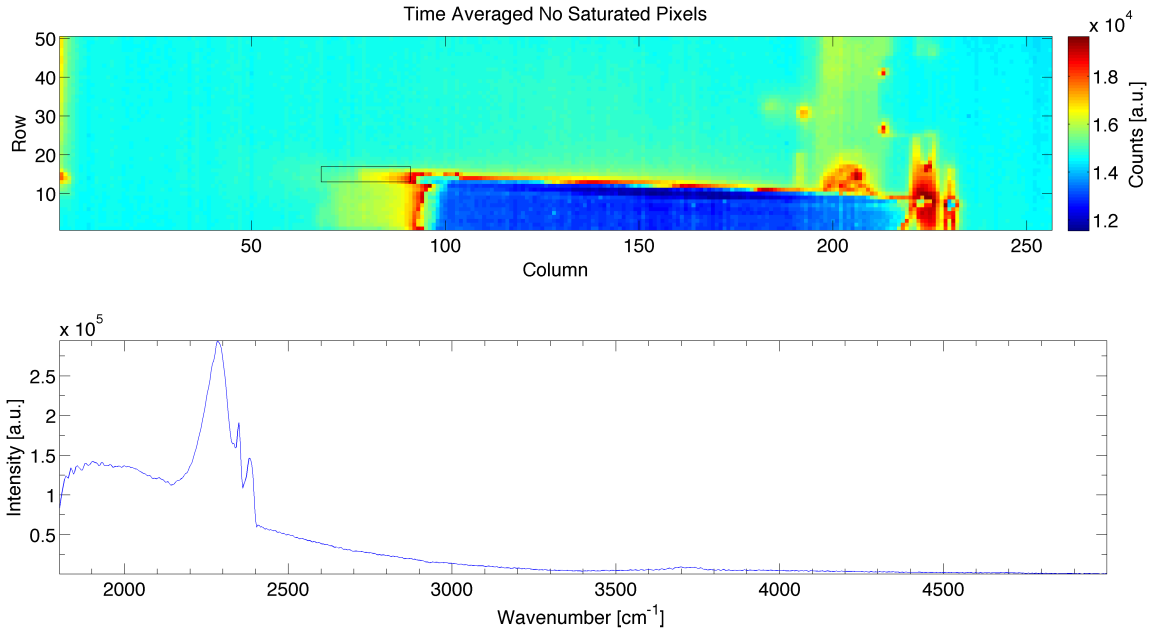

Figure 61. Time and spatially averaged spectra at the edge of the sample towards the oxidizer stream flow.

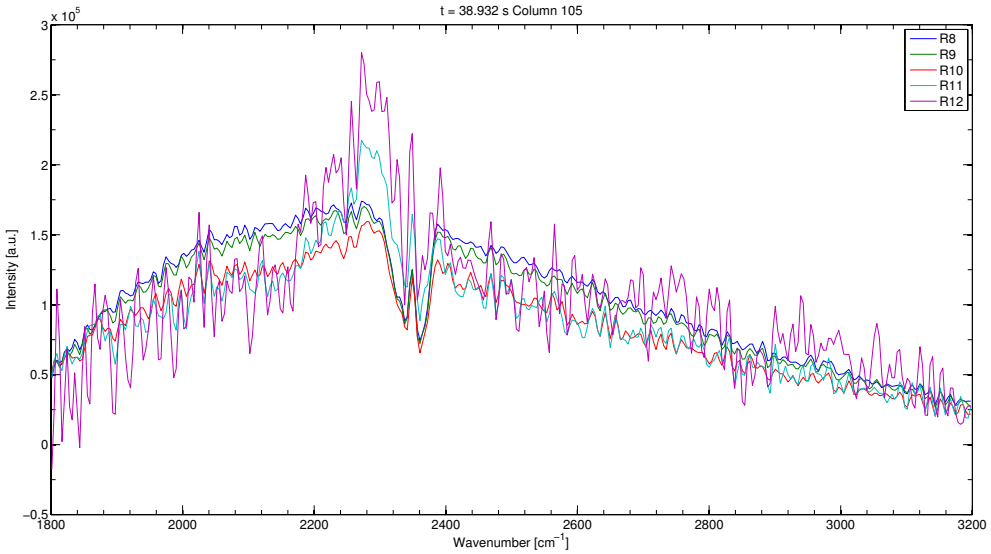

Figure 62. Un-calibrated spectra at t = 39 s for rows (8 – 12) along column 106.

The peak intensity of the CO_2 band at 2195 cm^{-1} was plotted as a function of time in Figure 63 for rows 11 to 16 along columns 105, 146 and 188 (from top to bottom after the broadband image). At column 188 there is CO_2 signal at row 11, where the intensity increases between 10 s $\leq$ t $\leq$ 15 s. At t > 15 s the intensity decreases and goes to zero, this is indicative of saturation in the signal using a 1.45 ND filter. At column 146 the CO_2 signal at row 11 is much more intense and appears to have the same increase and decrease rate as column 188. Much farther away in the oxidizer flow in column 105, the spectral CO_2 signal appears to not saturate until much later in time (t ~ 70 s). Also it appears that CO_2 spectral signature can be detected at other pixels as oppose with columns 146 and 188.

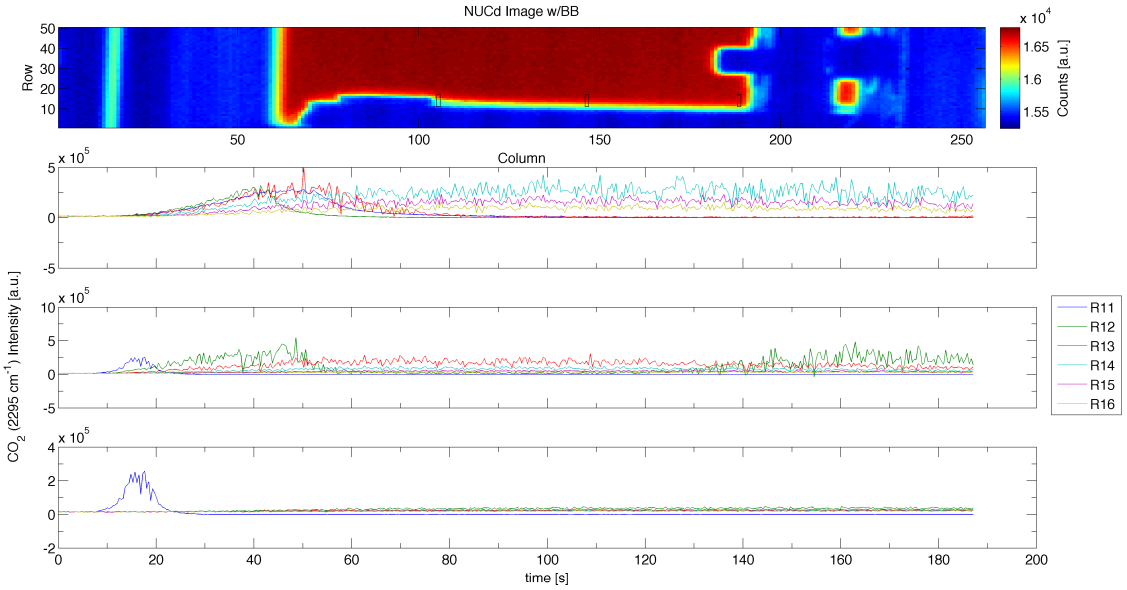

Figure 63. Peak CO_2 intensity at 2195 cm^{-1} for rows (11- 16) along columns 105, 146 and 188.

Conclusions

From this first set of experiments a lot was learned with the imaging FTIR instrument performance to improve the next set of experiments. First of all a better design for a sample holder and nozzle has to be consider prior engaging in the next experiment. It will be important to investigate beforehand the PSF. Based on the preliminary data it appears that there could be problem with focusing the instrument, that could have made difficult to detect CO. Based on buoyant flow experiments, a minimum spectral resolution of 2 cm^{-1} should be used to detect the CO P and R branches. The next test matrix should also investigate what the optimal ND filter will be to not saturated the detector. Even with a 1.45 ND filter data saturated very rapidly as oppose to using a 2.0 ND filter in the buoyant flow experiments. Averaging the data both spatially and temporally increases the signal to noise. This has to be taken into account with the temporally resolved data processing. The boundary layer plume appears much thinner and smaller at the wind tunnel than at a buoyant flow (Figure 34). The experimental results will be limited to the instrument spatial resolution on how many pixels could be interpreted at the surface-boundary layer. Future experiments will be aimed to elucidate the combustion kinetics of laser irradiated graphite in an oxidizer flow to anchor with fluid dynamics kinetics modeling.

Recommendations for Future Work

An important consideration is the design of the sample holder and nozzle. Based on previous experiments in laser heated graphite in buoyant flow, we melted several

sample holders due to the high surface temperatures of the graphite samples. It is recommended to have an insulated material such as ceramic that can withstand temperatures as high as 4000 K. Due to the thin boundary layer plume, a high spatial resolution will be required. The IFTS minimum focal distance with the 0.25X telescope is 35 cm, yielding spatial resolutions of 0.29 mm^2/pixel. It will be important to investigate the instrument point spread function as well to develop a systematic focusing method prior the next set of wind tunnel experiments. Another important consideration is the limitation with the line-by-line radiative transfer model. At gas temperatures above 2500 K, spectral modeling of the observed combustion gases becomes challenging due to underestimation of the band wings of the 4.3 μm fundamental asymmetric CO_2 band and/or overestimation of the CO_2 spectral radiance from the currently available spectral databases [106-108, 141]. Also, the radiative transfer mode suffer limitation on the total internal partition sum (TIPS) up to 3000 K [144, 145]. It is recommended to investigate the implementation of the CDSD-4000 spectral database, since the CO_2 absorption cross section has been developed up to 5000 K. However, this will require the extrapolation of the CO absorption cross section for temperatures above 3000 K. It is recommended to supplement the IFTS measurements with high-speed framing infrared and visible cameras as well with non-imaged FTIR instruments.

Bibliography

1. Darke, S. A. and J. F. Tyson. "Interaction of laser radiation with solid materials and its significance to analytical spectrometry. A review," *Journal of Analytical Atomic Spectrometry,* 8 (2): 145-209 (1993).

2. Perram, G. P., S. J. Cusumano, R. L. Hengehold and S. T. Fiorino. *An introduction to laser weapon systems*. Albuquerque, NM: Directed Energy Professional Society, 2010.

3. Radziemski, L. J. and D. A. Cremers. *Physics of laser-induced breakdown: An update*. New York, NY: CRC, 1989.

4. Chamberland, M., V. Farley, A. Vallieres, A. Villemaire, L. Belhumeur, J. Giroux and J.-F. Legault. "*High-performance field-portable imaging radiometric spectrometer technology for hyperspectral imaging applications*," Proc. SPIE. 5994: 59940N-59911 (2005).

5. Farley, V., C. Belzile, M. Chamberland, J.-F. Legault and K. R. Schwantes. "*Development and testing of a hyperspectral imaging instrument for field spectroscopy*," Proc. SPIE. 5546: 29-36 (2004).

6. Lewis, E. N., P. J. Treado, R. C. Reeder, G. M. Story, A. E. Dowrey, C. Marcott and I. W. Levin. "Fourier transform spectroscopic imaging using an infrared focal-plane array detector," *Analytical Chemistry,* 67 (19): 3377-3381 (1995).

7. Pisani, M. Q. and M. E. Zucco. *Fourier transform based hyperspectral imaging*. Rijeka, Croatia: InTech, 2011.

8. Gross, K. C., J. Wayman and G. P. Perram. "*Phenomenological fireball model for remote identification of high-explosives*," Proc. SPIE. 6566: 656613-656612 (2007).

9. Gordon, J. M., K. C. Gross and G. P. Perram. "*Temporally resolved infrared spectra from the detonation of advanced munitions*," Proc. SPIE. 7330: 733006-733008 (2009).

10. Gordon, J. M., K. C. Gross and G. P. Perram. "*Empirical model for the temporally resolved temperatures of post-detonation fireballs for aluminized high explosives*," Proc. SPIE. 8018: 80181M-80188 (2011).

11. Steward, B. J., K. C. Gross and G. P. Perram. "Reduction of optically observed artillery blast wave trajectories using low dimensionality models," *Proc. SPIE-Int. Soc. Opt. Eng.,* 8020: 80200D (2011).

12. Tremblay, P., K. C. Gross, V. Farley, M. Chamberland, A. Villemaire and G. P. Perram. "*Understanding and overcoming scene-change artifacts in imaging fourier-transform spectroscopy of turbulent jet engine exhaust*," Proc. SPIE. 7457: 74570F-74513 (2009).

13. Moore, E. A., K. C. Gross, S. J. Bowen, G. P. Perram, M. Chamberland, V. Farley, J.-P. Gagnon, P. Lagueux and A. Villemaire. "Characterizing and overcoming spectral artifacts in imaging fourier-transform spectroscopy of turbulent exhaust plumes," *Proc. SPIE-Int. Soc. Opt. Eng.,* 7304: 730416 (2009).

14. Bradley, K. C., K. C. Gross and G. P. Perram. "*Imaging fourier transform spectrometry of chemical plumes*," Proc. SPIE. 7304: 73040J-73011 (2009).

15. Bradley, K. C. *Midwave infrared imaging fourier transform spectrometry of combustion plumes*. PhD Dissertation. Air Force Institute of Technology (AU), Wright-Patterson AFB, OH, 2009.

16. Gross, K. C., K. C. Bradley and G. P. Perram. "Remote identification and quantification of industrial smokestack effluents via imaging fourier-transform spectroscopy," *Environmental Science & Technology,* 44 (24): 9390-9397 (2010).

17. Savary, S., J.-P. Gagnon, K. C. Gross, P. Tremblay, M. Chamberland and V. Farley. "Stadoff identification and quantification of flare emissions using infrared hyperspectral imaging," *Proc. SPIE-Int. Soc. Opt. Eng.,* 8024: 802040T (2011).

18. Rhoby, M. R., K. C. Gross and D. L. Blunck. *Application of an imaging fourier-transform spectrometer to determine two-dimensional scalar values in laminar flames*. Dayton, OH: Spring Technical Meeting of the Central States Section of the Combustion Institute, 2012.

19. Revercomb, H. E., H. Buijs, H. B. Howell, D. D. LaPorte, W. L. Smith and L. Sromovsky. "Radiometric calibration of ir fourier transform spectrometers: Solution to a problem with the high-resolution interferometer sounder," *Applied Optics,* 27 (15): 3210-3218 (1988).

20. Morley, N. J., et al. *High energy laser (hel) lethality data collection standards*. Albuquerque, NM: The Directed Energy Professional Society, 2007.

21. Boley, C. D., S. N. Fochs and A. M. Rubenchik. "Large-spot material interactions with a high-power solid-state laser beam," *J. Dir. Energy,* 3: 15-24 (2008).

22. Palm, W. J., M. A. Marciniak, G. P. Perram, K. C. Gross, W. F. Bailey and C. T. Walters. "Wavelength and temperature dependence of continuous-wave laser absorptance in kapton® thin films," *Optical Engineering,* 51 (12): 121802 (2012).

23. Hurst, B., M. A. Marciniak and G. P. Perram. *Laser-damage study of painted metals at 1.07μm*. Presentation at the Directed Energy Systems Symposium, Directed Energy Professional Society, March 2011, Monterey, California.

24. Kinsella, K., J. R. Markham, C. M. Nelson and T. R. Burkholder. "Thermal decomposition products of fiberglass composites: A fourier transform infrared analysis," *J. Fire Sci.,* 15 (2): 108-125 (1997).

25. Acosta, R. I., K. C. Gross, S. Johnson, L. Dao, D.Medina, R. Roybal, P. Black and G. P. Perram. "Gas phase plume from laser irradiated fiberglass reinforced polymers via imaging fourier-transform spectroscopy," *In Press Appl. Spectros.,* 68 (7): (2014).

26. Clough, S. A., M. W. Shephard, E. J. Mlawer, J. S. Delamere, M. J. Iacono, K. Cady-Pereira, S. Boukabara and P. D. Brown. "Atmospheric radiative transfer modeling: A summary of the aer codes," *J. Quant. Spectrosc. Radiat. Transf.,* 91: 233-244 (2005).

27. Alvarado, M. J., V. H. Payne, E. J. Mlawer, G. Uymin, M. W. Shephard, K. E. Cady-Pereira, J. S. Delamere and J.-L. Moncet. "Performance of the line-by-line radiative transfer model (lblrtm) for temperature, water vapor, and trace gas retrievals: Recent updates evaluated with iasi case studies," *Atmos. Chem. Phys.,* 13: 6687-6711 (2013).

28. Acosta, R. I., K. C. Gross and G. P. Perram. "Thermal degradation of poly(methyl methacrylate) with a 1.06 μm nd:Yag laser in a buoyant flow," *To be submitted to Polym. Degrad. Stab.*: (2014).

29. Acosta, R. I., K. C. Gross and G. P. Perram. "Boundary layer combustion kinetics of laser irradiated porous graphite from imaging fourier transform spectroscopy," *To be submitted to Combustion and Flame*: (2014).

30. Soufiani, A. and J. Taine. "High temperature gas radiative property parameters of statistical narrow-band models for h2o, co2, and correlated-k model for h2o and co2," *J. Heat Mass Transf.,* 40: 987-991 (1997).

31. Grosshandler, W. L. "Radiative heat transfer in nonhomogeneous gases: A simplified approach," *J. Heat Mass Transf.,* 23: 1147-1459 (1980).

32. Acosta, R., K. Gross and G. Perram. "*Mid-infrared imaging fourier transform spectrometry for high power fiber laser irradiated fiberglass composites*," Proc. SPIE. 8239: 82390R (2012).

33. Michelson, A. A. "Visibility of interference-fringes in the focus of a telescope," *Philos. Mag.,* 31: 256-259 (1891).

34. Michelson, A. A. "On the application of interference methods to spectroscopic measurements ii," *Philos. Mag.,* 34 (32): 280-299 (1892).

35. Michelson, A. A. *Light waves and their uses*. Chicago, IL: University of Chicago Press, 1961.

36. Griffiths, P. R. and J. A. de Haseth. *Fourier transform infrared spectrometry*. Hoboken, NJ: John Wiley & Sons, Inc., 2007.

37. Cooley, J. W. and J. W. Tukey. "An algorithm for the machine calculation of comlex fourier series," *Math. Comput.,* 19: 297-301 (1965).

38. Speitel, L. C. "Foruier transform infrared analysis of combustion gases," *J. Fire Sci.,* 20: 349-371 (2002).

39. Dunn, R. J. *Operational implications of laser weapons*. Falls Church, VA: Northrop Grumman Corporation, 2005.

40. Lutes, C. C. and J. V. Ryan. *Characterization of air emissions from the simulated open combustion of fiberglass materials. Final report, january 1992-august 1993*. Report number: EPA-600/R-93-239. Research triangle park, NC: EPA, 1993.

41. Donovan, R. P. *Fabric filtration for combustion sources*. New York, NY: Marcel Dekker Inc., 1985.

42. Skinner, H. C. W., M. Ross and C. Frondel. *Asbestos and other fibrous materials: Mineralogy, crystal chemistry, and health effects*. New York, NY, USA: Oxford University Press, USA, 1988.

43. Ishida, H. and J. L. Koenig. "An investigation of the coupling agent/matrix interface of fiberglass reinforced plastics by fourier transform infrared spectroscopy," *Journal of Polymer Science: Polymer Physics Edition,* 17 (4): 615-626 (1979).

44. Landrock, A. H. *Handbook of plastics flammability and combustion toxicology: Principles, materials, testing, safety, and smoke inhalation effects*. PARK RIDGE, NJ, USA: NOYES DATA CORP., 1983.

45. Gad, S. C., S. C. Gad and R. C. Anderson. *Combustion toxicology*. Boca Raton, FL: CRC Press, 1990.

46. Levin, B. C. "A summary of the nbs literature reviews on the chemical nature and toxicity of the pyrolysis and combustion products from seven plastics: Acrylonitrile–butadiene–styrenes (abs), nylons, polyesters, polyethylenes, polystyrenes, poly(vinyl chlorides) and rigid polyurethane foams," *Fire and Materials,* 11 (3): 143-157 (1987).

47. Braun, E. and B. C. Levin. "Polyesters: A review of the literature on products of combustion and toxicity," *Fire and Materials,* 10 (3-4): 107-123 (1986).

48. Smith, B. *Infrared spectral interpretation: A systematic approach*. Boca Raton, FL: CRC Press, 1999.

49. Bo, Z., J. H. Yan, X. D. Li, Y. Chi, K. F. Cen and B. G. Cheron. "Effects of oxygen and water vapor on volatile organic compounds decomposition using gliding arc gas discharge," *Plasma Chem. Plasma Process.,* 27: 546-558 (2007).

50. Sumi, K. and Y. Tsuchiya. "Toxicity of combustion products," *J. Combust. Toxicol.,* 2 (213-255): (1975).

51. Kashiwagi, T. "Experimental observation of radiative ignition mechanisms," *Combust. Flame,* 34: 231-244 (1979).

52. Kashiwagi, T. "Effect of sample orientation on radiative ignition," *Combust. Flame,* 44: 223-245 (1982).

53. Mutoh, N., T. Hirano and K. Akita. "Experimental study on radiative ignition of polymethylmethacrylate," *Proc. Combust. Inst.,* 17: 1183-1190 (1979).

54. Tsai, T.-H., M.-J. Li, I.-Y. Shih, R. Jih and S.-C. Wong. "Experimental and numerical study of autoignition and pilot ignition of pmma plates in a cone calorimeter," *Combust. Flame,* 124: 466-480 (2001).

55. Hertzberg, M. and I. A. Zlochower. "Devolatilization wave structures and temperatures for the pyrolisis of polymethylmethacrylate, ammonium, perchlorate, and coal at combustion level heat fluxes," *Combust. Flame,* 82: 15-37 (1991).

56. Kashiwagi, T. "Effects of attenuation of radiation on surface temperature for radiative ignition," *Combust. Sci. Technol.,* 20 (5-6): 225-234 (1979).

57. Lloyd, C. T. *Near-ir laser ablation of organic polymeric materials*. PhD George Mason University, Fairfax, VA, 2009.

58. Lloyd, C. T., R. F. Cozzens, C. J. Bright, J. D. Sames, L. K. Myers and P. D. Kazunas. "Ablative polymeric materials for near-infrared high energy laser beam diagnostics," *J. Dir. Energy,* 3 (3): 239-256 (2009).

59. Glauberman, G. Y., N. F. Pilipetskii, S. Y. Savanin, V. V. Shvedchenko and V. V. Shkunov. "Damage to polymer glasses caused by scanning with a cw laser beam," *Sov. J. Quantum Electron.,* 19 (6): 790-793 (1989).

60. Luche, J., T. Rogaume, F. Richard and E. Guillaume. "Characterization of thermal properties and analysis of combustion behavior of pmma in a cone calorimeter," *Fire Safety J.,* 46: 451-461 (2011).

61. Said-Galiev, E. E. and L. N. Nikitin. "Possibilities of laser modification of the surface of polymer composites," *Mech. Compos. Mater.,* 29 (2): 196-201 (1993).

62. Joeckle, R. C., G. Rapp and A. Sontag. "Boiling process in pmma irradiated by co2, df and hf laser radiations," *Proc SPIE,* 1397: 679-682 (1991).

63. Cozzens, R. F. and R. B. Fox. "Infrared laser ablation of polymers," *Polym. Eng. Sci.,* 18 (11): 900-904 (1978).

64. Pielichowski, K. and J. Njuguna. *Thermal degradation of polymeric materials*. Crewe, UK: Rapra Technology Limited, 2005.

65. Song, J., C.-H. Fischer and W. Schnable. "Thermal oxidative degradation of poly(methyl methacrylate)," *Polym. Degrad. Stab.,* 36: 261-266 (1992).

66. Hirata, T., T. Kashiwagi and J. E. Brown. "Thermal and oxidative degradation of poly(methyl methacrylate): Weight loss," *Macromolecules,* 18 (7): 1410-1418 (1985).

67. Peterson, J. D., S. Vyazovkin and C. A. Wight. "Kinetic study of stabilizng effect of oxygen on thermal degradation of poly(methyl methacrylate)," *J. Phys. Chem. B,* 103: 8087-8092 (1999).

68. Peterson, J. D., S. Vyazovkin and C. A. Wight. "Stabilizing effect of oxygen on thermal degradation of poly(methyl methacrylate)," *Macromol. Rapid Commun.,* 20: 480-483 (199).

69. Zeng, W. R., S. F. Li and W. K. Chow. "Review on chemical reactions of burning poly(methyl methacrylate) pmma," *J. Fire Sci.,* 20: 401-433 (2002).

70. Zeng, W. R., S. F. Li and W. K. Chow. "Preliminary studies on burning behavior of polymethylmethacrylate (pmma)," *J. Fire Sci.,* 20: 297-318 (2002).

71. Caminat, P. and E. Saatdjian. "The oxidation of solid graphite using a 5-kw co2, laser," *Combust. Flame,* 86: 249-257 (1991).

72. Li, C. and T. C. Brown. "Carbon oxidation kinetics from evolved carbon oxide analysis during temperature-programmed oxidation," *Carbon,* 39: 725-732 (2001).

73. Hayhurst, A. N. and M. S. Parmar. "Does solid carbon burn in oxygen to give the gaseous intermediate co or produce co2 directly? Some experiments in a hot bed of sand fluidized by air," *Chem. Eng. Sci.,* 53 (3): 427-438 (1998).

74. Arthur, J. R. "Reactions between carbon and oxygen," *Trans. Faraday Soc.,* 47: 164-178 (1951).

75. Kulasekaran, S., T. M. Linjewile, P. K. Agarwal and M. J. Biggs. "Combustion of a porous char particle in an incipiently fluidized bed," *Fuel,* 77 (14): 1549-1560 (1998).

76. Takahashi, M., M. Kotaka and H. J. Sekimoto. "Burn-off andproduction of co and co2 in the oxidation of nuclear reactor-grade graphites in a flow system," *J. Nucl. Sci. Technol.,* 31 (12): 1275-1286 (1994).

77. Walker, P. L., R. L. Taylor and J. M. Ranish. "An update on the carbon-oxygen reaction," *Carbon,* 29 (3): 411-421 (1991).

78. Mitchell, R. E., R. J. Kee, P. Glarborg and M. E. Coltrin. "The effect of co conversion in the boundary layers surrounding pulverized-coal char particles," *Proc. Combust. Inst.,* 23: 1169-1176 (1990).

79. Adomeit, G., G. Mohiuddin and N. Peters. "Boundary layer combustion of carbon," *Proc. Combust. Inst.,* 16 (1): 731-743 (1977).

80. Lear, A. E., T. C. Brown and B. S. Haynes. "Formation of metastable oxide complezes during the oxidation of carbons at low temperatures," *Proc. Combust. Inst.,* 23 (1): 1191-1197 (1990).

81. Tucker, B. G. and M. F. R. Mulcahu. "Formation and decomposition of surface oxide in carbon combustion," *Trans. Faraday Soc.,* 65: 274-286 (1969).

82. Ahmed, S. and M. H. Back. "The role of the surface complex in the kientics of the reaction of oxygen with carbon," *Carbon,* 23 (5): 513-524 (1985).

83. Eisenhut, W. *In chemistry of coal utilization, second supplementary volume*. New York, NY: John Wiley & Sons, Inc., 1981.

84. Vastola, F. J., P. J. Hart and P. L. Walker. "A study of carbon-oxygen surface complexes using o18 as a tracer," *Carbon,* 2 (1): 65-71 (1964).

85. Marsh, H. and A. D. Foord. "Mechanism of oxidation of carbon by molecular oxygen," *Carbon,* 11 (4): 421-424 (1973).

86. Du, Z., A. F. Sarofim, J. P. Longwell and C. A. Mims. "Kinetic measurement and modeling of carbon oxidation," *Energy Fuels,* 5 (1): 214-221 (1991).

87. Chelliah, H. K. "The influence of heterogeneous kinetics and thermal radiation on the oxidation of graphite particles," *Combust. Flame,* 104: 81-94 (1996).

88. Chelliah, H. K., A. Makino, I. Kato, N. Araki and C. K. Law. "Modeling of graphite oxidation in a stagnation-point flow field using detailed homogeneous and semiglobal heterogeneous mechanism with comparison to experiments," *Combust. Flame,* 104: 469-480 (1996).

89. Bradley, D., G. Dixon-Lewirs, S. El-Din Habik and E. M. J. Mushi. "The oxidation of graphite powder in flame reaction zones," *Proc. Combust. Inst.,* 20 (1): 931-940 (1984).

90. Calleja, G., A. F. Sarofim and C. Georgakis. "Effect of char gasification reaction order on bounding solutions for char combustion," *Chem. Eng. Sci.,* 36 (5): 919-929 (1981).

91. Dutta, S. and C. Y. Wen. "Reactivity of coal and char 2. In oxygen-nitrogen atmosphere," *Ind. Engng. Chem. Process Des. Dev.,* 16 (1): 31-37 (1977).

92. Dutta, S., C. Y. Wen and R. J. Belt. "Reactivity of coal and char 1. In carbon dioxide atmosphere," *Ind. Engng. Chem. Process Des. Dev.,* 16 (1): 20-30 (1977).

93. Field, M., D. Gill, B. Morgan and P. Hawksley. *Combustion of pulverized coal*. Leatherhead, Surrey, England: The British Coal Utilization Research Association, 1967.

94. Matsui, K. and H. Tsuji. "An aerothermochemical analysis of solid carbon combustion in the stagantion flow acompanied by homogeneous co oxidation," *Combust. Flame,* 70: 79-99 (1987).

95. Ding-Guo, X. and P. A. Libby. "The burning of graphite spheres with gas-phase equilibrium," *Combust. Flame,* 67: 37-57 (1987).

96. Howard, J. B., G. C. Williams and D. H. Fine. "Kinetics of carbon monoxide oxidation in postflame gases," *Proc. Combust. Inst.,* 14 (1): 975-986 (1974).

97. Steward, B. J., K. C. Gross and G. P. Perram. "Optical characterization of large caliber muzzle blast waves," *Propellants, Explos., Pyrotech.,* 36 (6): 564-575 (2011).

98. Krakow, B., E. Kiech and H. McAdoo. *Isolated co lines for use in combustion gas diagnostics*. Report number: AEDC-TR-77-11. Arnold Air Force Station, TN: USAF, 1977.

99. Wolfe, W. L. and G. J. Zissis. *The infrared handbook*. Washington DC: IRIA Center, Environmental Research Institute of Michigan, 1978.

100. Davis, S. P., M. C. Abrams and J. W. Brault. *Fourier transform spectrometry*. London, U.K.: Academic Press, 2001.

101. Rothman, L. S., I. E. Gordon, R. J. Barber, H. Dothe, R. R. Gamache, A. Goldman, V. I. Perevalov, S. A. Tashkun and J. Tennyson. "Hitemp, the high temperature molecular spectroscopic database," *J. Quant. Spectrosc. Radiat. Transf.,* 111: 2139-2150 (2010).

102. Rothman, L. S., et al. "The hitran2012 molecular spectroscopic database," *J. Quant. Spectrosc. Radiat. Transf.,* 130: 4-50 (2013).

103. Chang, H. and T. T. Charalampopoulos. "Determination of the wavelength dependence of refractive indices of flame soot," *Proc. R. Soc. London, A,* 430: 577-591 (1990).

104. Kupstov, A. H. and G. N. Zhizhin. *Handbook of fourier transform raman and infrared spectra of polymers, volume 45 (physical sciences data)*. Amsterdam, The Netherlands: Elsevier Science Publisher B.V., 1998.

105. Wade, L. G. *Organic chemistry*. Upple Saddle River, NJ: Pearson Prentice Hall Inc, 2006.

106. Depraz, S., M. Y. Perrin, P. Riviere and A. Soufiani. "Infrared emission spectroscopy of co2 at high temperature. Part ii: Experimental results and comparisons with spectroscopic databases," *J. Quant. Spectrosc. Radiat. Transf.,* 113: 14-25 (2012).

107. Modest, M. F. and S. P. Bharadwaj. "Medium resolution transmission measurements of co2 at high temperature," *J. Quant. Spectrosc. Radiat. Transf.,* 73: 329-338 (2002).

108. Tashkun, S. A. and V. I. Perevalov. "Cdsd-4000: High-resolution, high-temperature carbon dioxide spectroscopic databank," *J. Quant. Spectrosc. Radiat. Transf.,* 112: 1403-1410 (2011).

109. Gross, K. C., A. M. Young, C. Borel, B. J. Steward and G. P. Perram. "Simulating systematic scene-change artifacts in fourier-transform spectroscopy," *Proc. SPIE-Int. Soc. Opt. Eng.,* 7695: 76951Y (2010).

110. Zhou, Z. and A. C. Fernandez-Pello. "Numerical modeling of endothermic pyrolysis and ignition delay of composite materials exposed to an external radiant heat flux," *Proc. Combust. Inst.,* 28 (2): 2769-2275 (2000).

111. Koppman, R., K. von Czapiewski and J. S. Reid. "A review of biomass burning emissions, part i: Gaseous emissions of carbon monoxide, methane, volatile organic compounds, and nitrogen containing compounds," *Atmos. Chem. Phys. Discuss.,* 5: 10455-10516 (2005).

112. Celina, M., D. K. Ottesen, K. T. Gillen and R. L. Clough. "Ftir emission spectrocopy applied to polymer degradation," *Polym. Degrad. Stab.,* 58: 15-31 (1997).

113. Park, S. H., A. J. Stretton and C. L. Tien. "Infrared radiation properties of methyl methacrylate vapor," *Combust. Sci. Technol.,* 62: 257-271 (1988).

114. Gross, K. C., K. C. Bradley and G. P. Perram. "Remote identification and quantification of industrial smokestack effluents via imaging fourier-transform spectroscopy," *Environmental Science & Technology,* 62: 9390-9397 (2010).

115. Jiang, F., J. L. d. Ris and M. M. Khan. "Absorption of thermal energy in pmma by in-depth radiation," *Fire Safety J.,* 44: 106-112 (2009).

116. Rivercomb, H. E., H. Buijs, H. B. Howell, D. D. LaPorte, W. L. Smith and L. Sromovsky. "Radiometric calibration of ir fourier transform spectrometers: Solution to a problem with the high-resolution interferometer sounder," *Appl. Optics,* 27: 3210-3218 (1988).

117. Holland, B. J. and J. N. Hay. "The kinetics and mechanism of the thermal degradation of poly(methyl methacrylate) studied by thermal analysis-fourier transform infrared spectroscopy," *Polymer,* 42: 4825-4835 (2001).

118. Willis, H. A., V. J. I. Zichy and P. J. Hendra. "The laser-raman and infra-red spectra of poly(methyl methacrylate)," *Polymer,* 10: 737-746 (1969).

119. Martin, J. W., B. Dickens, D. Waksman, D. P. Bentz, W. E. Byrd, E. Embree and W. E. Roberts. "Thermal degradation of poly(methyl methacrylate) at 50c to 125c," *J. Appl. Polym. Sci.,* 34 (1): 377-393 (1987).

120. Wilmshurst, J. K. and J. F. Horwood. "The vibrational spectrum and molecular structure of methyl pyruvate," *Aust. J. Chem.,* 24: 1183-1191 (1971).

121. Wakatsuki, K. *High temperature radiation absorption of fuel molecules and an evaluation of its influence on pool fire modeling*. PhD Dissertation. University of Maryland, College Park, MD, USA, 2005.

122. Wakatsuki, K., S. P. Fuss, A. Hamins and M. R. Nyden. "A technique for extrapolating absorption coefficient measurements to high temperatures," *Proc. Combust. Inst.,* 30: 1565-1573 (2005).

123. Gross, L. A., P. R. Griffiths and J. N. P. Sun. *Infrared measurements for gaseous measurements*. New York, USA: Marcel Decker, 1985.

124. Orloff, L., J. D. Ris and G. H. Markstein. "Upward turbulent fire spread and burning of fuel surface," *Proc. Combust. Inst.,* 15 (1): 183-192 (1975).

125. Kashiwagi, T. and T. J. Ohlemiller. "A study of oxygen effects on nonflaming transient gasification of pmma and pe during thermal irradiation," *Proc. Combust. Inst.,* 19: 815-823 (1982).

126. Linstrom, P. J. and W. G. Mallard, Eds. Nist chemistry webbook, nist standard reference database number 69. Gaithersburg, MD: National Institute of Standards and Technology, http://webbook.nist.gov, (retrieved March 8, 2014).

127. Brown, J. E. and T. Kashiwagi. "Gas phase oxygen effect on chain scission and monomer content in bulk poly(methyl methacrylate) degraded by external thermal radiation," *Polym. Degrad. Stab.,* 52: 1-10 (1996).

128. Chaiken, R. F., W. H. Andersen, M. K. Barsh, E. Mishuck, G. Moe and R. D. Schultz. "Kinetics of the surface degradation of polymethylmethacrylate," *J. Chem. Phys.,* 32: 141-146 (1960).

129. Arisawa, H. and T. B. Brill. "Kinetics and mechanism of flash pyrolysis of poly(methyl metchacrylate) (pmma)," *Combust. Flame,* 109: 415-426 (1997).

130. Cowley, P. R. E. J. and H. W. Melville. "The photo-degradation of polymethylmethacrylate ii. Evaluation of absolute rate constants for a depolymerization reaction," *Proc. R. Soc. London, A,* 211 (1106): 320-334 (1952).

131. Kashiwagi, T., A. Inaba, J. E. Brown, K. Hatada, T. Kitayama and E. Masuda. "Effects of weak linkages on the thermal and oxidative degradation of poly(methyl methacrylates)," *Macromolecules,* 19 (8): 2160-2168 (1986).

132. Acosta, R. I., K. C. Gross and G. P. Perram. "*Mid-infrared imaging fourier transform spectrometry for high power fiber laser irradiated fiberglass composites*," Proc. SPIE. 8239: 82390R (2012).

133. Phillips, R., F. J. Vastola and P. L. Walker. "Factors affecting the product ratio of the carbon-oxygen reaction-ii. Reaction temperature," *Carbon,* 8: 205-210 (1970).

134. Zazula, J. M. *On graphite transformations at high temperature and pressure induced by absorption of the lhc beam*. Report number: CERN-LHC-Project-Note-78. European Organization for Nuclear Research: 1997.

135. Steinbeck, J., G. Braunstein, M. S. Dresselhaus, T. Venkatesan and D. C. Jacobson. "A model for pulsed laser melting of graphite," *J. Appl. Phys.,* 58: 4374-4382 (1985).

136. Bundy, F. P. "Pressure-temperature phase diagram of elemental carbon," *Phys. A,* 156 (1): 169-178 (1989).

137. Bonelli, M., M. A., P. M. Ossi and A. Pessi. "Laser-irradiation-induced structural changes on graphite," *Phys. Rev. B: Condens. Matter,* 59: 13513-13516 (1999).

138. Tashkun, S. A., V. I. Perevalov, J.-L. Teffo, A. D. Bykov and N. N. Lavrentieva. "Cdsd-1000, the high temperature carbon dioxide spectroscopic databank," *J. Quant. Spectrosc. Radiat. Transf.,* 82 (1-4): 165-196 (2003).

139. Tashkun, S. A., V. I. Perevalov, J. L. Teffo, L. S. Rothman and V. G. Tyuterev. "Global fitting of 12c16o2 vibrational–rotational line positions using the effective hamiltonian approach," *J. Quant. Spectrosc. Radiat. Transf.,* 60 (5): 785-801.

140. Tashkun, S. A., V. I. Perevalov, J.-L. Teffo and V. G. Tyuterev. "Global fit of 12c16o2 vibrational–rotational line intensities using the effective operator approach," *J. Quant. Spectrosc. Radiat. Transf.,* 62 (5): 571-598 (1999).

141. Bharadwaj, S. P. and M. F. Modest. "Medium resolution transmission measurements of co2 at high temperature-an update," *J. Quant. Spectrosc. Radiat. Transf.,* 103: 146-155 (2007).

142. Depraz, S., M. Y. Perrin and A. Soufiani. "Infrared emission sepctroscopy of co2 at high temperature. Part i: Experimental setup and source characterization," *J. Quant. Spectrosc. Radiat. Transf.,* 113: 1-13 (2012).

143. Ferriso, C. C., C. B. Ludwig and L. Acton. "Spectral-emissivity measurements of the 4.3 u co2 band between 2650 and 3000 k," *J. Opt. Soc. Am.,* 56: 171-173 (1966).

144. Gamache, R. R., R. L. Hawkins and L. S. Rothman. "Total internal partition sums in the temperature range 70-3000 k: Atmospheric linear molecules," *J. Mol. Spectrosc.,* 142 (2): 205-219 (1990).

145. Gamache, R. R., S. Kennedy, R. Hawkins and L. S. Rothman. "Total internal partition sums for molecules in the terrestrial atmosphere," *J. Mol. Struct.,* 517-518: 407-425 (2000).

146. Linjewile, T. M., V. S. Gururajan and P. K. Agarwal. "The co/co2 product ratio from the combustion of single petroleum coke spheres in an incipiently fluidized bed," *Chem. Eng. Sci.,* 50 (12): 1881-1888 (1995).

147. Tu, C. M., H. Davis and H. C. Hottel. "Combustion rate of carbon - combustion of spheres in flowing gas streams," *Ind. Eng. Chem.,* 26 (7): 749-757.

148. Matsui, K., H. Tsuji and A. Makino. "The effects of water vapor concentration on the rate of combustion of an artificial graphite in humid air flow," *Combust. Flame,* 50: 107-118 (1983).

149. Tognotti, L., J. P. Longwell and A. F. Sarofim. "The products of the high temperature oxidation of a single char particle in an electrodynamic balance," *Proc. Combust. Inst.,* 23 (1): 1207-1213 (1991).

150. Adomeit, G., W. Hocks and H. Henriksen. "Combustion of a carbon surface in a stagnation point flow field," *Combust. Flame,* 59: 273-288 (1985).

151. Mitchell, R. E. "Variations in the temperatures of coal-char particles during combustion: A consequence of particle-to-particle variations in ash-content," *Proc. Combust. Inst.,* 23 (1): 1297-1304 (1991).

152. Van Krevelen, D. W. "Some basic aspects of flame resistance of polymeric materials," *Polymer,* 16: 615-620 (1975).

153. Kandola, B. K. and A. R. Horrocks. "Complex char formation in flame-retarded fiber/intumescent combinations: Physical and chemical nature of char," *Text. Res. J.,* 69 (5): 374-381 (1999).

154. Poljansek, I. and M. Krajnc. "Characterization of phenol-formaldehyde prepolymer resin by in line ft-ir spectroscopy," *Acta Chim. Slov.,* 52: 238-244 (2005).

155. Anderson, K. B., R. S. Tranter, W. Tang, K. Bezinsky and L. B. Harding. "Speciation of c6h6 isomers by gas chromatography-matrix isolation fourier transform infrared spectroscopy-mass spectrometry," *J. Phys. Chem. A,* 108: 3403-3405 (2004).

Vita

Capt Acosta was born and raised in Puerto Rico, where he graduated with a B.S. in Physics from the University of Puerto Rico with honors. At the University of Puerto Rico, he received a NASA scholarship with research efforts in nano-bio markers. He was a distinguished graduated from the Air Force Reserve Office Training Corps (AFROTC) Detachment 755 where he received a commission as a 2nd lieutenant in the United States Air Force.

His first assignment was at the Air Force Research Laboratory Materials & Manufacturing Directorate (AFRL/RX), where he worked as a Bio Materials Research Scientist & Power Materials Lead Scientist. He also completed an M.S. in Physics at Wright State University, Dayton, OH. In 2010 he deployed to Naval Air Station Guantanamo Bay, Cuba as the Joint Air Operations Officer in support of Operation Enduring Freedom and Operation Unified Response in support of the Haiti relief efforts. The same year he started the Air Force Institute of Technology (AFIT) PhD program in Applied Physics.

REPORT DOCUMENTATION PAGE

Form Approved
OMB No. 074-0188

1. REPORT DATE *(DD-MM-YYYY)*	2. REPORT TYPE	3. DATES COVERED *(From – To)*
06-16-2014	Dissertation	September 2010 – June 2014

TITLE AND SUBTITLE
Imaging Fourier Transform Spectroscopy of the Boundary Layer Plume from Laser Irradiated Polymers and Carbon Materials

5a. CONTRACT NUMBER
5b. GRANT NUMBER
5c. PROGRAM ELEMENT NUMBER

6. AUTHOR(S)
Acosta, Roberto I., Captain, USAF

5d. PROJECT NUMBER
5e. TASK NUMBER
5f. WORK UNIT NUMBER

7. PERFORMING ORGANIZATION NAMES(S) AND ADDRESS(S)
Air Force Institute of Technology
Graduate School of Engineering and Management (AFIT/ENP)
2950 Hobson Way, Building 640
WPAFB OH 45433-8865

8. PERFORMING ORGANIZATION REPORT NUMBER
AFIT-ENP-DS-14-J-8

9. SPONSORING/MONITORING AGENCY NAME(S) AND ADDRESS(ES)
High Energy Laser Joint Technology Office
901 University
Blvd. SE, Suite 100, Albuquerque, NM 87106
505-248-8208, harro.ackermann@jto.hpc.mil
ATTN: Dr. Harro Ackermann

10. SPONSOR/MONITOR'S ACRONYM(S)
HEL-JTO

11. SPONSOR/MONITOR'S REPORT NUMBER(S)

12. DISTRIBUTION/AVAILABILITY STATEMENT
DISTRUBTION STATEMENT A. APPROVED FOR PUBLIC RELEASE; DISTRIBUTION UNLIMITED.

13. SUPPLEMENTARY NOTES
This material is declared a work of the U.S. Government and is not subject to copyright protection in the United States.

14. ABSTRACT
Emissive plumes from laser irradiated fiberglass reinforced polymers (FRP), poly(methyl methacrylate) (PMMA) and porous graphite targets were investigated primarily using a mid wave infrared (MWIR) imaging Fourier transform infrared (FTIR) spectrometer. Polymer and graphite targets were irradiated with a 1.064 μm Nd:YAG and a 1.07 μm ytterbium continuous wave (CW) fiber lasers respectively. Data was acquired with a spectral resolution of 2 cm^{-1} and spatial resolution as high as 0.52 mm^2 per pixel. Strong emissions from H_2O, CO, CO_2 and hydrocarbons were observed in the MWIR between 1900 cm^{-1} and 4000 cm^{-1}. A single-layer radiative transfer model was developed to estimate spatial maps of temperature and column densities of CO and CO_2 from the hyperspectral imagery of the boundary layer plume of irradiated FRP and porous graphite targets. The spectral model was used to compute the absorption cross sections of CO and CO_2 using spectral line parameters from the high temperature extension of the HITRAN. Also, spatial maps of plume temperature and methyl methacrylate (MMA) column density were developed for laser irradiated black PMMA.

15. SUBJECT TERMS
Hyperspectral Imaging; High Energy Laser; Combustion Plume; Carbon Combustion; Laser Lethality; Laser Materials

16. SECURITY CLASSIFICATION OF:			17. LIMITATION OF ABSTRACT	18. NUMBER OF PAGES	19a. NAME OF RESPONSIBLE PERSON
a. REPORT	b. ABSTRACT	c. THIS PAGE			Glen P. Perram, PhD, AFIT/ENP
U	U	U	UU	216	19b. TELEPHONE NUMBER *(Include area code)* (937) 255-6565, ext 4504 glen.perram@afit.edu

Standard Form 298 (Rev. 8-98)
Prescribed by ANSI Std. Z39-18